Changes of the Greenland ice sheet - derived from ICESat and GRACE data

Sørensen, Louise Sandberg; Tscherning, Carl Christian; Forsberg, René

Publication date:
2010

Document Version
Publisher's PDF, also known as Version of record

THE PHD SCHOOL OF SCIENCE
FACULTY OF SCIENCE
UNIVERSITY OF COPENHAGEN

Ph.D. thesis

Sofie Louise Sandberg Sørensen

Changes of the Greenland ice sheet - derived from ICESat and GRACE data.

Supervisor: Carl Christian Tscherning, University of Copenhagen
Co-supervisor: Rene Forsberg, DTU Space.

Submitted: December 20, 2010

DTU Space
National Space Institute

Resume

Jordens klima er i forandring og Grønland's indlandsis reagerer på klimaændringerne. Satellitobservationer har været et vigtigt instrument til at kunne kortlægge iskappens forandringer. Afsmeltningen af Jordens store og små iskapper bidrager til den globale havniveau-stigning, og det er vigtigt at fastlægge hvor stort dette bidrag er. Hvis hele Grønland's indlandsis smelter vil det globale havniveau øges med ca. 7 m. Der er et stort fokus på at bestemme størrelsen af bidraget fra Grønland's indlandsis, og at opnå større forståelse af mekanismerne bag de observerede forandringer af iskappen.

I denne afhandling anvendes data fra to satellit-missioner, til at kortlægge forandringerne af Grønlands indlandsis. Målet er at bestemme iskappens totale massebalance, og dermed også bidraget til havniveaustigningen. De to anvendte datasæt har meget forskellige egenskaber, og bruges til at bestemme to uafhængige massebalance-estimater.

Gravity Recovery And Climate Experiment (GRACE) er en tyngde-satellitmission, der blev opsendt i 2002 og stadig leverer data. Adskillige processeringscentre genererer månedlige globale tyngdefelts-modeller. En analyse af disse modeller afslører en stærk negativ trend i tyngdefeltet over Grønland. Denne trend afspejler et massetab af is. En inversionsmetode benyttes til at bestemme masseændringerne af indlandsisen udfra de observerede tyngdeændringer. Der korrigeres for den tyngdeændring som skyldes Jordens respons på masseændringerne. Der er ikke fuldstændig overensstemmelse mellem de månedlige modeller fra de forskellige processerings-centre, hvilket betyder at inversionsmetoden giver massetabsestimater mellem $-242 \pm 36\,\mathrm{Gt\,år^{-1}}$ og $-96 \pm 22\,\mathrm{Gt\,år^{-1}}$ for perioden august 2002 - august 2009.

NASA's Ice, Cloud, and land Elevation Satellite (ICESat) er en laser-altimetri mission, der fra opsendelsen i 2003 til 2009 har målt ændringer af overfladehøjden af Grønland's indlandsis. Der opstod problemer med laserinstrumentet på ICESat allerede på et tidligt stadie af missionen, hvilket resulterede i, at den kun har målt 2 eller 3 måneder hvert år istedet for at måle kontinuert, som i den oprindelige plan. Dette har resulteret i en reduceret datadækning. Derudover bliver ICESat sporene ikke gentaget helt præcist, og dette gør det vanskeligt at bestemme højdeændringerne. I dette studie er der udviklet forskellige metoder til at bestemme højdeændringer af Grønland's indlandsis fra ICESat data, hvilket resulterer i estimater af den årlige volumenændring af iskappen.
Den fundne volumenændring af Grønland's indlandsis konverteres til en masseændring ved at benytte modellerede is- og snedensiteter samt korrigere for højdeændrings-signaler, som ikke bidrager til massebalancen. Korrektionerne består af firn kompaktion, bevægelse af undergrunden (som er et resultat af masseændringer på både kort og lang tidsskala) og et offset i højderne mellem de forskellige ICESat måle-perioder. Fra ICESat-analysen estimeres massebalancen for Grønlands indlandsis for perioden 2003-2008 til at være
$-210 \pm 21\,\mathrm{Gt\,år^{-1}}$.

Abstract

The Greenland ice sheet (GrIS) is responding to the changing climate, and satellite observations have been crucial in mapping these changes. The melting of the large ice sheet contribute to the global sea level rise, and it is important to determine this present-day contribution. If the entire GrIS melted, it would result in a sea level rise of approximately 7 m. It is of great importance to determine the mass balance of the GrIS, and to understand the mechanisms controlling the observed changes of the ice sheet.

In this thesis, data from two satellite missions are used to determine the present-day changes of the GrIS with the goal of determining the mass balance of the GrIS, and hence it's contribution to the global sea level rise. The two data sets are very different in nature, and they are used to create two independent mass balance results.

The Gravity Recovery And Climate Experiment (GRACE) is a gravity satellite mission, which was launched in 2002 and is still operating. Several processing centres provide monthly global gravity models based on GRACE data. A trend analysis of these monthly models reveals a strong negative trend in gravity over Greenland associated with ice mass loss. An inversion method is applied in order to derive ice mass changes from the gravity changes. Part of the gravity trend observed by GRACE is caused by glacial isostatic adjustment (GIA) and by the elastic response due to present-day changes. There is not complete consensus between the monthly solutions from the different processing centres, and mass balance estimates in the range $-242 \pm 36\,\mathrm{Gt\,yr^{-1}}$ to $-96 \pm 22\,\mathrm{Gt\,yr^{-1}}$ are obtained for the period August 2002 - August 2009.

NASA's Ice, Cloud, and land Elevation Satellite (ICESat) is a laser altimetry mission, and it measured the surface elevation changes of the ice sheets from the launch in 2003 until 2009. Problems with the lasers on-board ICESat early in the mission, have reduced the measurements to two or three months every year, and this has also reduced the spacial coverage of the satellite. Furthermore the tracks are not repeated exactly, and this makes deriving rates of elevation changes difficult. Different methods for deriving elevation from the ICESat altimetry was developed in this study, from which volume changes are derived. The volume change of the GrIS derived from ICESat data are converted into mass change, by correcting the observed elevation changes for movements not related to ice mass balance, and by modeled snow/ice densities. The elevation change corrections applied are the firn compaction correction, the bedrock movement (both the elastic signal and the glacial isostatic adjustment), and an ICESat inter-campaign elevation bias correction. From the ICESat analysis, a mass balance estimate for 2003-2008 of $-210 \pm 21\,\mathrm{Gt\,yr^{-1}}$ for the GrIS is obtained.

Preface

This thesis is submitted in fulfilment of the requirements for obtaining a Ph.D. degree at the Niels Bohr Institute, University of Copenhagen. The research presented here was carried out within the Division of Geodynamics, DTU Space, under supervision of C. C. Tscherning at University of Copenhagen and R. Forsberg at DTU Space. The Ph.D. program was partly funded by COGCI (Copenhagen Global Change Initiative). This thesis includes four scientific papers; Sørensen and Forsberg (2010), Sørensen et al. (2010a), Hvidegaard et al. (2010) and Sørensen et al. (2010b).

It was stated in the 4th IPPC report from 2007 that the future contribution from the large ice sheets to sea level rise is very uncertain. This highlighted the need for a scientific focus on the changes of the large ice sheet. The subject of climate change and sea level rise is indeed a hot topic, and it has been very exciting to work within this scientific area.

During the Ph.D. program I have had the opportunity to participate in many conferences and meetings and I very much appreciate the network and the great experiences it has given me.
I spent a week in Urbino, Italy, visiting Prof. Giorgio Spada. During this stay I learned a lot about SELEN, GIA and I enjoyed the extraordinary hospitality from G. Spada and colleagues. Also, I want to thank Gudfinna Adalgeirsdottir for welcoming me at DMI, where I spent one month.

I am grateful to all the people who have been involved in the process - both my wonderful family and my great colleagues. I want to thank my supervisors for their confidence in my work, and for their inspiration.

Also, I would like to thank my co-authors, especially S. Simonsen and K. Nielsen who both have put a lot of working hours and enthusiasm into the manuscript : Sørensen et al. (2010a).

Louise Sandberg Sørensen
Copenhagen, December 2010

Cover: Space Shuttle photograph of the southern part of Greenland taken on 29 March 1992. From: http://pubs.usgs.gov/pp/p1386c/p1386c.pdf

List of abbreviations

ASIRAS	Airborne Synthetic Aperture and Interferometric Radar Altimeter System
ASTER	Advanced Spaceborne Thermal and Emission reflection Radiometer
CNES	Centre National d'Etudes Spatiales
CSR	Center for Space Research
DEM	Digital Elevation Model
DLR	Deutches Zentrum für Luft-und Raumfahrt
EGIG	Expédition Glaciologique au Groenland
ELA	Equilibrium line altitude
ERS	European Remote Sensing satellite
GDEM	Global Digital Elevation Model
GF	Green's Function
GFZ	GeoForschungsZentrum
GIA	Glacial Isostatic Adjustment
GLAS	Geoscience Laser Altimeter System
GPS	Global Positioning System
GRACE	Gravity Recovery And Climate Experiment
GrIS	Greenland Ice Sheet
ICESat	Ice, cloud and land Elevation Satellite
IGG	Institut für Geodäsie und Geoinformatik
InSAR	Interferometric Synthetic Aperture Radar
IPCC	Intergovernmental Panel of Climate Change
I-SIPS	ICESat Science Investigator led Processing System
ITG	Institute for Theoretical Geodesy
JPL	Jet Propulsion Laboratory
LAGEOS	Laser Geodynamics Satellites
LEO	Low Earth orbit
LGM	Last glacial maximum
LiDAR	Light Detection And Ranging

LDC	load deformation coefficients
MB	Mass balance
NASA	National Aeronautics and Space Administration
NSIDC	National Snow and Ice Data Center
PREM	Preliminary Reference Earth Model
RCM	regional Climate model
RDC	Raw Data Center
RMSE	Root Mean Square Error
RSL	Relative Sea Level
SAR	Synthetic Aperture Radar
SLE	Sea Level Equation
SLR	Satellite Laser Ranging
SMB	Surface Mass Balance

Contents

List of Figures

List of Tables

Chapter 1

Introduction

The main goal of this Ph.D. study is to determine the present-day (2002-2010) changes and mass balance of the Greenland ice sheet (GrIS) from satellite data. In the following, the different methods for determining ice sheet mass balance are described, and the structure of the thesis is also outlined.

1.1 Background and motivation

In recent years there has been a focus on the subject of climate change. Many scientists from various fields have worked to determe these climate changes, and to predict their future effects. In the 4th Intergovernmental Panel of Climate Change (IPCC) report from 2007 (Solomon et al., 2007), it was concluded that the climate changes are human induced and various future scenarios were outlined. It was furthermore stated that a major limitation in predicting future sea-level changes, is the contribution from the ice sheets. Ice dynamics is very sensitive to climatic changes, but the physical processes behind this mechanism are poorly understood. The amount of water, currently stored in the GrIS, is estimated to be equivalent to a 7.3 m global sea level rise (Bamber et al., 2001a). The current state of the large ice sheets must be known, in order to determine their role in the global climate system and obtain more reliable future climate scenarios. It is therefore of great importance to obtain a better understanding of the dynamics of ice sheets.

During the last decade much research, focusing on the large ice sheets, has been carried out, in order to get a better picture of the effect of the present-day climate changes in polar regions. Dramatic changes in the Greenland ice sheet have been observed (e.g. Krabill et al. (2004); Velicogna and Wahr (2005); Joughin et al. (2010)). Many of the largest outlet glaciers velocity has accelerated, causing an increased ice discharge. The largest accelerations have been observed at the Helheim, Kangerdlussuaq and Jakobshavn glaciers.

1.2 How to determine the mass balance of an ice sheet

The mass balance of an ice sheet is the difference between the mass gained by accumulation and the mass loss caused by discharge, sublimation and melting. During the last decade, satellite missions such as GRACE (Gravity Recovery And Climate Experiment), ICESat (Ice, cloud and land Elevation Satellite), ERS (European Remote Sensing satellite), and Envisat have measured the entire ice sheet, and many methods have been developed in order to optimally use the available data. There are three primary methods to estimate the mass balance of the ice sheets, using satellite data; the gravity method, the elevation change method, and the mass budget method.

The gravity method is the method used to estimate mass balance from the gravity satellite mission GRACE. The observed spatio-temporal gravity changes are associated with mass re-distribution in the atmosphere and in and on the Earth. The gravity method is also called the weighting method, since an observed change in gravity is directly associated with a change in mass. A challenge when using this method is to seperate the signals contributing to the gravity signature, such as hydrology, glacial isostatic adjustment (GIA) and present-day mass changes. The change in gravity caused by ice mass changes can be isolated by modelling the other contributing signals, and hence the ice sheet mass balance can be determined from the gravity changes by either forward modelling or an inversion scheme.

The elevation change method is based on repeated elevation measurements of the ice sheet. These are performed from satellites and airplanes using radar and laser altimeters. The derived elevation changes are translated into mass changes by using assumptions of snow and ice densities. It is also necessary to take elevation changes not related to the ice sheet mass balance into account. The largest of these corrections is the firn compaction correction, but the bedrock movement and potential elevation bias between different measurement campaigns must also be taken into account.

The mass budget method compares the sources and sinks of ice mass. Accumulation is compared to sublimation, calving, runoff etc. The information of accumulation comes primarily from ice cores, and the calving/discharge can be determined from Interferometric Synthetic Aperture Radar (InSAR) measurements of glacier velocities together with the ice thickness. The major challenge with the mass budget method is the lack of sufficiently accurate data for determining the various contributions to the mass budget equation.

1.3 Scientific objective and methods

In this thesis, the state of the art research concerning the mass balance of the Greenland ice sheet will be outlined. Results based on different techniques will be summarised and a picture of an increasing mass loss of the ice sheet during the last decade is found. Mass

balance estimates based on different methods and measurements do not show complete consensus, and it is therefore important to understand the reasons for these differences.

The scientific objective of this thesis is to derive two independent mass balance estimates of the Greenland ice sheet. One estimate is derived using the gravity method, based on data from the GRACE mission 2002-2010. The other mass balance estimate is obtained using the elevation change method, using data from the ICESat mission 2003-2008. The two methods and data sets used in this study, are used to directly estimate the mass or volume changes of the entire ice sheet. The differences between the mass balance estimates will be described, and the reasons for these differences will be discussed.

Besides determining the total mass balance, it is also an objective of this study, to describe and compare the regional changes of the GrIS. A mass balance estimate obtained from a combination of the GRACE and ICESat data is outside the scope of this Ph.D. project.

1.4 Structure of this thesis

This thesis is based on four papers. These are described briefly in Chap. 2, and are enclosed in App. A-D. The content of this thesis is supplementary to the content of these four papers.

The Earth's climate is getting warmer, and this warming is amplified in the high northern latitudes. Some key findings concerning the climatic changes and the associated response of the GrIS from the remote sensing and cryosphere communities are presented in Chap. 3.

The two satellite missions, GRACE and ICESat, are described in Chap. 4 and 5, respectively.
The GRACE data is described in Sect. 4.4 and the post-processing applied to the data in order to derive temporal gravity changes, is covered in Chap. 7. To derive the mass balance of the GrIS from the GRACE gravity changes, an inversion method is applied. The results of the inversion scheme is outlined in Sect. 7.5.
The ICESat altimetry data, which is described in Sect. 5.4, contains some less reliable measurements caused by e.g. cloud reflections and saturation, and some data culling is therefore necessary (Sect. 5.5). The methods developed for deriving surface elevation changes from the ICESat data are described in Chap. 8, together with the different elevation change corrections that must be applied to derive mass balance. In Sect. 8.3 the mass changes of the GrIS derived from ICESat data are presented.

Both the GRACE and ICESat measurements are sensitive to GIA, which is the response of the Earth due to changes in ice load since the last glacial maximum (LGM). It is necessary to determine the GIA signal from models of ice history and Earth rheology, in order to

isolate and estimate the present-day ice mass changes from the satellite data. Therefore, Chap. 6 is dedicated to the description of the GIA processes, and the methods used to calculate the present-day gravity change and elevation change signals caused by GIA.

The two independent mass balance estimates from GRACE and ICESat are compared in Chap. 9, in which a basin scale analysis is also presented. In Chap. 10 the sea level rise associated with the mass loss of the GrIS is discussed.

The methods developed for estimating changes of the GrIS for this Ph.D. study, can be used to investigate other ice covered areas as well, and in Chap. 11 a case study of the Antarctic ice sheet is presented.

The results obtained in this thesis are summarised in Chap. 12, along with a discussion of ideas for future work and developments.

Chapter 2

Scientific papers

The scientific work carried out in this Ph.D. programme is partly described in the papers listed below. This thesis is a summary of these papers.

Paper 1
Sørensen, Louise Sandberg and Forsberg, R. (2010), *Greenland Ice Sheet Mass Loss from GRACE Monthly Models*, Gravity, Geoid and Earth Observation, vol. 135, pp. 527–532, doi:10.1007/978-3-642-10634-7_70. Sørensen and Forsberg (2010), App. A.

This paper describes the inversion method used for deriving ice mass changes from GRACE data. This generalised inversion method was applied on GRACE data from three different processing centres; GFZ (GeoForschungsZentrum), CSR (Center for Space Research), and JPL (Jet Propulsion Laboratory). The data time span was August 2002 to August 2008. It was concluded that there were large differences in the calculated mass balance estimates of the Greenland ice sheet, derived from the different data sets. We found mass losses of $189\,\mathrm{Gt\,yr^{-1}}$, $146\,\mathrm{Gt\,yr^{-1}}$ and $67\,\mathrm{Gt\,yr^{-1}}$ from the CSR, GFZ and JPL data, respectively.

Paper 2
Sørensen, Louise Sandberg, Simonsen, S. B., Nielsen, K., Lucas-Picher, P., Spada, G., Adalgeirsdottir, G., Forsberg, R. and Hvidberg, C. S. (2010), *Mass balance of the Greenland ice sheet - A study of ICESat data, surface density and firn compaction modelling*, under review in The Cryosphere Discussions. Sørensen et al. (2010a), App. B

In this paper, four different methods to derive the elevation changes from the ICESat altimetry data set were presented. We found firn dynamics and surface densities to be important factors in deriving the mass loss from remote sensing altimetry. The volume change derived from ICESat data was corrected for firn compaction, vertical bedrock movement and an inter-campaign elevation bias in the ICESat data. Subsequently, the corrected volume change was converted into mass change by surface density models. We found an annual mass loss of the Greenland ice sheet of $210\pm21\,\mathrm{Gt\,yr^{-1}}$ in the period October 2003 to March 2008.

Paper 3
Hvidegaard, Sine Munk, Sørensen, L. S. and Forsberg, R. (2010), *ASTER GDEM validation using LiDAR data over coastal regions of Greenland*, In press, Remote Sensing Letters. Hvidegaard et al. (2010), App. C

One of the methods for deriving elevation changes from ICESat data, presented in paper 2, uses a digital elevation model (DEM) of the ice sheet in order to correct for the cross track slope. Therefore, the ASTER (Airborne Synthetic Aperture and Interferometric Radar Altimeter System) Global Digital Elevation Model (GDEM) could potentially be used as an independent high-resolution DEM in the ICESat analysis.

The ASTER GDEM was released in June 2009. It provides surface elevations at a resolution of 1 arc second. The aim of paper 3 was to evaluate the vertical accuracy of the ASTER GDEM in the coastal regions of Greenland, and to identify some of the associated sources of error. As validations, LiDAR (Light Detection And Ranging) measurements from various ice monitoring campaigns - both over land and ice covered areas - was used. We found that the ASTER tiles investigated, show an accuracy of 15-65 m RMSE (root mean square error).

Paper 4
Sørensen, Louise Sandberg, Stenseng, L., Simonsen, S. B., Forsberg, R., Poulsen, S. K. and Helm, V. (2010), *Greenland Ice Sheet changes from space using laser, radar and gravity*, ESA Living Planet Conference, ESA Special Publication SP-686. Sørensen et al. (2010b), App. D

In this paper we applied the inversion technique described in paper 1, to derive a mass balance of the Greenland ice sheet for the period 2002-2009 based on the CSR monthly solutions. In this study, the C_{20} coefficients of the spherical harmonic solutions were substituted with those obtained from satellite laser ranging (SLR) satellites. This analysis reveals a mass loss estimate of $204\,\mathrm{Gt\,yr^{-1}}$. We showed in paper 2 that the firn compaction correction was a large contribution in the ice sheet volume to mass conversion. It is therefore important to validate the model results. In this paper, ASIRAS (Airborne Synthetic Aperture and Interferometric Radar Altimeter System) radar data from the EGIG (Expédition Glaciologique au Groenland) line was used, and we found that it showed great potential for validating the glaciological models.

Chapter 3

State of the Greenland ice sheet

The Earth's climate is changing (Solomon et al., 2007), and the Greenland ice sheet is sensitive to these climate changes. Space-based measurements have been crucial in mapping the recent changes of the Greenland ice sheet. The GRACE mission has observed a massive mass loss of the ice sheet (e.g Luthcke et al. (2006)), while altimetry missions, such as ICESat, have mapped the spatial variability of the elevation changes (e.g Pritchard et al. (2009)), and InSAR measurements have been used to determine an acceleration of many major outlet glaciers (e.g Joughin et al. (2010)). The measuring techniques are very different in nature, and a comparison of the different measurements will help to better understand the different components of the ice sheet mass balance (MB). In this chapter, some of the key results concerning the recent changes of the GrIS are outlined, and the methods and data used are summarised.

3.1 A warmer climate and ocean

Fig. 3.1(a) shows the mean annual surface temperature anomaly for the period 2002-2009 (the time span of the data used in this thesis), compared with the period 1951-1980 (*data.giss.nasa.gov/gistemp*). The plot shows an overall global temperature increase which is largest at high latitudes. This polar amplification becomes clear when looking at the zonal means of the temperature anomaly, see Fig. 3.1(b). It is a consequence of feedback mechanisms of ice covered regions, but is less significant in Antarctica because the southern ocean acts as a heat sink.

The increased mean annual temperature in Greenland has resulted in an increased surface melting of the ice sheet (Mote, 2007). The increased surface melting can be one of the triggering factors concerning glacier speed-up, as a result of the melt water reaching the bed of the glacier (Zwally et al., 2002a).

The temperature of the ocean around Greenland has also increased in recent years. The warmer waters are believed to be a primary cause of the acceleration of some of the large

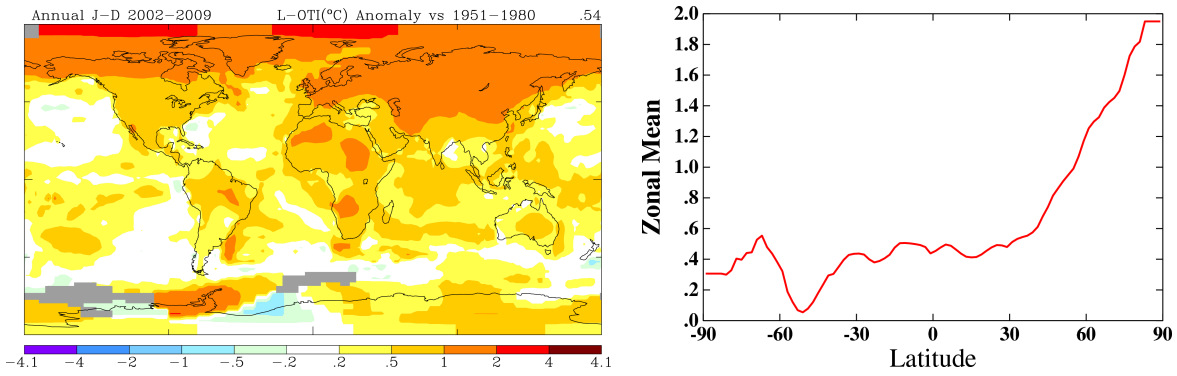

Figure 3.1: *(a) Global plot of the mean annual temperature change for the period 2002-2009 compared to 1951-1980. (b) Zonal means of the data shown in (a). Figure generated at data.giss.nasa.gov/gistemp*

marine-terminating outlet glaciers (Holland et al., 2008; Hanna et al., 2009; Rignot et al., 2010).

3.2 Acceleration of outlet glaciers

Many recent research results indicate that the ice sheet reacts dynamically to a warming climate, and as already mentioned, several studies have confirmed an acceleration in the velocity of many of the large outlet glaciers of the GrIS, such as Helheim, Jakobshavn and Kangerdlussuaq. The velocities can be mapped from space by using feature tracking of imagery (Howat et al., 2007), or SAR data (Rignot et al., 2004; Rignot and Kanagaratnam, 2006; Joughin et al., 2008, 2010). Figure 3.2 shows a velocity map from the western coast of Greenland for 2005/2006, compiled by Joughin et al. (2010). The change in speed from 2000/2001 to 2005/2006 is also shown in Fig 3.2, where the speed-up of the Jakobshavn glacier is clearly evident. A similar speed-up of glaciers is found along most of the ice sheet margin.
The increased glacier velocity results in increased discharge, and also mass loss of the glaciers. The unloading of the bedrock can be observed by permanent GPS (Global Positioning System) measurements from instruments placed on the bedrock close to the glaciers (Khan et al., 2007, 2010b).

The fact, that the glacier speed-up and retreat in Southeast Greenland is observed to be almost synchronuous, indicates that the glacier dynamics is very sensitive to the climate changes (Howat et al., 2008a). The relationship between the climate forcing and the dynamic response is poorly understood. The conclusion of the research on glaciers is, that the outlet glaciers have accelecated to a level that is above the level which keeps the GrIS in a steady-state.

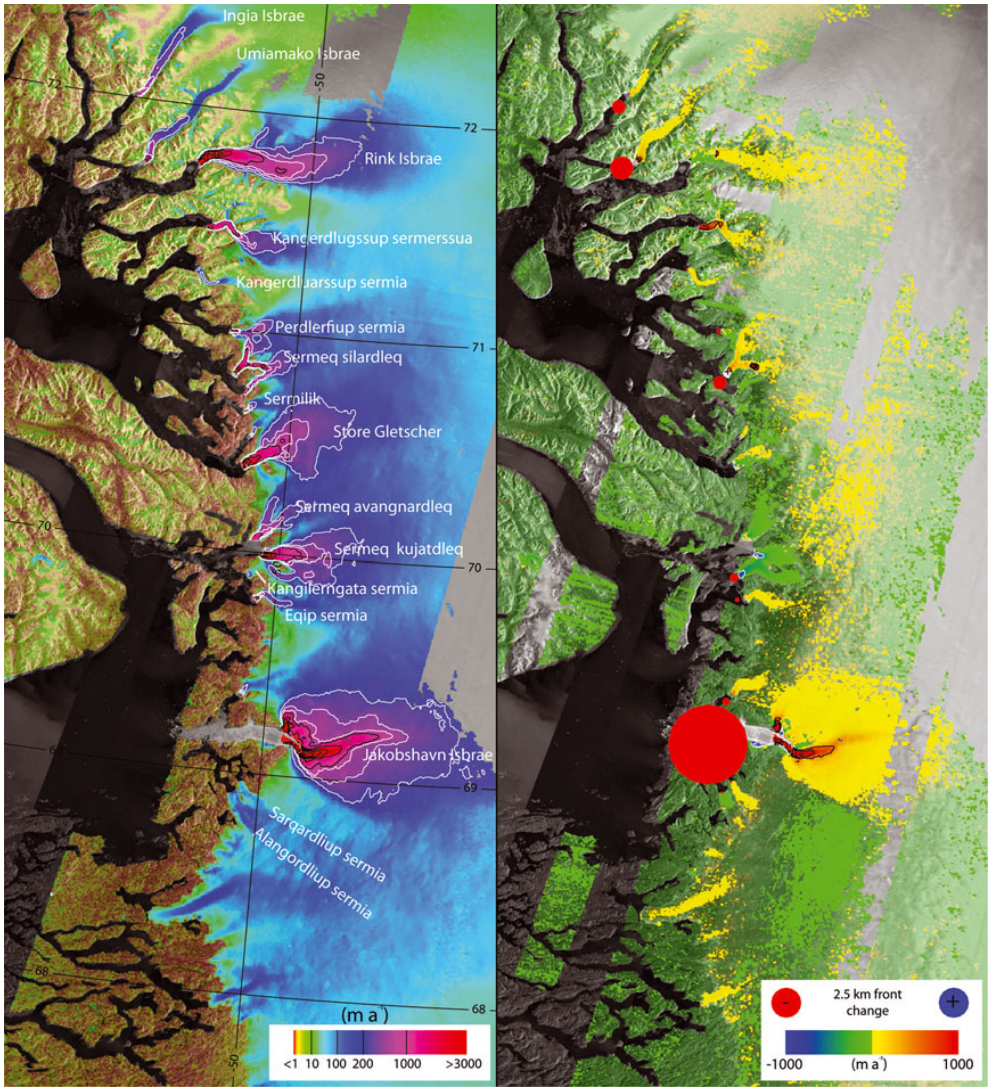

Figure 3.2: *(Left) Ice flow speed for 2005/2006 in the western coast of Greenland from InSAR. (Right) The difference in flow speed with respect to 2000/2001. From Joughin et al. (2010).*

3.3 Increased thinning

The changes of the GrIS have also been observed using repeat-track radar and laser altimetry from satellites (Slobbe et al., 2008; Pritchard et al., 2009) and airplanes (Krabill et al., 2000, 2004). The altimetry studies, show significant thinning in the marginal zones of the ice sheet, which corresponds well with the observed increase in flow velocity (Abdalati et al., 2001; Thomas et al., 2008; Howat et al., 2008b; Thomas et al., 2009). The thinning is a result of increased melt and flow dynamics. The altimetry results show, that the ice

sheet is thickening in the central part, but that this increase is small compared to the large marginal thinning. A map of elevation changes derived from aircraft laser altimetry is shown in Fig. 3.3 (Krabill et al., 2004).

Results show, that the marine-terminating glaciers have thinned, at a much higher rate than the land-terminating glaciers. This indicates, that the thinning of the land-terminating glaciers is caused by the changes in air temperature, while the thinning of the marine-terminating glaciers is caused by ice dynamics (Sole et al., 2008).

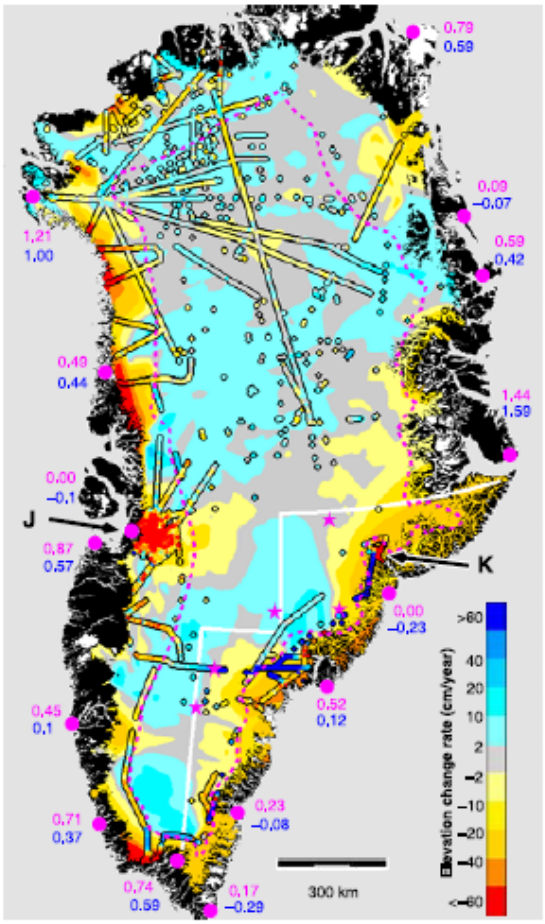

Figure 3.3: *Rate of elevation changes of the GrIS from aircraft laser altimetry for the period 1993-2003. From Krabill et al. (2004).*

3.4 An increasing mass loss

The wide spread thinning of the GrIS, and the increased ice flow speed indicate, that the GrIS is loosing mass. The total MB is of particular interest, since this can be translated directly into a the sea-level change (Leuliette et al., 2004; Shepherd and Wingham, 2007; Cazenave et al., 2009).

Slobbe et al. (2008) convert elevation changes from satellite altimetry (2003-2007) into mass changes, using a simple assumption of the snow and ice densities. This results in a MB estimate of $-139 \pm 68\,\mathrm{Gt\,yr^{-1}}$. In Krabill et al. (2004), elevation changes derived from airborne laser altimetry are combined with modeled snowfall and summer melt. The result of this study is a MB for 1993-1999 of $-55 \pm 3\,\mathrm{Gt\,yr^{-1}}$ and $-73 \pm 11\,\mathrm{Gt\,yr^{-1}}$ for the period 1997-2003.

Velocity maps generated by InSAR can be used together with ice thickness to determine discharge, and the discharge estimates can be combined with surface mass balance (SMB) modeling to derive a MB estimate of the ice sheet. van den Broeke et al. (2009) use this mass budget approach, and find a MB of $-237 \pm 20\,\mathrm{Gt\,yr^{-1}}$ for 2003-2008. The mass budget method is also used by Rignot and Kanagaratnam (2006), in which three mass loss estimates are presented; $83 \pm 28\,\mathrm{Gt\,yr^{-1}}$ in 1996, increasing to $127 \pm 28\,\mathrm{Gt\,yr^{-1}}$ in 2000, and then reaching $205 \pm 38\,\mathrm{Gt\,yr^{-1}}$ in 2005. These estimates are based on InSAR, and deviations from a zero-anomaly (SMB) estimate.

Many studies of GrIS MB are based on GRACE data (e.g. Velicogna and Wahr (2005)). Most of the studies are based on the monthly global gravity models, which are delievered by various GRACE processing centres. Velicogna (2009) finds a mass loss of $230 \pm 33\,\mathrm{Gt\,yr^{-1}}$ during the period 2002-2009 based on CSR solutions, see Fig. 3.4, which shows the time series of ice mass changes for the GrIS, based on GRACE monthly mass solutions. Blue is the unfiltered mass change estimates, red is the filtered data using a 13 months window, and green is the best fitting quadratic trend.
The MB estimate of $-219 \pm 21\,\mathrm{Gt\,yr^{-1}}$ found by Chen et al. (2006) for the period 2002-2005 is also based on CSR data. Wouters et al. (2008) use a forward modelling approach to make mass changes fit the GRACE observations which are derived from CSR models. This study estimates MB of individual drainage basins, but finds a total MB of $-179 \pm 25\,\mathrm{Gt\,yr^{-1}}$ for 2003-2008. Slobbe et al. (2009) obtain MB estimates in the range -128 to -218 $\mathrm{Gt\,yr^{-1}}$ based on data products from four different processing centres (CNES, DEOS, CSR and GFZ). The Ramillien et al. (2006) result of $-118 \pm 14\,\mathrm{Gt\,yr^{-1}}$, is derived from the 10-day solutions from CNES covering the period 2002-2005.
In the recent paper by Wu et al. (2010), a somewhat smaller MB of $-104 \pm 23\,\mathrm{Gt\,yr^{-1}}$, is found. In this study, an inversion scheme is applied in order to estimate GIA, and ice mass loss simultaneously.

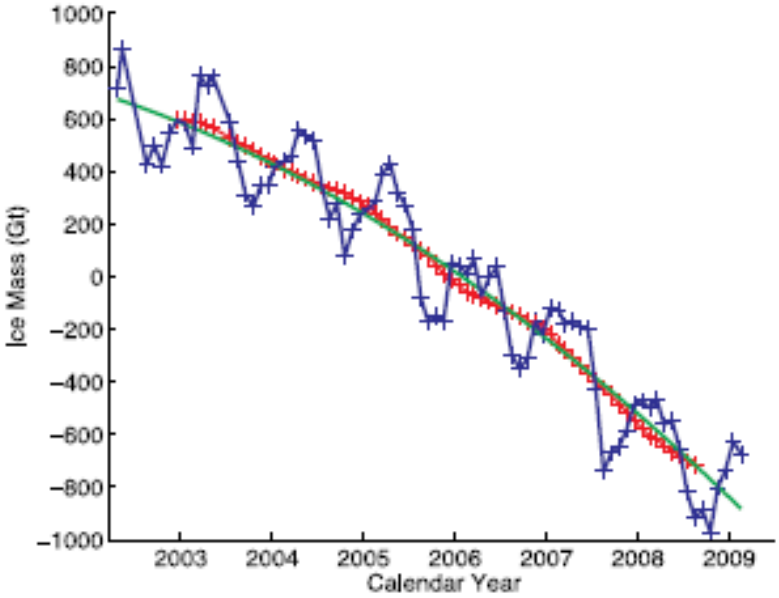

Figure 3.4: *Time series of ice mass changes for the GrIS based on GRACE monthly mass solutions. Blue is the unfiltered mass change estimates, red is the filtered data using a 13 months window, and green is the best fitting quadratic trend. By fitting a linear trend to the data, a mass loss of* 230 ± 33 *Gt yr*$^{-1}$ *is obtained. From (Velicogna, 2009)*

The results in Luthcke et al. (2006), are derived from the GRACE range rates, used in a mascon approach, with a resolution in time of 10 days. A mass change result of $-101 \pm 15\,\mathrm{Gt\,yr^{-1}}$ is derived for 2003-2005.
As already mentioned, the various methods all have limitations but when summarising the various MB results a picture is revealed; the GrIS is indeed undergoing rapid changes.

All of the mass loss estimates are shown in Fig. 3.5. Some of the MB results are published in units of $[\mathrm{km^3\,yr^{-1}}]$, and these are converted into $[\mathrm{Gt\,yr^{-1}}]$ assuming an ice density of $0.91\,\mathrm{Gt\,km^{-3}}$. The different methods are represented by different colours, with the gravity method results shown in red, the elevation change method results in green, and the mass budget method results in blue. It is clear from this figure, that there is still a lack of consensus on the MB of the GrIS, when using different methods for the same period of time, or even when using the same data, but with different assumptions and approaches. This figure highlights the importance of a continued effort in constraining the MB of the GrIS.

In spite of the differences in the MB estimates, Fig. 3.5 shows, that there is a negative trend in the MB estimates in time, indicating that the annual mass loss is increasing.

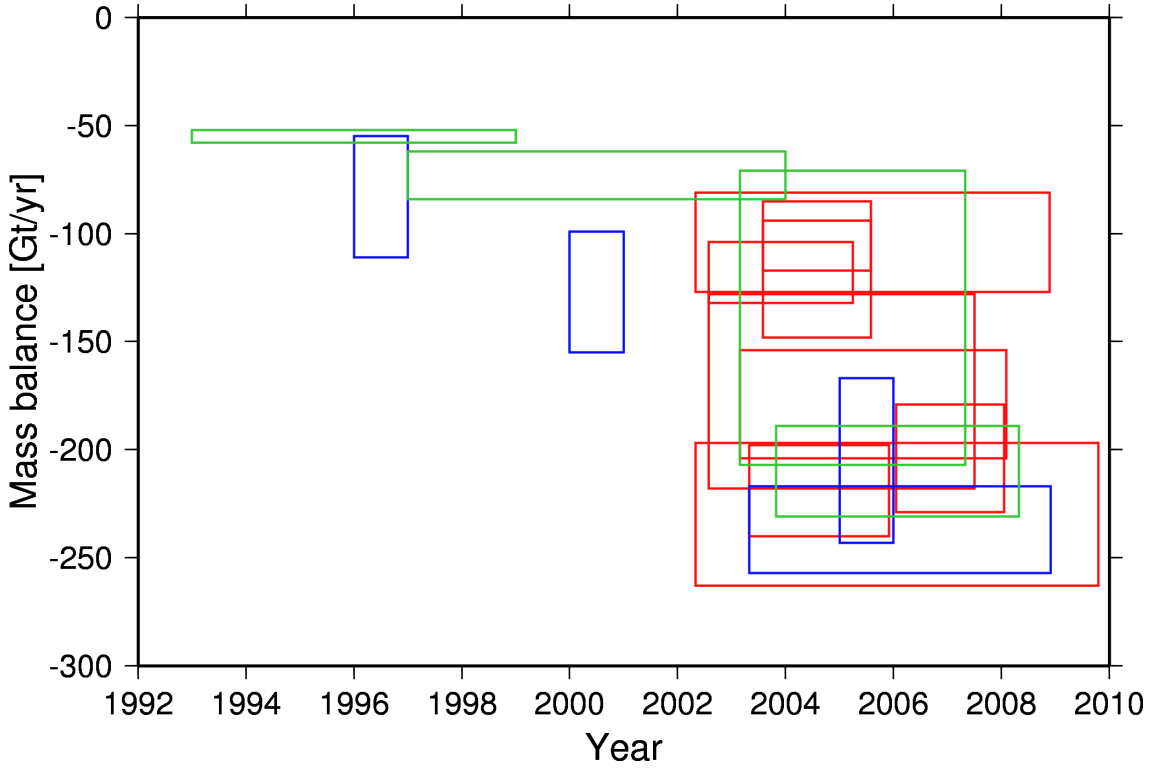

Figure 3.5: *Published mass balance estimates of the GrIS. Red indicates results based on the gravity method, blue indicates those based on the mass budget method, and green indicates the results based on the elevation change method.*

Chapter 4

The Gravity Recovery and Climate Experiment (GRACE) mission

In this Ph.D. thesis, satellite-gravimetry data, provided by GRACE since 2002, are used to determine the mass balance of the GrIS. This chapter provides an overview of the GRACE mission and its objectives. Furthermore, the different levels of GRACE data are introduced, and the level-2 data, provided by different processing centres, are described in more detail.

4.1 Mission objectives

The GRACE twin satellites (Fig. 4.1) were launched on March 17th 2002. The mission is a joint German-American project between Deutsche Forschungsanstalt für Luft und Raumfahrt (DLR) and National Aeronautics and Space Administration (NASA).

The primary goal of the GRACE satellite mission is to obtain accurate global models of the Earth's gravity field, of both the static and time varying component (Tapley et al., 2004). The determination of a very precise geoid is important for both accurate positioning and orbit determination. The time-variations in the gravity field can be used in many different applications, for instance in ice sheet mass balance studies (e.g. Luthcke et al. (2006); Chen et al. (2006); Wu et al. (2010)), in hydrology (e.g. Andersen et al. (2005); Krogh et al. (2010)) or in GIA studies (e.g. Wahr and Velicogna (2003); Steffen et al. (2008)). A secondary objective of the GRACE mission, is to record globally distributed profiles of the atmosphere and ionosphere, through measurements of the GPS signal excess delay. These profiles are used in research as well as in weather forecasts.
The planned lifetime of the mission was originally 5 years. As the satellites are still operating today, the mission has been extended to 2015.

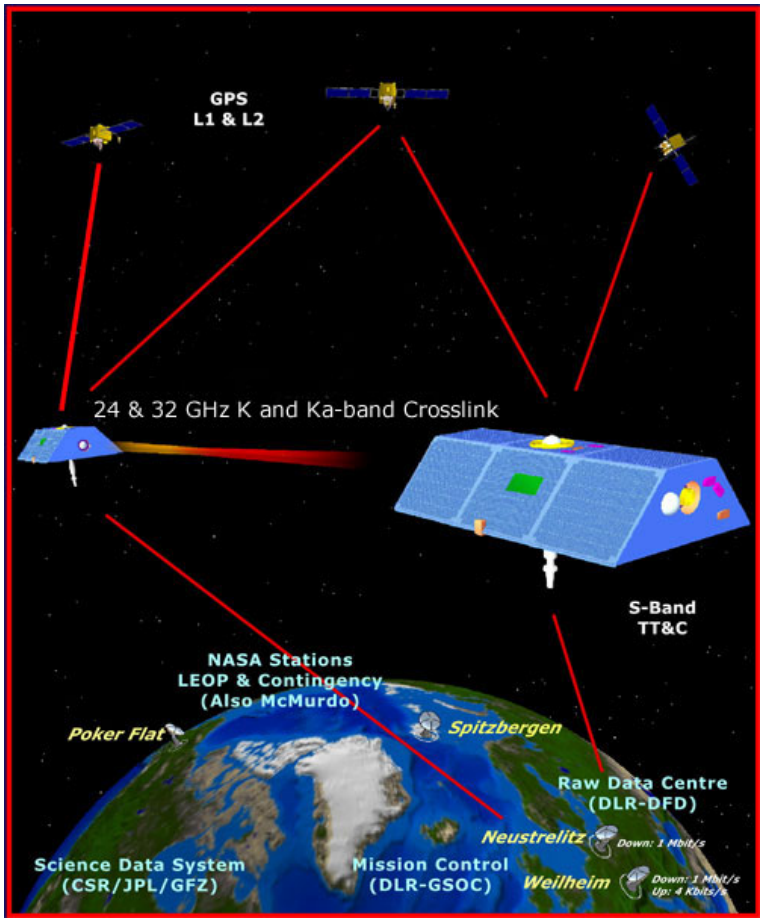

Figure 4.1: *The two LEO GRACE satellites orbiting the Earth. Their precise positions are tracked by GPS. Illustration adapted from http://www.tacc.utexas.edu/news/feature-stories/2005/state-of-grace*

4.2 Measurement principle

The two low Earth orbiting (LEO) GRACE satellites act as test masses in the Earth's gravity field. The two satellites are flying in the same orbit, separated by a distance of approximately 220 km. A change in gravitational acceleration results in a change in the velocity, and hence the orbital motion, of the satellites. This is observed as a change in distance between the front and tailing satellite. From the observed variations in the inter-satellite distance, position and acceleration, the Earth's gravity field can be determined. The mission science data consist of inter-satellite range rate measurements while accelerations, GPS and attitude measurements are made for each satellite.
The satellites are moving in a near-polar orbit with an inclination of 89 °, and the positions are precisely determined by the high-altitude GPS satellites (GRACE-GFZ, 2010). The satellite altitude of 450-500 km is a compromise between the high resolution gravity field, which could be obtained at a lower altitude, and the atmospheric drag on the satellites that decreases with altitude.

When deriving gravity models from the range and range rate data, non-gravitational accelerations, such as solar radiation pressure and atmospheric drag must be taken into account.

4.3 Instruments on-board the GRACE satellites

The two GRACE satellites are identical except from the frequencies of the communication signals.
The key scientific equipment on-board GRACE is the JPL K-Band ranging instrument, which measures the range and range rate between the satellites, with very high precision. The inter-satellite communication is running continuously, via a microwave K-band frequency link. An S-band radio frequency is used for ground communications (GRACE-CSR, 2010).

An accelerometer, placed at the center of mass of each satellite, measures the sum of the non-gravitational forces such as the atmospheric drag. On each satellite a star camera assembly is placed used to determine the orientation of the satellites in space.
The GPS receivers on-board the satellites enable position determination with an accuracy on the cm level. Each satellites is equipped with GPS antennas.
In addition, the GRACE satellites carry a laser retro reflector. It is attached to the down-looking side of the satellite, and is used for orbit verification by terrestrial measurements.

4.4 GRACE gravity data

The GRACE gravity data are categorized into different levels according to the level of processing performed. The observed range rates between the two satellites represent the sum

of all forces acting on the satellites, and it includes both gravitational and non-gravitational forces. However, it is possible to determine the gravitational field of the Earth, as the non-gravitational forces are measured by the accelerometers.

The level-0 data are the raw GRACE data, which consists of the binary encoded satellite communication. The Raw Data Center (RDC) is responsible for dividing the raw data stream into science and housekeeping data (Bettadpur, 2003). This is done for each of the two satellites once every pass.

The level-1 data are divided into level-1A and level-1B data. The level-1A data are the result of applying sensor calibration factors to the level-0 data in order to convert it to engineering units. Data quality tags are added, and when needed, time tags are corrected. The level-1 data are completely reversible to the level-0 data.
Irreversible processing of the level-0 and level-1A data has been applied to create the level-1B data, which are all the input needed for deriving gravity field and orbit determination. The level-1B data include orbit information, inter-satellite range, range-rates, and non-gravitational accelerations.

The level-2 data are the monthly gravity fields and related products. The series of gravity fields are derived from processing of the level-1B data. The monthly gravity fields are provided as sets of spherical harmonic coefficients to a specific maximum degree and order, describing the exterior gravity potential of the Earth. It is the level-2 data, that are used in this thesis, and thay are described in more detail in Sect. 4.4.1.

Several GRACE data users have developed value-added GRACE products, such as time-series of surface mass anomalies, an interactive tool for calculating error-corrected mass anomalies in regional or global time series, and an interactive tool for calculation error-corrected mass anomalies in regional or global time series. These and similar products, are referred to as level-3 data products (GRACE-Tellus, 2010; CU-GRACE, 2010; ICGEM, 2010).

4.4.1 Level-2 data

The three GRACE project processing centres **CSR** (Centre for Space Research, University of Texas), **GFZ** (GeoForschungsZentrum) and **JPL** (Jet Propulsion Laboratory), are responsible for continuously providing the level-2 monthly gravity fields. The most recent release from these centres is the release 4 gravity fields (release 4.1 for JPL). It is available to the public via the PO.DAAC system (http://podaac.jpl.nasa.gov/grace) and ISDC (http://isdc.gfz-potsdam.de/grace).

The Institute of Theoretical Geodesy (ITG) at the University of Bonn provides GRACE gravity data products, called ITG-Grace2010 (Mayer-Gürr et al., 2010). Besides monthly gravity models, ITG-Grace2010 consists of a static, high resolution gravity field, as well as

daily models (Mayer-Gürr, 2006; Kurtenbach et al., 2009).
The unconstrained monthly ITG-Grace2010 models (for future reference just denoted **ITG**) are created without applying any regularization. The ITG monthly gravity models are available via ftp://skylab.itg.uni-bonn.de/ITG-Grace2010/monthly/ITG-Grace2010/.

A GRACE level-2 data product is also derived by Centre National d'Etudes Spatiales/-Groupe de Rescherches de Géodésie (CNES/GRGS) (Lemoine et al., 2007). The **CNES** models are provided as 10-day solutions, recovered from both GRACE and LAGEOS (Laser Geodynamics Satellites) SLR data. The latter provide most of the information needed for the $\bar{C}_{20}$ coefficient.
A tailored regularization is performed on each individual Stokes coefficient (Bruinsma et al., 2010), such that the 10 day solutions are stabilized towards a static gravity model. The CNES data are available at http://grgs.obs-mip.fr/index.php/fre/Donnees-scientifiques/Champ-de-gravite/grace.
The time span of solutions from the different processing centres are shown in Fig. 4.2.

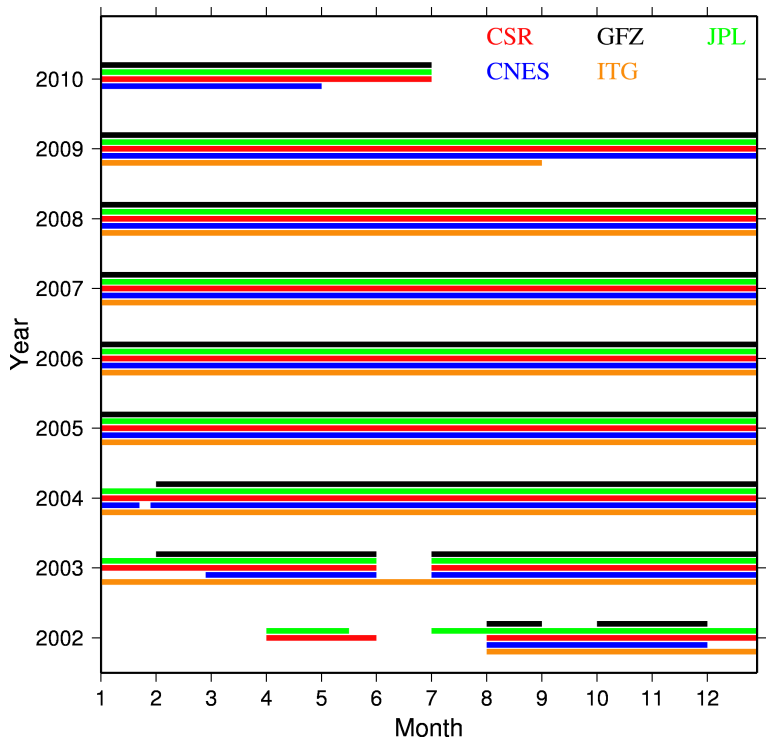

Figure 4.2: *The time span of the level-2 GRACE data used in this study. CSR is shown in red, GFZ in black, JPL in green, CNES in blue and ITG in orange.*

The GRACE level-2 data are provided as sets of fully normalized spherical harmonic coefficients $\bar{C}_{lm}$ and $\bar{S}_{lm}$, also called Stokes coefficients.
The gravitational acceleration, g, is the gradient of the gravity potential, V, which can be expressed as (Heiskanen and Moritz, 1967):

$$V(r,\theta,\lambda) = \frac{GM}{r}(1 + \sum_{l=1}^{\infty}\left(\frac{a_e}{r}\right)^l \sum_{m=0}^{l} \bar{P}_{lm}(sin\phi)[\bar{C}_{lm}\cos m\lambda + \bar{S}_{lm}\sin m\lambda]), \tag{4.1}$$

where G is the gravitational constant of 6.67428×10^{-11} $\mathrm{m^3kg^{-1}s^{-2}}$, M is the mass of the Earth, a_e is the equatorial radius of the Earth, r is the distance to the Earth's center, (θ, λ) is the geographical latitude and longitude, and $\bar{P}_{lm}(sin\phi)$ is the fully normalized associated Legendre polynomial of degree l and order m. Equation 4.1 is an infinite series, but in practice, it is truncated at a certain degree and order N_{max} (see Table 4.1). This truncation level determines the spatial resolution of the potential field represented by the series (or model). If the origin of the reference frame is chosen to coincide with the center of mass of the earth, the $l = 1$ coefficients are all zero.
The spatial resolution, S_{res}, and the truncation level, N_{max}, are inverse proportional:

$$S_{res}[km] = \frac{20000}{N_{max}}. \tag{4.2}$$

The gravity field estimates are derived from a linear least squares adjustment of the orbit, and gravity from an optimally weighted combination of GRACE data (Bettadpur, 2007a). Thus, the equations of motion of the satellites are propagated using a background (or a priori) model. Part of the background model is a static (long-term mean) gravity field model, and the background gravity models used by the different processing centres are listed in Table 4.1.

Table 4.1: *Short description of GRACE level-2 data.* [1] *GIFF22a is generated from 22 months of RL02 data, GGM02C and EGM96*

Processing Center	**Release**	**N$_{max}$**	**Background gravity model**
CSR	4	60	GIFF22a [1]
GFZ	4	120	EIGEN-GL04C
JPL	4.1	120	GIFF22a [1]
CNES	2	50	EIGEN-GRGS.RL02.MEAN-FIELD
ITG	1	120	ITG-Grace2010

The background model also contains contributions from time-varying phenomena such as tides, sun/moon/planet contributions, atmospheric and ocean variations. These contributions are described in more detail in the level-2 processing standards documents by Bettadpur (2007b),Watkins (2007), and Flechtner (2007).

The solutions, provided by the different processing centres, are based on the same GRACE data but they may be regarded as independent due to differences in processing strategies, orbits, noise reduction, and background models.
CSR, GFZ, and CNES provide both formal and calibrated error estimates on the Stokes coefficients, while JPL and ITG provide only the formal error estimates.

Chapter 5

The Ice Cloud and land Elevation Satellite (ICESat) mission

The laser altimetry data collected by ICESat in the period October 2003 to March 2008, is used to estimate the GrIS mass balance (Sørensen et al., 2010a). This chapter provides an overview of the ICESat mission and mission data. Furthermore, the data culling performed is described. Supplementary information on the ICESat data and the data culling is found in Sect. 2 of Sørensen et al. (2010a).

5.1 Mission objectives

ICESat was a laser altimetry satellite mission (Fig. 5.1(a)), launched on January 13th, 2003, which provided multi-year science data until October 2009. The satellite was decommissioned from operation in August 2010. ICESat was part of NASA's Earth observing system (NASA-ICESat, 2010).
The primary goal of the ICESat mission was to measure the topography of the ice sheets and its variations in time, to estimate the mass balance. Other objectives were to obtain a better knowledge of the surface characteristics of both sea ice and ice caps, to measure cloud and aerosol heights, and to determine land topography and vegetation characteristics (Zwally et al., 2002b; NASA-ICESat, 2010).

A follow-on ICESat mission (ICESat-2) is planned for launch in late 2015. To bridge the gap between the two ICESat missions, NASA initiated a project called IceBridge (NASA-IceBridge, 2010). In IceBridge, the polar ice is mapped by airborne LiDAR and a suite of other instruments.

5.2 Instruments on-board ICESat

The Geoscience Laser Altimeter System (GLAS) was the sole scientific instrument carried on ICESat (Abshire et al., 2005; NASA-GLAS, 2010).

The GLAS instrument operated at a frequency of 40 pulses per second, and illuminated spots on the ground with a diameter of 70 m. The laser spots were separated by an along-track distance of approximately 170 m. The GLAS instrument had three lasers, which were in operation one at a time. Two different signal frequencies were use; an infrared pulse to determine surface topography and a green pulse used for atmosphere measurements (Schutz et al., 2005).
The GLAS measurement duty cycle needed to be re-planned right after the launch. The three GLAS lasers had some unforeseen problems, that made it necessary to reduce the measurement duty cycle from 365 days a year to three campaigns of approximately 33 days a year. Since 2003, ICESat operated in a 91 day repeat track orbit, with a sub cycle of 33 days. The precise position of the satellite is obtained by two GPS receivers. The attitude of the satellite, and hence the direction of the laser beam was determined by gyroscopes and star cameras.

5.3 Measurement principle

The simple measurement principle of satellite (laser) altimetry is illustrated in Fig. 5.1(b). The altimeter emits an electromagnetic signal, which is reflected from the Earth's surface, and then received by the satellite. The two-way travel time of the signal is a measure of the distance from the altimeter to the surface, since the electromagnetic signal travels with the speed of light. When knowing the precise attitude and position of the satellite (and hence the altimeter), the surface elevation can be determined.
The emitted signal is Gaussian in shape, and the characteristics of the return signal (the waveform) contains information on the surface characteristics. The shape of the waveform is a result of different factors such as the height distribution within the laser footprint, clouds, saturation and forward scattering (Brenner et al., 2003). ICESat operated in a near-polar orbit, with an inclination of 94°, and an altitude of approximately 600 km. The satellite orbit was a compromise between the wish for global coverage and the need for ground-track crossovers.
The satellite could perform pointing maneuvers to compensate for orbit drift, and to ensure that the laser was always pointed towards a reference track (Luthcke et al., 2005).

5.4 ICESat data

The processing of the GLAS waveforms results in 15 different products, which are listed in Table 5.1. The data are distributed by the National Snow and Ice Data Center (NSIDC) as binary files. All of the parameters in the ICESat data files are determined from the digitized waveforms of the return signals. In the data processing, the waveforms are evaluated, and different quality indicators are applied to the individual measurements.The processing is done by the ICESat Science Investigator led Processing System (I-SIPS).

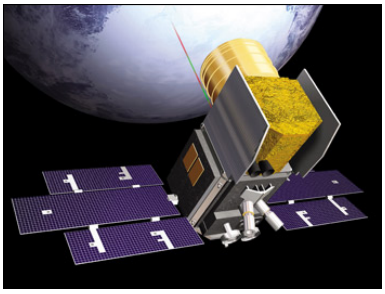

(a)

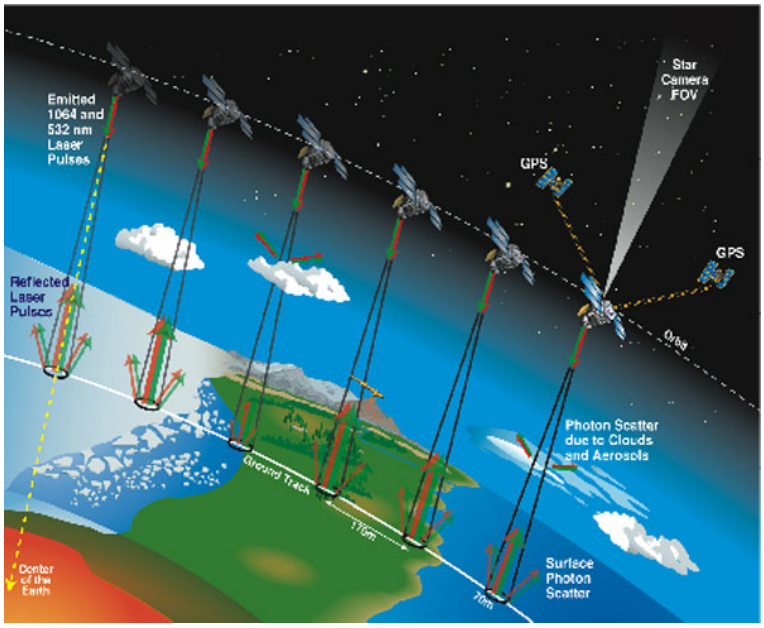

(b)

Figure 5.1: *(a) Illustration of ICESat (http://nasa.gov/centers/goddard/images/) (b) Measurement principle of satellite altimetry (http://www.aviso.oceanobs.com/en/altimetry/).*

5.4.1 GLAS/ICESat L2 Antarctica and Greenland Ice sheet Altimetry Data

The GLAS/ICESat L2 Antarctica and Greenland Ice Sheet Altimetry Data - or in short GLA12 - consist of surface elevations for the large ice sheets (Zwally et al., 2010), along with associated parameters (NSIDC, 2010). Each binary GLA12 data file contains measurements from about 14.7 orbits of the satellite.

To convert range measurements to elevations, several geodetic corrections have been applied. These corrections and data quality indicators are provided to the user, making it possible to perform data culling, suited for the specific investigation.
Release 31 is the most recent version of the GLA12 data sets. This release includes improved corrections for saturation effects compared to earlier releases. A description of the time span of the data and number of measurements used in this study, is given in Table 1 of Sørensen et al. (2010a).

5.5 ICESat data culling

The corrections, and quality indicators taken into account in this study, are shortly described in Sørensen et al. (2010a), Sect 2.1. The number of data from the GrIS before and

Table 5.1: *Description of GLAS products.*

GLAS data products	Description
GLA01	Global Altimetry Data
GLA02	Global Atmosphere Data
GLA03	Global Engineering Data
GLA04	Global Laser Pointing Data
GLA05	Global Waveform-based Range Corrections Data
GLA06	Global Elevation Data
GLA07	Global Backscatter Data
GLA08	Global Planetary Boundary Layer Data
GLA09	Global Cloud Heights for Multi-layer Clouds
GLA10	Global Aerosol Vertical Structure Data
GLA11	Global Thin Cloud/Aerosol Optical Depths Data
GLA12	Antarctic and Greenland Ice Sheet Altimetry Data
GLA13	Sea Ice Altimetry Data
GLA14	Global Land Surface Altimetry Data
GLA15	Ocean Altimetry Data

after the data culling is listed in Table 1 in ibid.
Here, the parameters and quality indicators evaluated in the data culling are described in further detail. The data culling parameters are chosen to remove measurements which potentially have larger than average uncertainty.

The rejection criteria applied can/will be partly overlapping. The criteria used are adapted from other studies (e.g. Smith et al. (2009)) and from NSIDC (2010), and they are applied in the order in which they are listed in the following. The parameters used are described in NSIDC-Parameters (2010), and the spatail distribution of the measurements rejected from the various parameters is shown in Fig. 5.2.
The quality flag $i\_ElvuseFlg$ indicates whether an elevation measurement should be used or not. $i\_sigmaatt$ is an attitude quality indicator, which can have values of 0 (=good), 50 (=warning) or 100 (=bad). Here, we accept only measurements with $i\_sigmaatt = 0$, since uncertainty in the attitude translates directly into an error in the elevation (Schutz, 2002; Bae and Schutz, 2002).
Based on the $i\_AttFlg1$ flag, measurements associated with large off-nadir angle (outside the limits) are rejected. This is chosen, since the geolocation of the points associated with a large off-nadir pointing angle, are determined using another scheme than the near-nadir measurements and are likely associated with a larger error due to the off-nadir pointing (Fricker et al., 2005; Luthcke et al., 2005).

Table 5.2: *Data culling statistics*

Parameter	**% of rejected data**
i_ElvuseFlg	4.5
i_sigmaatt	1.9
i_AttFlg1	65.5
i_SatCorr	6.5
i_numPk	0.5
i_IceSVar	21.1

The $i\_SatCorrFlg$ indicates whether a measurement is saturated or not. If the measurement can not be corrected by the saturation correction, the data are rejected.
i_numPk contains information on the number of peaks in the return signal, and we use only measurements with $i\_numPk = 1$.
Over ice sheets a simple single peak Gaussian return is expected but the presence of clouds, highly variable topography, or fog can affect the waveform. $i\_IceSVar$ contains information on the standard deviation of the difference between the functional fit and the received echo, using standard parameters. Measurements for which $i_IceSVar > 40$mV are rejected.
It is seen in Fig. 5.2 that data rejected by $i\_ElvuseFlg$ and $i\_IceSVar$ are distributed over the entire ice sheet, while the measurements rejected from $i\_SatCorrFlg$ and i_numPk are located in the coastal areas. It is also seen that $i\_AttFlg1$ and $i\_sigmaatt = 0$ reject distinct tracks.
Table 5.2 contains information on the amount of the rejected data is caused by the various parameters.

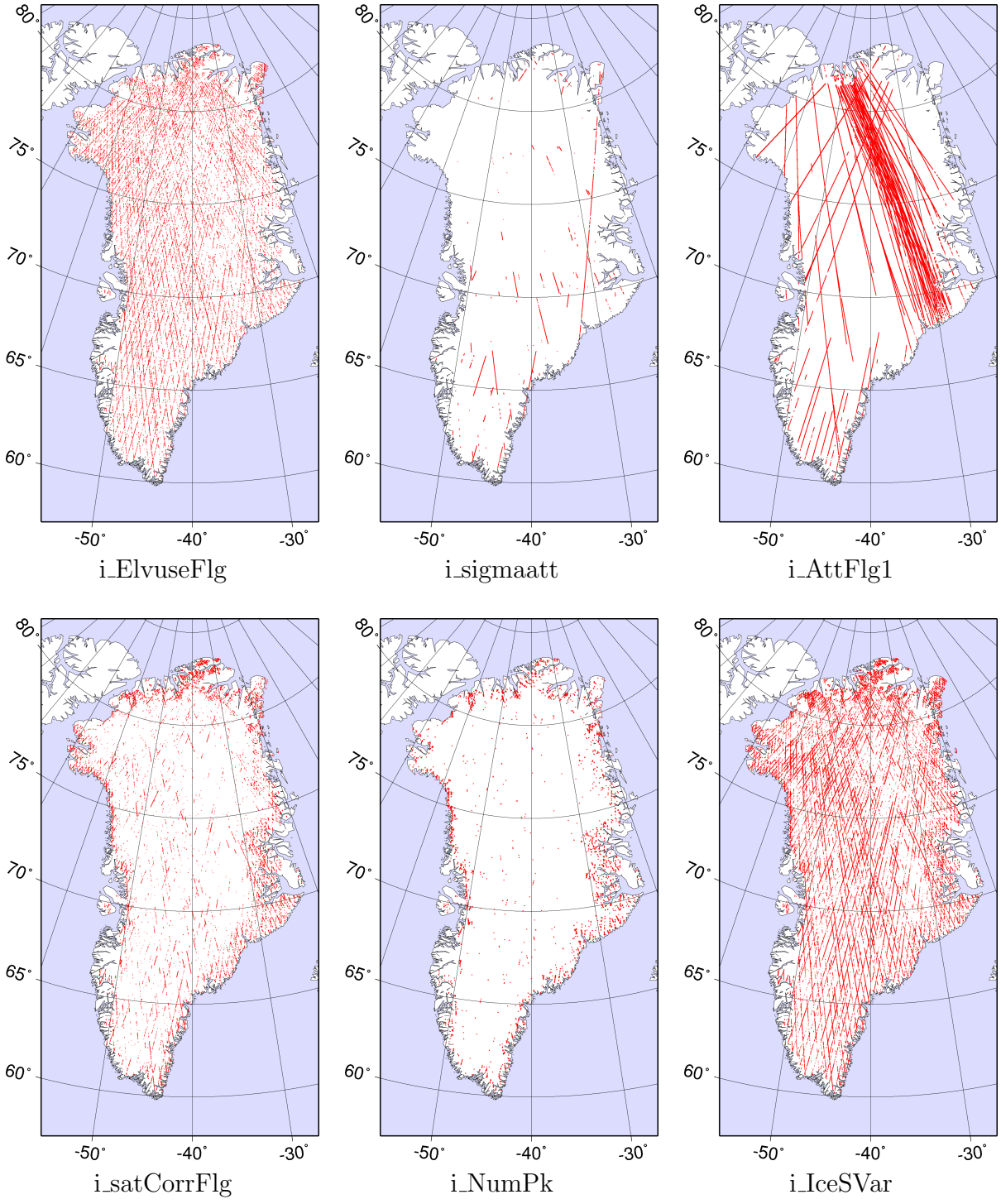

Figure 5.2: *Regional distribution of rejected data based on the different rejection parameters.*

Chapter 6

Glacial isostatic adjustment

In this chapter, the principle of glacial isostatic adjustment (GIA) is described.
When using satellite altimetry (e.g. ICESat) or gravimetry (e.g. GRACE), to determine the present-day changes of the GrIS, it is necessary to separate the signals caused by present-day mass changes, and those related to GIA (Wahr and Velicogna, 2003; Barletta et al., 2008; Wu et al., 2010). The GIA processes modify both the Earth's shape and gravity field, hence the GIA contribution must be estimated, and corrected for in studies of ice sheet mass balance.
The publicly available program SELEN (version. 2.9) is also introduced in this chapter (Spada and Stocchi, 2007). SELEN is used for GIA calculations in this study.
For a state of the art report on GIA modelling, the reader is refered to Whitehouse (2009).

GIA is Earth's response, to changes in ice load geometry during a glacial cycle. During glaciation, the crust is suppressed by the increased ice loads, and mantle material is moved away from the centre of the loads. During, and after deglaciation, the solid Earth is returning to a state of isostatic equilibrium, by uplift and mantle material flow towards the deglaciated area (see Fig. 6.1).
The Earth shows both elastic and viscous behavior. An elastic material deforms instantaneously, when a force is applied to it, while a viscous material can flow under the applied load.
The current deglaciation began at approximately 21,000 years ago, at the LGM, at which point an amount of water, equivalent to a 115-135 m sea-level change, was stored in the ice sheets (Milne et al., 2002).
When predicting the present-day GIA signal at a given location (e.g. the rate of vertical movement or rate of gravity change), information is needed on the evolution of the past ice sheets, since this defines the force field applied to the Earth's surface. The Earth's structure and rheology (its viscoelastic properties) must also be known or assumed a priori, because these governs the isostatic response.

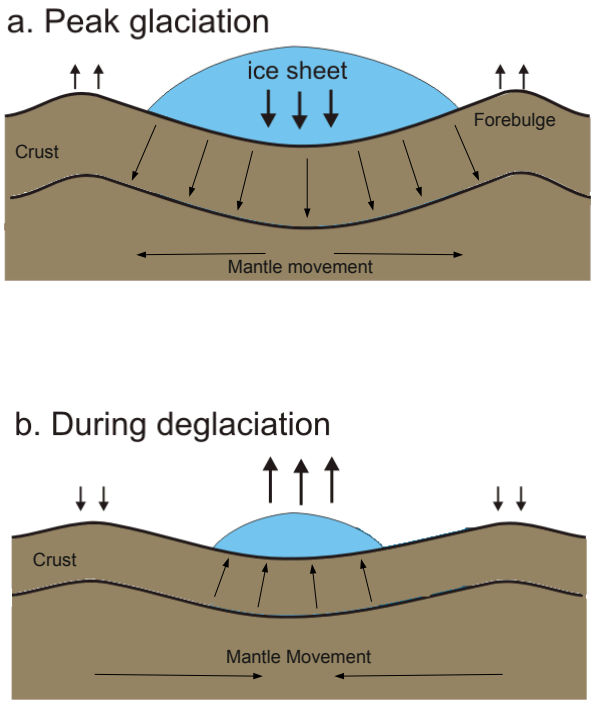

Figure 6.1: *The Earth's response to changes in ice load. During glaciation, the crust is suppressed by the ice load, and mantle material is moved away from the centre of the load. During and after deglaciation, the Earth is returning to a state of equilibrium, by uplift and mantle flow towards the deglaciated area (From: gsc.nrcan.gc.ca/geodyn/images/).*

The re-distribution of ice and water, and the resulting deformation of the Earth, can be measured today by different techniques. Time series analysis of GPS measurements are used to determine the crustal movement (both vertical and horizontal), caused by GIA (Khan et al., 2008). Data from tide-gauges time series reveal the relative sea-level (RSL) changes, and repeated altimetry also detect the vertical movement of the Earth, caused by GIA processes.
The present-day GIA signal can also be observed as changes in the gravity field, due to mass re-distribution within the interior of the Earth. The gravity changes can be observed by ground-based measurements, and by gravity satellites such as GRACE (Wahr and Velicogna, 2003).

6.1 Earth models

As mentioned, one of the input parameters needed in GIA modelling, is a model of the Earth structure. The Earth models used in GIA calculations are often simple, in the sense that a spherical geometry and rheology is assumed. Using a simple representation of the Earth is also of advantage when solving the full SLE using the pseudo-spectral method, see Sect. 6.3.
The Earth models often consist of an elastic, incompressible lithosphere of a constant thickness, together with a number of viscoelastic layers (see Fig. 6.2). The Earth is assumed to be an incompressible Maxwell body, showing both elastic and viscous behaviour. The viscosity of the mantle layers are in the range 10^{19} to 10^{24} Pa s.
Even the deeper layers of the mantle under the large ice sheets, can be deformed, due to the long time scales, and large mass redistribution of large spatial extent during a glacial cycle.

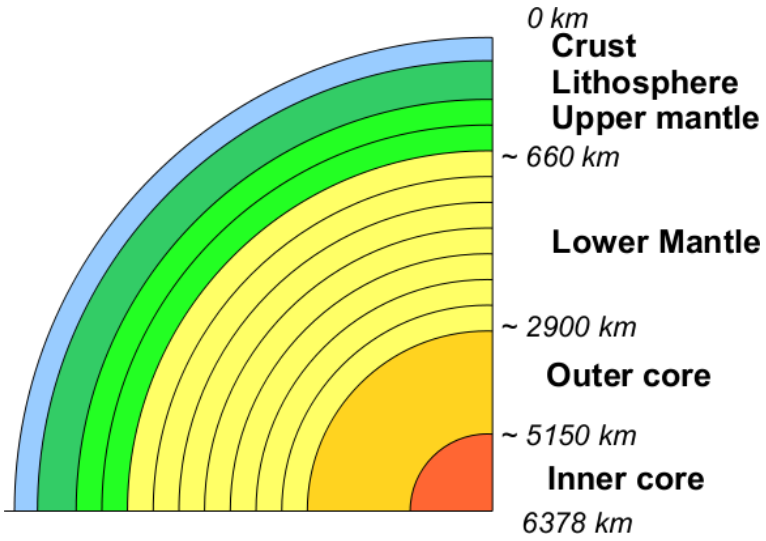

Figure 6.2: *Simple spherical Earth model used in the GIA calculations. The lithosphere is assumed elastic and with a fixed thickness. The mantle consists of a number of viscoelastic layers.*

6.2 Ice histories

An ice sheet history model is also needed as input in GIA modelling. In this study, three different ice histories are used to predict the present-day GIA contribution to both altimetry and gravimetry over Greenland.
The majority of ice sheet reconstructions (ice histories), used in GIA modelling, are constrained by geological, geomorphological and sometimes archaeological observations of past

RSL.
The RSL is the position and height of the sea relative to the land. It is a function of various processes, such as actual mass gain of the ocean, thermal expansion and uplift or subsidence of the bedrock.

The reconstruction of ice histories, is often based on fitting modelled data with observations, but this is a non-unique problem to solve, because the relative contribution of the two governing factors (the ice history and the Earth model) can not be easily separated. For Greenland, present-day changes of the ice sheet complicates the ice sheet reconstruction, since these contribute to the observations to which the model is fitted.
For the same reason, the deglaciation of the much larger Laurentide Ice Sheet, also complicates the GrIS reconstruction, since Greenland is situated upon its forebulge.
Furthermore, the GrIS evolution has not only involved a decrease in ice extend since the LGM, but also a period called the neoglacial, which included the ice sheet in some areas expanding from its post-glacial minimum, to its present-day extent (e.g. Weidick (1996)).

Observations of sea-level indicators, moraine locations and present-day uplift rates are often used to constrain the ice histories. Due to the nature of sea-level observations, only a few are dated further back than to 10 ka before present, at which time the present coast of Greenland generally became ice free (Funder and Hansen, 1996). Since Greenland is still largely ice covered, the reconstruction of the extent and thickness of the GrIS since the LGM, is primarily based on observations near the ice edge. In such a reconstruction, a compromise is made between local, high resolution observations near the ice edge, the very limited and rough thickness estimates, from the interior part of the ice sheet, obtained from ice cores, and the far-field observations (Tarasov and Richard Peltier, 2002). Far-field observations are defined as observations located far from the large LGM ice sheets, where the RSL change is dominated by the eustatic (mean) RSL change.
For these reasons, the evolution of the GrIS is not as well constrained as, for example, the Fennoscandian and Laurentide ice sheets.

Below, is a presentation of three ice histories; ICE-3G, ICE-5G and ANU05. These are used in this study, to predict the present-day GIA contribution to both altimetry and gravimetry over Greenland. When using different ice histories, it is possible to get an idea of the large uncertainties involved in GIA modelling, when comparing the present-day signal predicted from various ice histories.

6.2.1 ICE-3G (TP)

The global ICE-3G ice history (Tushingham and Peltier, 1991) was created by fitting modelled RSL results to data. ICE-3G was pioneering with respect to resolution. Prior to this model, most GIA related research had focused on constraining the Earth structure, assuming relatively simple ice sheet models.
In the creation of ICE-3G, a simple three-layered Earth model is used in the forward

modelling. Therefore, following Tushingham and Peltier (1991), the Earth model (TP) used in this study together with ICE-3G, is defined as a three-layered model, with lithosphere thickness of 120 km, upper mantle viscosity of 10^{21} Pa s and lower mantle viscosity 2×10^{21} Pa s. The TP viscosity profile is shown in green in Fig. 6.3.

6.2.2 ICE-5G (VM2)

The ICE-5G ice history is widely used in GIA modelling. Following the same strategy as with ICE-3G, RSL estimates were derived from forward modelling, and these were then compared with observations (Peltier, 2004). The reconstruction of the GrIS in ICE-5G was created, with the goal of optimally fitting both the RSL data, and the Greenland ice core project (GRIP) borehole data (Johnsen et al., 1995; Dahl-Jensen et al., 1998) in a glaciologically self-consistent way. ICE-5G is derived from more advanced modelling and on more data than the precursor, ICE-3G.

In the forward modelling used to create ICE-5G, a viscosity profile called VM2 is used. Therefore, the VM2 model must be used with ICE-5G, in GIA calculations. The VM2 elastic properties are fixed to those given in the Preliminary Reference Earth Model (PREM) (Dziewonski and Anderson, 1981). In this study, VM2 is approximated by a 90 layered mantle model, with a lithosphere thickness of 90 km. The viscosity profile is shown in red in Fig. 6.3.

6.2.3 ANU05 (KL)

The ANU05 global ice history was derived from combining field data of ice sheet margins and RSL, with simple ice sheet modelling, and inversion of uplift data. The ice sheets in the global model have been created individually, using different assumptions on the Earth's rheology. The reconstruction of the GrIS in ANU05, is called GREEN1 and is described in Fleming and Lambeck (2004).
The GREEN1 model was constrained by sea-level indicator data, consisting mainly of mollusk species, but also some biological indicators, such as drift wood samples, and marine mammal bones. It is based on the minimum and maximum reconstructions of the GrIS extent as proposed by Denton and Hughes (1981), as well as several deglaciation starting dates. Its development employed the GIA modelling tools of the Research School of Earth Sciences, the Australian National University (e.g. Johnston (1993); Johnston and Lambeck (1999)), with the ice load outside of Greenland, represented by the model of Lambeck et al. (1998). Predictions of sea-level change based on these models were compared to the observations, with the Greenland contribution computed separately and scaled to give a minimum in the variance, of the difference between the predicted and observed values.

The Earth model, denoted KL, which is used with ANU05 in this study, consists of a 90 layered Earth. The elastic lithosphere thickness is 80 km, and the upper and lower mantle viscosities 4×10^{20} Pa s and 10^{22} Pa s, respectively. These values are chosen to be

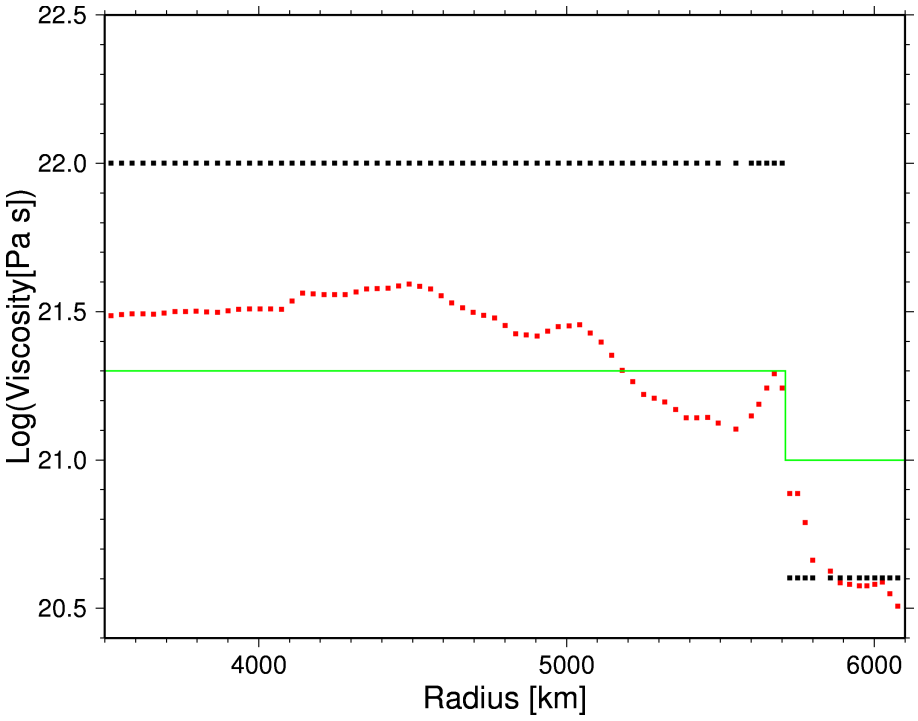

Figure 6.3: *The mantle viscosity as a function of radius. TP is shown in green, VM2 is shown in red, and KL is shown in black.*

identical to the nominal values given in Fleming and Lambeck (2004). The KL profile is shown in black in Fig 6.3.

6.3 The sea-level equation

Following the theory of Farrell and Clark (1976), the sea-level equation (SLE) can be used in GIA modelling. The SLE describes the variations of the global sea-level, both in time and space. It can be written as (Spada and Stocchi, 2006):

$$S = \frac{\rho_i}{\gamma} G_s \otimes_i I + \frac{\rho_w}{\gamma} G_s \otimes_o S + S^E - \frac{\rho_i}{\gamma} \overline{G_s \otimes_i I} - \frac{\rho_w}{\gamma} \overline{G_s \otimes_o S}, \tag{6.1}$$

where S is the sea-level change. ρ_i and ρ_w are the densities of ice and water, respectively. γ is the surface gravity acceleration, I is the ice load function, and O is the ocean function. $\otimes_i$ and $\otimes_o$ implies spatio-temporal convolution over the surface defined by the ice history and ocean function, respectively. S^E is the eustatic sea-level change, defined as:

$$S^E = -\frac{m_i(t)}{\rho_w A_o}, \tag{6.2}$$

where m_i is the mass change of the ice sheets, and A_o is the area covered by ocean. G_s is the sea-level Green's function (GF), which can be written as:

$$G_s(\alpha, t) = G_\phi - G_u\gamma, \tag{6.3}$$

with α being the co-latitude with respect to the point loads. The viscoelastic GF for the incremental potential, G_ϕ, and the viscoelastic GF for the vertical displacement, G_u, are given by:

$$\left\{ \begin{array}{c} G_\phi \frac{1}{\gamma} \\ G_u \end{array} \right\} (\alpha, t) = \frac{a_e}{m_e} \sum_{l=0}^{\infty} \left\{ \begin{array}{c} k_l \\ h_l \end{array} \right\} (t) P_l(\cos\alpha). \tag{6.4}$$

k_l and h_l are the load deformation coefficients (LDC), also called the Love numbers. a_e is the Earth's radius, m_e is its mass, and $P_l(\cos\alpha)$ is the Legendre polynomial of degree l.

In Eq. 6.1, S appears on both the right-hand and left-hand side, hence it is an integral equation, which must be solved iteratively.

6.4 GIA predictions with SELEN 2.9

SELEN 2.9 is a open source sea-level equation solver, which is used for GIA modelling. The program, written in Fortran 90, is described in detail in Spada and Stocchi (2007), and is freely available at http://www.fis.uniurb.it/spada/SELEN_minipage.html. The calculations done for this study were carried out in collaboration with G. Spada (personal communication, 2010).

In SELEN, the SLE is solved for a spherically symmetric Earth, using a pseudo-spectral method, introduced by Mitrovica and Peltier (1991). In the first iteration of solving Eq. 6.1, it is assumed that the sea-level S is equal to the eustatic sea level S^E, which is obtained from far-field observations.
SELEN is based on the SLE theory of Farrell and Clark (1976), and can be used to derive various GIA related geodetic variations, such as rate of change of geoid height, relative sea-level and vertical motion.
In SELEN 2.9, the shoreline position (defined by the ocean function), is fixed in time. This is off course a crude assumption, taking into account that during the LGM, water equivalent to more than 100 m of eustatic sea-level, was stored in the large ice sheets. The migration of shorelines will be implemented in future versions of SELEN.

The present-day GIA signals are found by convolving the viscoelastic GF's with the ice loading history, as described in Sect. 6.3. The ice history input file defines the ice thickness at a global grid, in time intervals of 1000 years.
A GIA prediction of interest in this study is the present-day rate of vertical movement, since this signal is part of the ICESat elevations measurements. The present-day rate

of vertical movement in Greenland, determined from ICE-3G (TP), ICE-5G (VM2), and ANU05 (KL) are shown in Fig. 6.4. There are obvious differences in the GIA predictions shown in Fig. 6.4.
ICE-5G (VM2) predicts the largest uplift of approximately 10 mm/yr, to be in the Northern part of Greenland (Fig. 6.4(b)). A smaller uplift of approximately 2 mm/yr is predicted along the ice sheet margin. In the interior of the ice sheet, a small subsidence is seen.
The maximum uplift predicted by ANU05 (KL) is of approximately 6 mm/yr and is located in the Northwestern part of Greenland (Fig. 6.4(c)). Besides this uplift, the ANU05 (KL) prediction is dominated by subsidence.
The prediction of rate of vertical movement in Greenland, based on ICE-3G (TP) show a very different pattern compared to the other two predictions. Uplift is seen under the entire ice sheet, with an amplitude of 10 mm/yr (Fig. 6.4(a)).

Another GIA prediction of interest, is the present-day rate of changes in gravity, since this is observed by the GRACE mission.
The rate of change of the gravity disturbance in satellite altitude (480 km) from ICE-3G (TP), ICE-5G (VM2) and ANU05 (KL) are shown in Fig. 6.5.

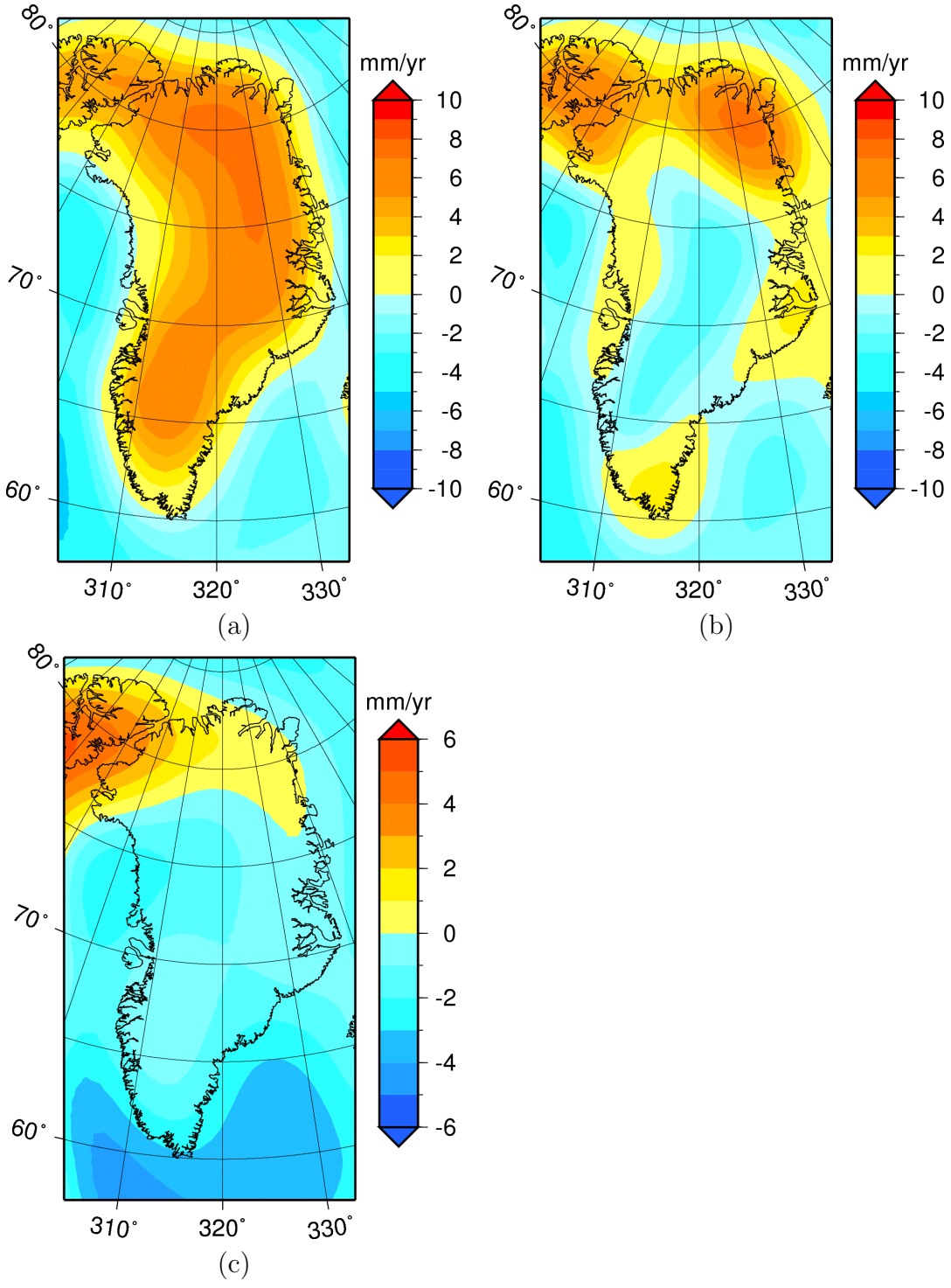

Figure 6.4: *Present-day rate of vertical movement based on (a) The ICE-3G ice history and the TP Earth model, (b) The ICE-5G ice history and the VM2 Earth model (c) The ANU05 ice history and KL Earth model.*

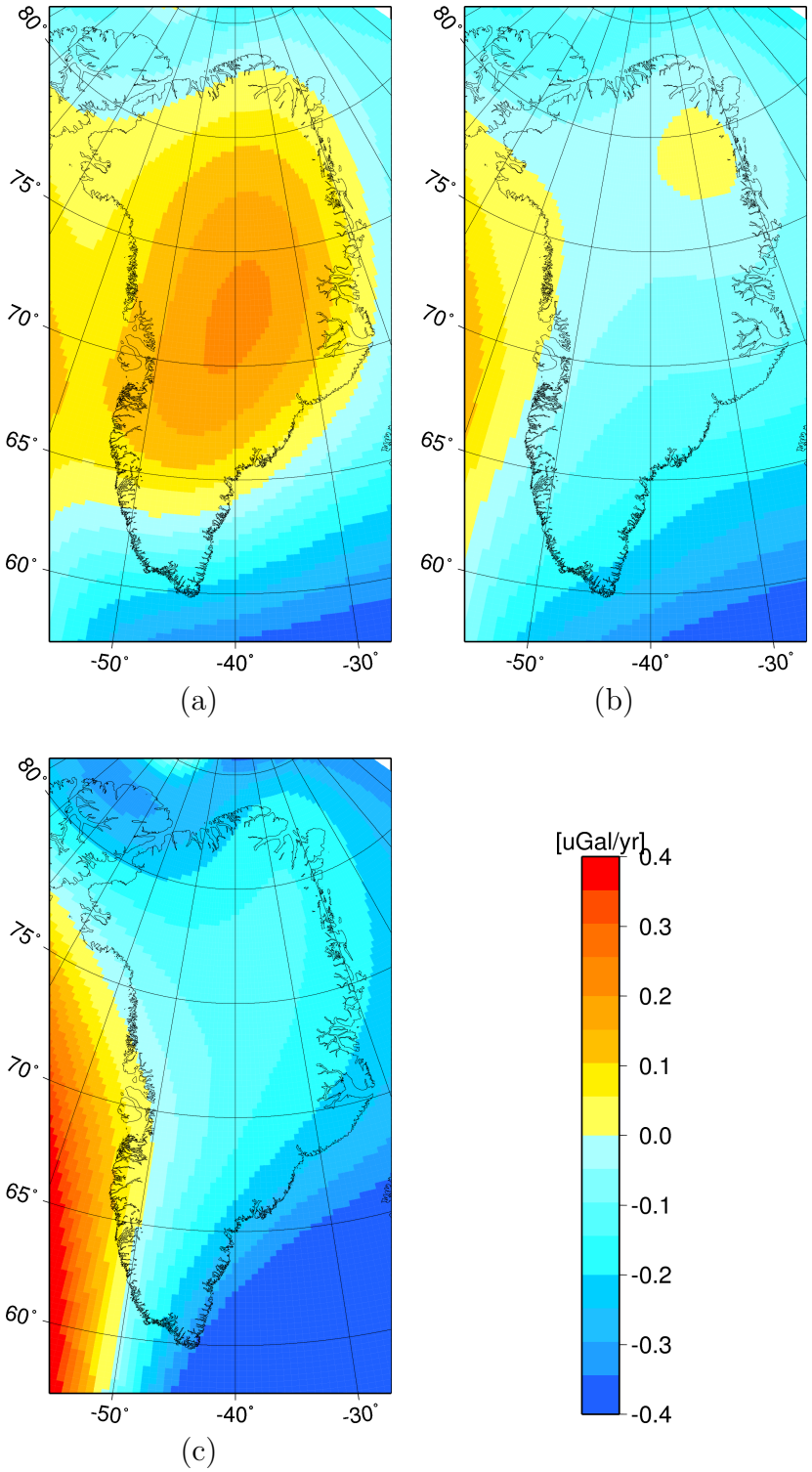

Figure 6.5: *Present-day rate of change in gravity disturbance based on (a) The ICE-3G ice history and the TP Earth model, (b) The ICE-5G ice history and the VM2 Earth model (c) The ANU05 ice history and KL Earth model.*

Chapter 7

GrIS mass balance from GRACE

In this chapter GrIS mass balance estimates, derived from five level-2 GRACE data sets (Sect. 4.4.1), are presented. The mass balance estimates are derived using the generalized inversion method, which is described in Sørensen and Forsberg (2010).
The level-2 GRACE Stokes coefficients are not used directly in the inversion scheme but need post-processing. Here, the post-processing performed on the GRACE level-2 data, is described together with the technique for deriving uncertainties in the mass balance estimates.

7.1 Low degree Stokes coefficients

The degree-0 Stokes coefficient (Eq. 4.1, Sect. 4.4.1) is proportional to the total mass of the Earth and atmosphere. This can be assumed constant, and is not used in this analysis of time variability in the gravity field.

The changes in degree-1 coefficients represent the geocenter motion, and can not be derived from GRACE data. In this study, the change in degree-1 coefficients are neglected, but it is recognized that the absence of the geocenter motion might introduce an error in the mass balance estimates (Chambers et al., 2004; Chen et al., 2005).

The $\bar{C}_{20}$ coefficient is related to the Earth's oblateness. Due to the relative short distance between the two GRACE satellites, the $\bar{C}_{20}$ coefficient is poorly determined by GRACE. The $\bar{C}_{20}$ values provided in the level-2 data show anomalous variability (e.g. Chen et al. (2005)). Therefore, the GRACE $\bar{C}_{20}$ coefficients are replaced with values derived from five SLR satellites (LAGEOS-1 and 2, Starlette, Stella and Ajisai) (Cheng and Tapley, 2004), which is a well-established technique for determining independent degree-2 coefficients. The SLR $\bar{C}_{20}$ coefficients and their associated standard deviations are continuously provided in the GRACE project Technical Note 05[1]. The $\bar{C}_{20}$ SLR substitution is not performed on the CNES models, since the $\bar{C}_{20}$ coefficients in these are determined mainly

[1]Available at: ftp://podaac.jpl.nasa.gov/pub/grace/doc/TN-05_C20_SLR.txt

from SLR (LAGEOS) (Bruinsma et al., 2010).
The variations in time of $\bar{C}_{20}$ from the various processing centres are shown in Fig. 7.1, together with those derived from SLR.
It is seen that the $\bar{C}_{20}$ coefficients provided by CSR, GFZ and ITG show large variations compared with the SLR estimates, while the JPL coefficients show very little variability. It is also seen that there is, as expected, good correlation between the CNES and the SLR $\bar{C}_{20}$ coefficients.

7.2 Isolating the surface mass contribution

As described in Chap. 6, the Earth responds to surface mass re-distributions, such as the mass loss of an ice sheet. On the short time scale of the GRACE mission, this response can be considered to be purely elastic. The elastic response of the solid Earth to present-day ice mass changes, involves changes in the gravity field. This must be removed from the GRACE data, before deriving the surface mass changes from the observed gravity changes. The method presented in Wahr et al. (1998), is adapted here for constructing surface mass change (e.g. ice) estimates from the GRACE coefficients.

A change in the GRACE Stokes coefficient, $\Delta\bar{C}_{lm}$, is assumed to be caused by both a surface mass change and the solid Earth response:

$$\Delta\bar{C}_{lm} = \Delta\bar{C}_{lm}^{\text{surf mass}} + \Delta\bar{C}_{lm}^{\text{solid Earth}} \quad , \tag{7.1}$$

with the surface mass contribution given by:

$$\Delta\bar{C}_{lm}^{\text{surf mass}} = \frac{3}{4\pi a\rho_{ave}(2l+1)} \int \Delta\sigma(\theta,\phi)\bar{P}_{lm}(\cos\theta)\cos(m\phi)\sin\theta\, d\theta\, d\phi \tag{7.2}$$

and the solid Earth contribution given by:

$$\Delta\bar{C}_{lm}^{\text{solid Earth}} = \frac{3k_l}{4\pi a\rho_{ave}(2l+1)} \int \Delta\sigma(\theta,\phi)\bar{P}_{lm}(\cos\theta)\cos(m\phi)\sin\theta\, d\theta\, d\phi \ . \tag{7.3}$$

ρ_{ave} is the average density of the Earth, a is the radius of the Earth, and k_l is the elastic load Love number of degree l. The Love numbers used in this study are adapted from Han and Wahr (1995); Wahr et al. (1998), and from a linear interpolation of these, as discussed by Wahr et al. (1998). The love numbers are shown in Fig. 7.2. $\Delta\sigma$ is the change in surface density:

$$\Delta\sigma(\theta,\phi) = \int_{\text{thin layer}} \Delta\rho(r,\theta,\phi)dr, \tag{7.4}$$

where $\Delta\rho(r,\theta,\phi)$ is the density re-distribution that caused the gravity change observed by GRACE. Eq. 7.1-7.3 are satisfied, if the layer of $\Delta\rho$ is thin, i.e. $(r/a)^{l+2} \approx 1$ with a and r being the layer boundaries.

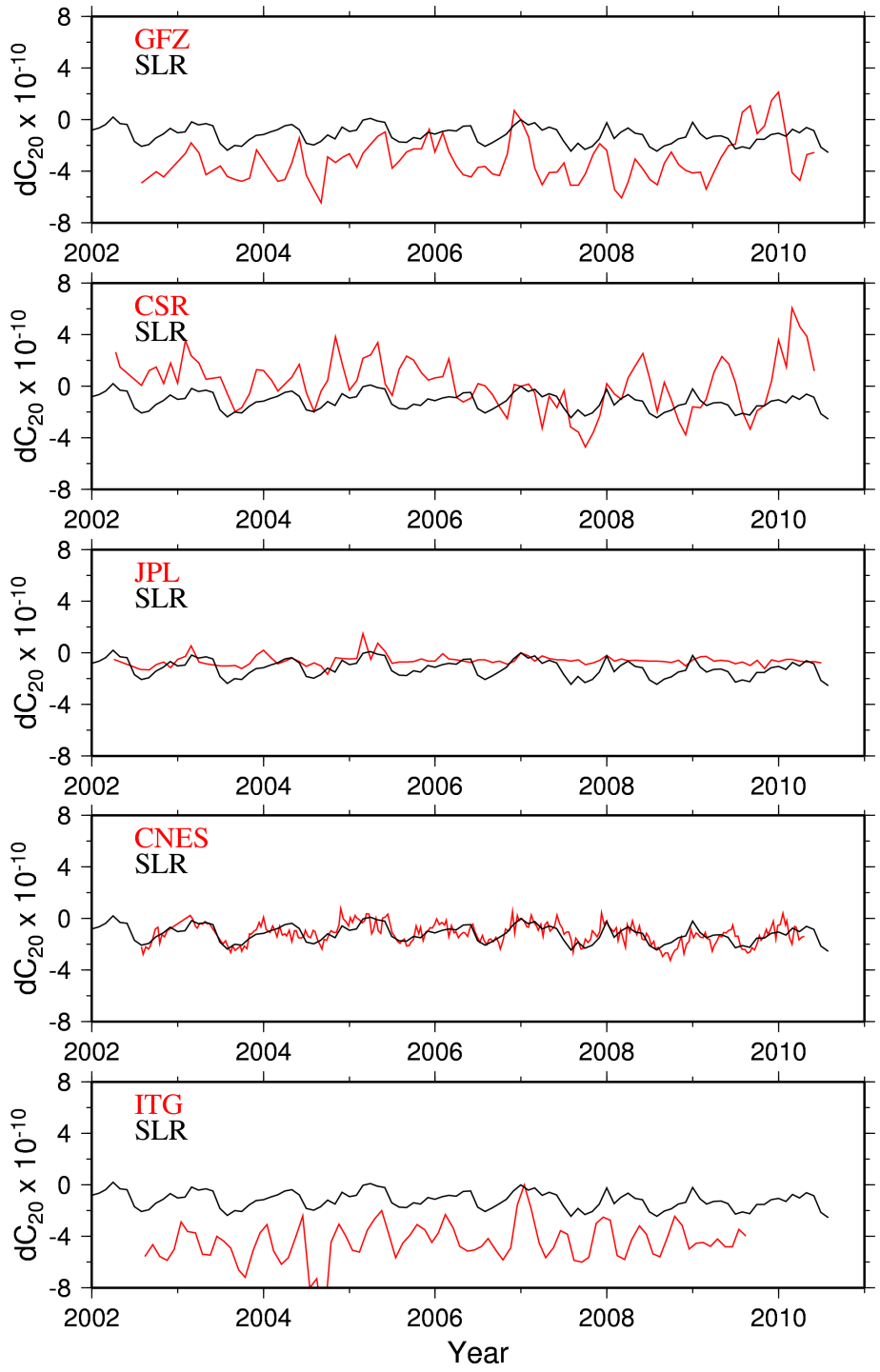

Figure 7.1: *Time variability of the $\bar{C}_{20}$ coefficients from the five processing centres are shown in red. The $\bar{C}_{20}$ coefficients derived from SLR are shown in black.*

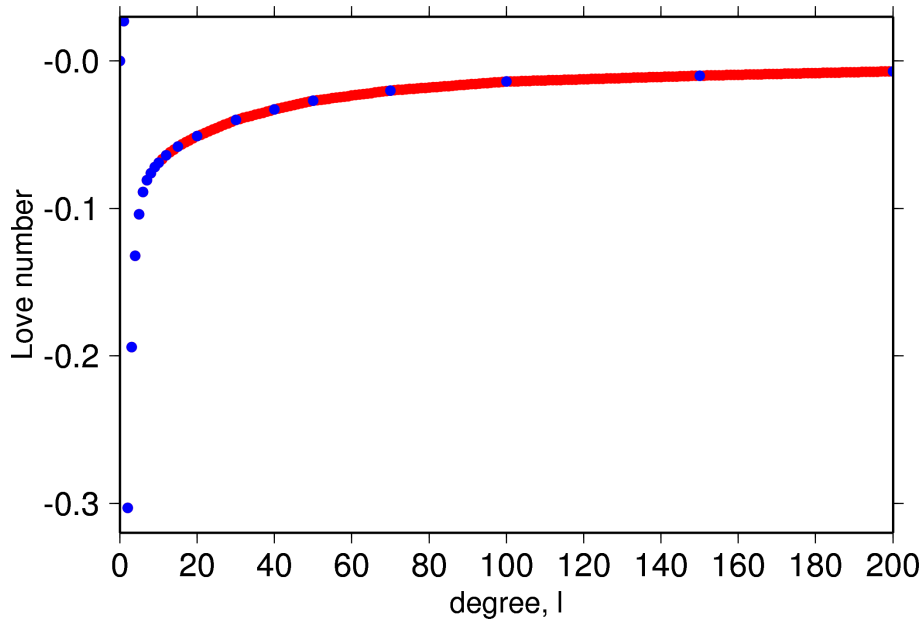

Figure 7.2: *Elastic love numbers from Wahr et al. (1998) and Han and Wahr (1995) are shown in blue. The remaining love numbers, shown in red, are found by linear interpolation of the provided (blue) love numbers.*

The change in Stokes coefficients caused by a surface (e.g. ice) mass change ($\Delta\bar{C}_{lm}^{\text{surf mass}}$), can then be related to the GRACE Stokes coefficients ($\Delta\bar{C}_{lm}$) by:

$$\Delta\bar{C}_{lm}^{\text{surf mass}} = \frac{1}{k_l + 1}\Delta\bar{C}_{lm} \quad . \tag{7.5}$$

Following the method previously described, all of the GRACE Stokes coefficients are corrected for the solid Earth response, before the inversion is applied to derive ice mass changes.
The equations 7.1-7.5 are equally valid for the $\Delta\bar{S}_{lm}$ coefficients.

7.3 De-striping

A well-known problem with the monthly GRACE solutions is apparent linear features (or stripes) in the global fields, generated from the monthly solutions. These stripes are a consequence of resolution-dependent noise, related to the satellite orbit geometry, the lack of spatial coverage, and errors in the background fields. Since the two GRACE satellites follow each other in a single orbital plane, the satellite range observable used in gravity field computation will primarily have an along-track sensitivity. Therefore, the noise will not be seen as white noise on the sphere, but as being correlated along the satellite track generally oriented in the north-south direction.

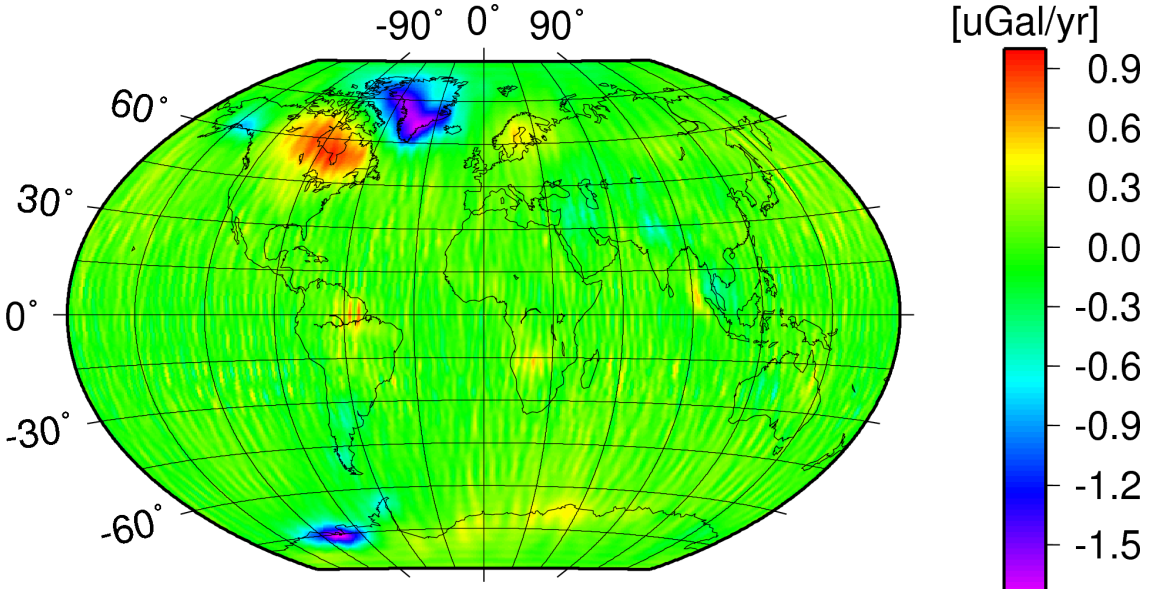

(a)

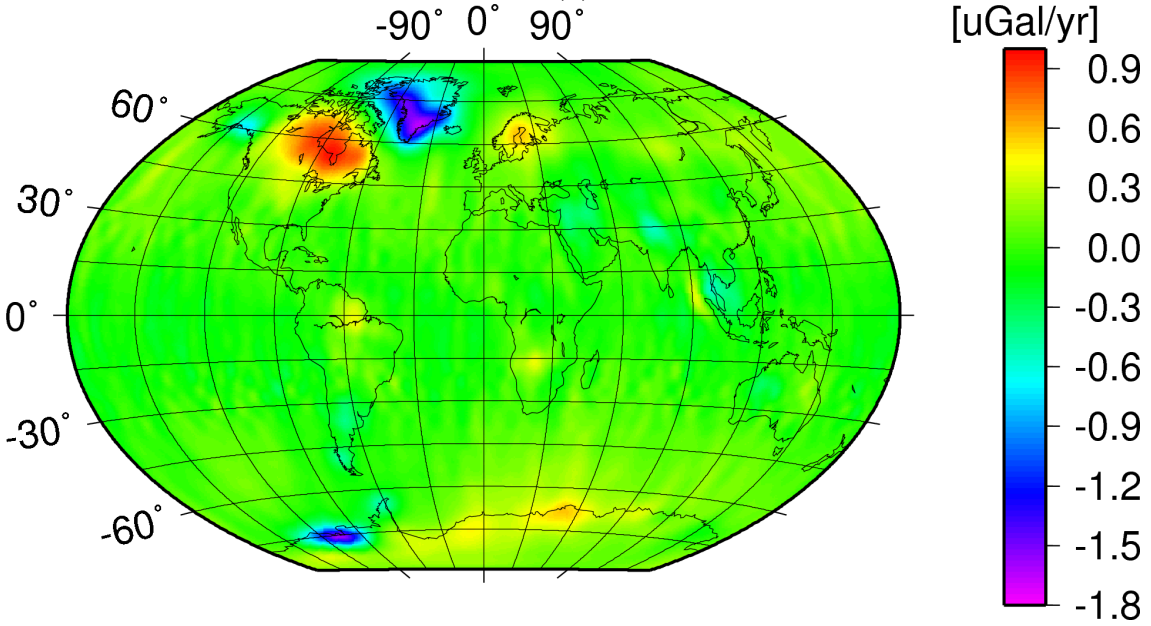

(b)

Figure 7.3: *Trend in the gravity disturbance at satellite altitude from GFZ solutions. (a) No smoothing. (b) De-striping applied to the monthly solutions with a smoothing parameter of* $a = 10^{10}$.

One way of removing the stripes is simply to truncate the spherical harmonic expansion at a relatively low degree, because the noise is associated with the short wavelength components of the solutions. A significant draw-back with this approach is that a part of the physical signal will be removed as well.

Several filtering methods have been developed in order to de-stripe the monthly fields to overcome the problem (Han et al., 2005; Swenson and Wahr, 2006; Sasgen et al., 2006; Fengler et al., 2007).
Due to the fact that the aliasing errors are strongly correlated in space but not as much in time, less de-striping (smoothing) is necessary when looking at long term trends (as is the case in this study). Figure 7.3(a) shows the trend in the gravity disturbance globally, for the entire GFZ time period, and it is seen that the stripes are as well present even when looking at long term trends. Therefore, the de-striping method presented in Kusche (2007); Kusche et al. (2009) is applied to the CSR, GFZ, JPL and ITG models, and present mass balance estimates based on these de-striped models.
The de-striping method developed by Kusche (2007) is a non-isotropic smoothing precedure, based on approximate de-correlation and successive regularization of the GRACE monthly solutions. The smoothess of the solutions is controlled by the parameter, a.

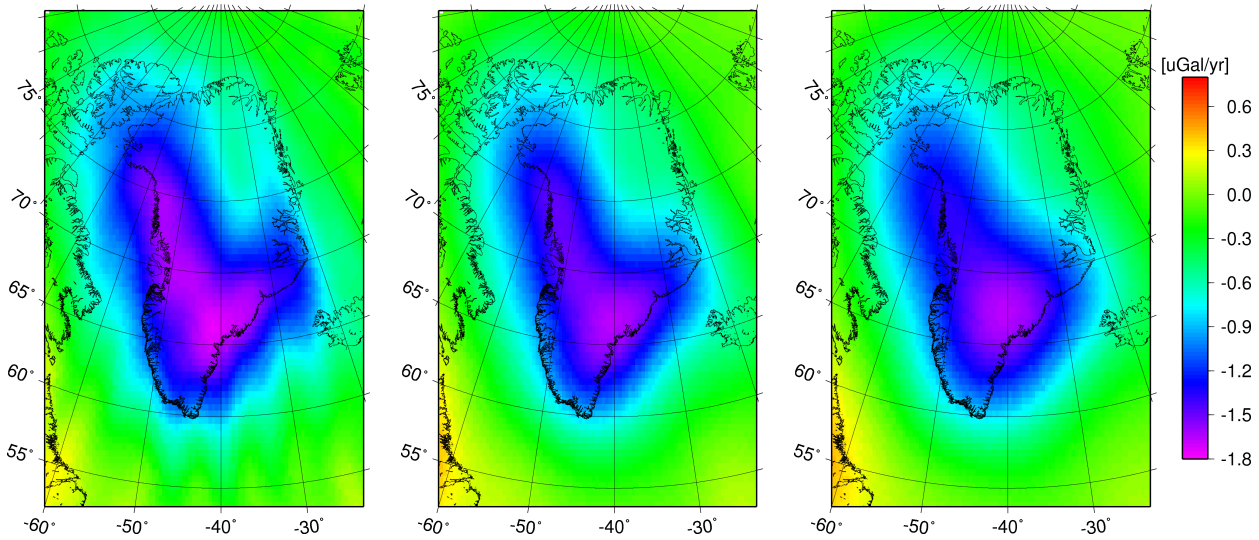

Figure 7.4: *Trend in the gravity disturbance from the full set of the GFZ solutions. (a) No de-striping. (b) De-striping applied to the monthly solutions with a smoothing parameter of $a = 10^{10}$, and (c) smoothing parameter of $a = 10^{12}$.*

Indridi Einarsson, DTU-Space (personal communication, 2010), has kindly produced the de-striped solutions for this study. A smoothing parameter of $a = 10^{10}$ is chosen, which results in a relatively weak smoothing. This smoothing parameter was chosen based on an empirical analysis, and ensures that the stripes are reduced while the gravity trend signal in Greenland is not dampened significantly. Figure 7.4 (a) shows the gravity disturbance trend at satellite altitude over Greenland, derived from the GFZ solutions, and it is seen how the trend of the un-filtered solutions contains some un-physical striping effects. The effect of the different degrees of smoothing in the de-striping in the Greenland region is seen by comparing Fig. 7.4 (a)-(c). The stripes are reduced in Fig. 7.4(b), but when applying the stronger smoothing parameter of $a = 10^{12}$ the amplitude of the trend is reduced, hence it removes some of the physical signal.
On a global scale the effect of de-striping is seen by comparing Fig. 7.3(a) and (b), in which a smoothing parameter of $a = 10^{10}$ is applied.
Due to the stabilization of the 10-day solutions from CNES, no de-striping is needed for these models.

7.4 Accuracy assessment

As described in Sect. 4.4.1, the processing centres provide error estimates of the Stokes coefficients, given as standard deviations of each coefficient. GFZ and CSR provide both formal and calibrated error estimates, while ITG and JPL only provide the formal errors and CNES only calibrated errors. The calibrated standard deviations are derived from subset and inter-month inter-comparisons, and should be considered preliminary (or best guesses) in the sense, that they will be updated when more inter-comparisons and techniques for calibration are available. The calibrated standard deviations for GFZ and CSR solutions are provided via the PO.DAAC system as separate monthly files, with the same naming conventions as the Stokes coefficient files.
The errors vary from month to month, due to both differences in the amount of data used in the processing, and the ground track coverage (Schmidt et al., 2007).
The formal errors provided by the processing centres are derived using the assumption, that all systematic influences are completely removed, hence they are probably too low (Wahr et al., 2006).
The aliasing effects from errors in the time varying background models are not part of the formal errors either. This aliasing effect is causing errors, which are observed as stripes in the gravity fields (Sect. 7.3) (Han et al., 2004; Schmidt et al., 2007).
A variance-covariance matrix is obtained together with each monthly estimate of Stokes coefficients by the least squares adjustment. In theory, the accuracy of the mass changes can be derived by error propagation from the formal variance-covariance matrix, but this full matrix is not available. In general the variance-covariance matrix does not represent the real accuracy, which is why calibration is needed (Schmidt et al., 2007).

The error degree variance is given by (Tscherning, 1985):

$$\sigma_l^e = \left(\frac{GM}{R_e}\right)^2 \sum_{m=0}^{l} (\sigma^2(\bar{C}_{lm}) + \sigma^2(\bar{S}_{lm})) \ , \tag{7.6}$$

where $\sigma^2(\bar{C}_{lm})$ and $\sigma^2(\bar{S}_{lm})$ are the error variances of the Stokes coefficients.

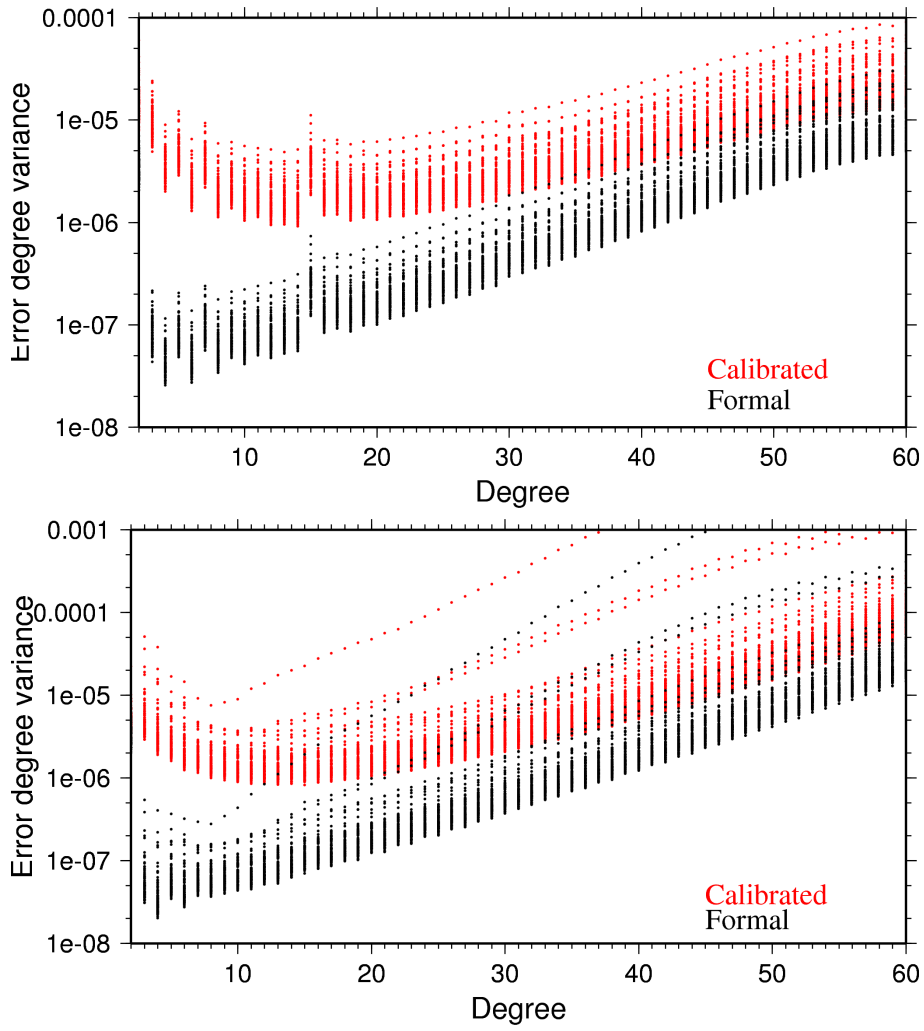

Figure 7.5: *Error degree variances derived from formal (in black) and calibrated (in red) errors. Upper figure is based on the provided CSR errors and the lower is based on GFZ errors.*

The error degree variances ($N_{max} = 60$) of both the formal and calibrated errors for GFZ and CSR are shown in Fig. 7.5, which confirm that the formal errors are indeed too low. The differences between the formal and calibrated errors in the CSR solutions are used derive degree-dependent scaling factors which are used to scale the formal errors in the JPL and ITG solutions.

The error of the mass change estimates derived from each monthly model is estimated by a Monte-Carlo like approach, in which a number of simulations are made. The simulations are created from Stokes coefficients drawn from normal distributions with zero mean, and the calibrated standard deviations provided with the GRACE level-2 data (Tscherning et al., 2001). If only the formal errors are provided (ITG and JPL), these are degree scaled by scaling factors derived from the CSR solutions.
In this approach, the error correlation is neglected, since the standard deviations provided are (the square-root of) the diagonal elements of the full variance-covariance matrix (the formal errors).
In order to derive a reliable error estimate, a sufficiently high number of simulations must be made. The estimates presented here are based on 100 simulations.

7.5 GRACE mass balance results

Based on the five level-2 GRACE data sets (Sect. 4.4.1) and post-processing of these (Sect. 7.1-7.3), time series of mass variability of the GrIS are derived by the inversion method described in Sørensen and Forsberg (2010). The ice mass changes show a short-period seasonal variability superimposed on a longer term trend, which is why the 4-parameter analysis is used. When the GIA contribution to the mass changes has been removed, the mean annual mass balance of the ice sheet is found as the secular trend in the analysis.
As an example, the time series of mass change of the GrIS, derived from the CSR solutions is shown in Fig 7.6, where the spread in the monthly mass change estimates are derived from the Monte-Carlo approach described in Sect. 7.4.
For a comparison of the different data sets, the mass change time series for all five data sets are shown in Fig. 7.7. The results are based on the de-striped solutions and does not include the error estimates. It is seen that four of the five mass change series show similar trends, but that the JPL solutions show a very low trend compared to the others. The small trend in the JPL solutions in the Arctic, has been observed by others (e.g. Baur et al. (2009); Sasgen (2009)).
The mass balance estimates based on the different data sets, using different GIA corrections used, are listed in Table 7.1. The results in this table are based on the full time periods of the different level-2 data Fig. 4.2.

The ITG time span is the shortest (August 2002 - August 2009), and in order to compare the results, an analysis is made of data from only the ITG time span. These results are also shown in Table 7.1.

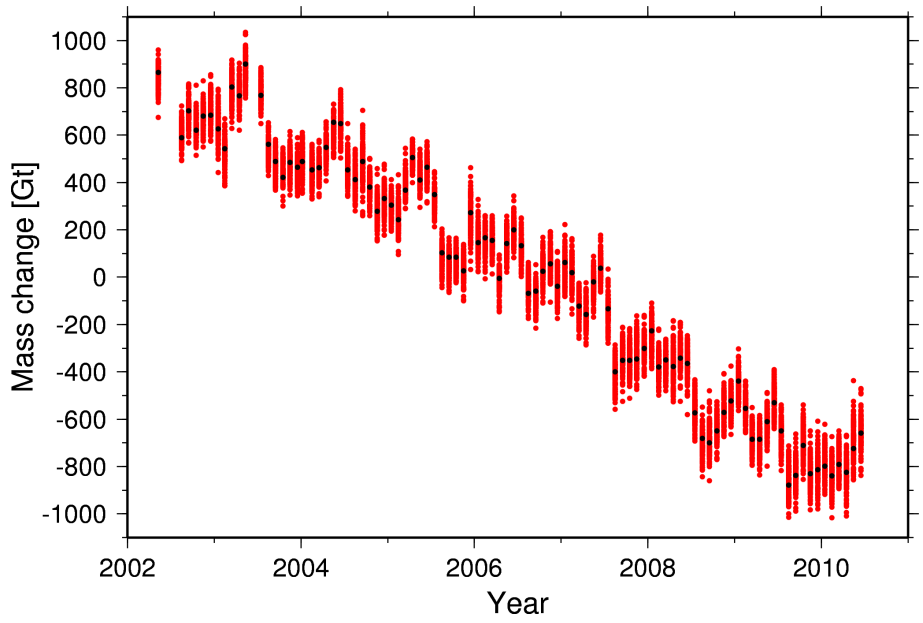

Figure 7.6: *Mass change time series of the GrIS from CSR solutions. The results of the 100 simulations derived are shown in red, and the results from the provided coefficients without taking errors into account are shown in black.*

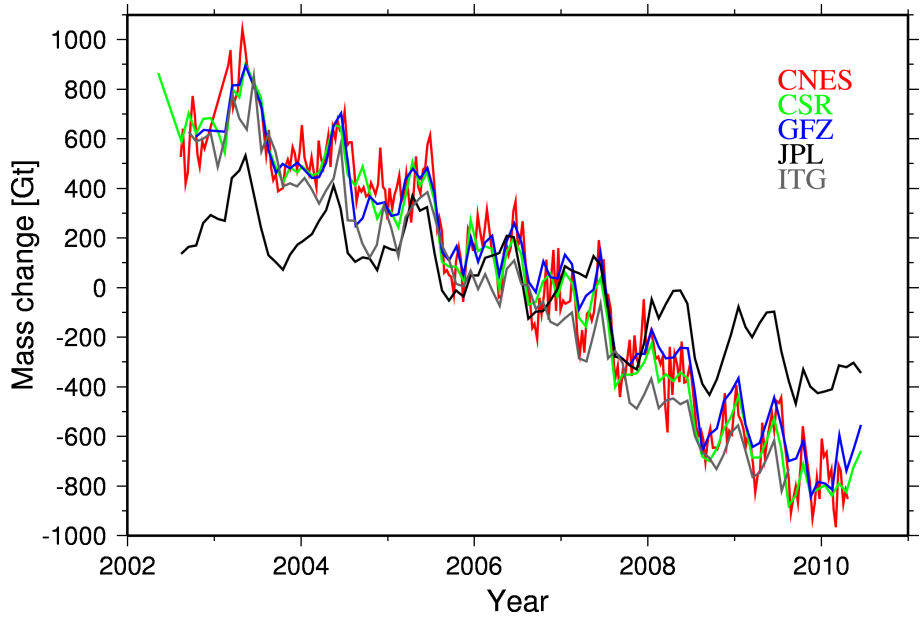

Figure 7.7: *Mass change time series of the GrIS from CSR, GFZ, JPL, CNES and ITG.*

Table 7.1: *Mass balance estimates from GRACE data. The results are obtained using different data sets and GIA corrections. Results are given for the full time span of each data set as well as for the ITG time span (August 2002 - August 2009).*

L2 Data	**GIA**	**Mass balance [Gt/yr] Full time span**	**Mass balance [Gt/yr] ITG time span**
CSR	ICE-5G (VM2)	-222 ± 28	-225 ± 33
CSR	ICE-3G (TP)	-235 ± 28	-238 ± 33
CSR	ANU05 (KL)	-229 ± 28	-232 ± 33
GFZ	ICE-5G (VM2)	-213 ± 28	-209 ± 32
GFZ	ICE-3G (TP)	-226 ± 28	-222 ± 32
GFZ	ANU05 (KL)	-220 ± 28	-216 ± 32
JPL	ICE-5G (VM2)	-100 ± 21	-96 ± 22
JPL	ICE-3G (TP)	-113 ± 21	-108 ± 22
JPL	ANU05 (KL)	-107 ± 21	-103 ± 22
ITG	ICE-5G (VM2)	-225 ± 36	-225 ± 36
ITG	ICE-3G (TP)	-238 ± 36	-238 ± 36
ITG	ANU05 (KL)	-232 ± 36	-232 ± 36
CNES	ICE-5G (VM2)	-226 ± 34	-229 ± 36
CNES	ICE-3G (TP)	-239 ± 34	-242 ± 36
CNES	ANU05 (KL)	-233 ± 34	-236 ± 36

The largest annual mass loss found from the limited time span is $242 \pm 39\,\mathrm{Gt\,yr^{-1}}$, and is determined from the CNES solutions with the ICE-3G(TP) GIA correction. It is seen that the MB estimates from CNES, ITG, GFZ and CSR agree within the errors, however the JPL results are very low with estimates between $-96 \pm 22\,\mathrm{Gt\,yr^{-1}}$ and $-108 \pm 22\,\mathrm{Gt\,yr^{-1}}$. Furthermore, it is seen from Table 7.1 that the different GIA corrections result in MB estimates which differ with up to $13\,\mathrm{Gt\,yr^{-1}}$.

The spatial distribution of the mass changes (mm water equivalent per year) for all five level-2 data sets, found by the inversion based on the ITG time span are shown in Fig. 7.8.

It is seen that very similar pattern are derived from CSR, GFZ, ITG and CNES data which reveals large coastal mass losses, with largest values found along the south-east and north-west coasts. A small mass increase is observed in the central, northern part of the ice sheet.
A somewhat different picture is revealed by the JPL solutions, which shows a larger central mass increase than the other results, and which also predicts a mass increase in south-west Greenland.

7.6 Changes in time

The mass change results presented in the previous sections are derived, assuming linear trends in gravity in time. Velicogna (2009) found increasing rates of ice mass loss of the GrIS, based on GRACE data, and (Khan et al., 2010b) found that GRACE and GPS measurements reveal that the pattern of the GrIS mass loss is changing in time. Mass change estimates of the GrIS derived from three year intervals, are listed in Table 7.2. These estimates indicate that the rate of GrIS mass loss was indeed increasing from 2002 to 2008, but also that it decreased in the period 2007-2010. It should be noted, that the MB estimates listed in Table 7.2 are associated with large uncertainties, due to the short time span of data.

Table 7.2: *Mass balance estimates from three year intervals of GRACE CSR data.*

Time period (both years included)	**Mass balance [Gt/yr]**
2002-2004	-146 ± 68
2003-2005	-176 ± 65
2004-2006	-190 ± 67
2005-2007	-211 ± 74
2006-2008	-268 ± 70
2007-2009	-254 ± 71
2008-2010	-196 ± 86

Figure 7.9 shows the trend in gravity (in 480 km altitude) over Greenland, derived from CSR GRACE data from three year intervals of data. It is seen that the pattern is indeed changing in time. The negative gravity trend (associated with mass loss) is seen to migrate from Southeast Greenland in 2003-2005, up along the west coast during 2004-2008. The maximum negative trend is in 2007-2010 found over the Northeast coast.

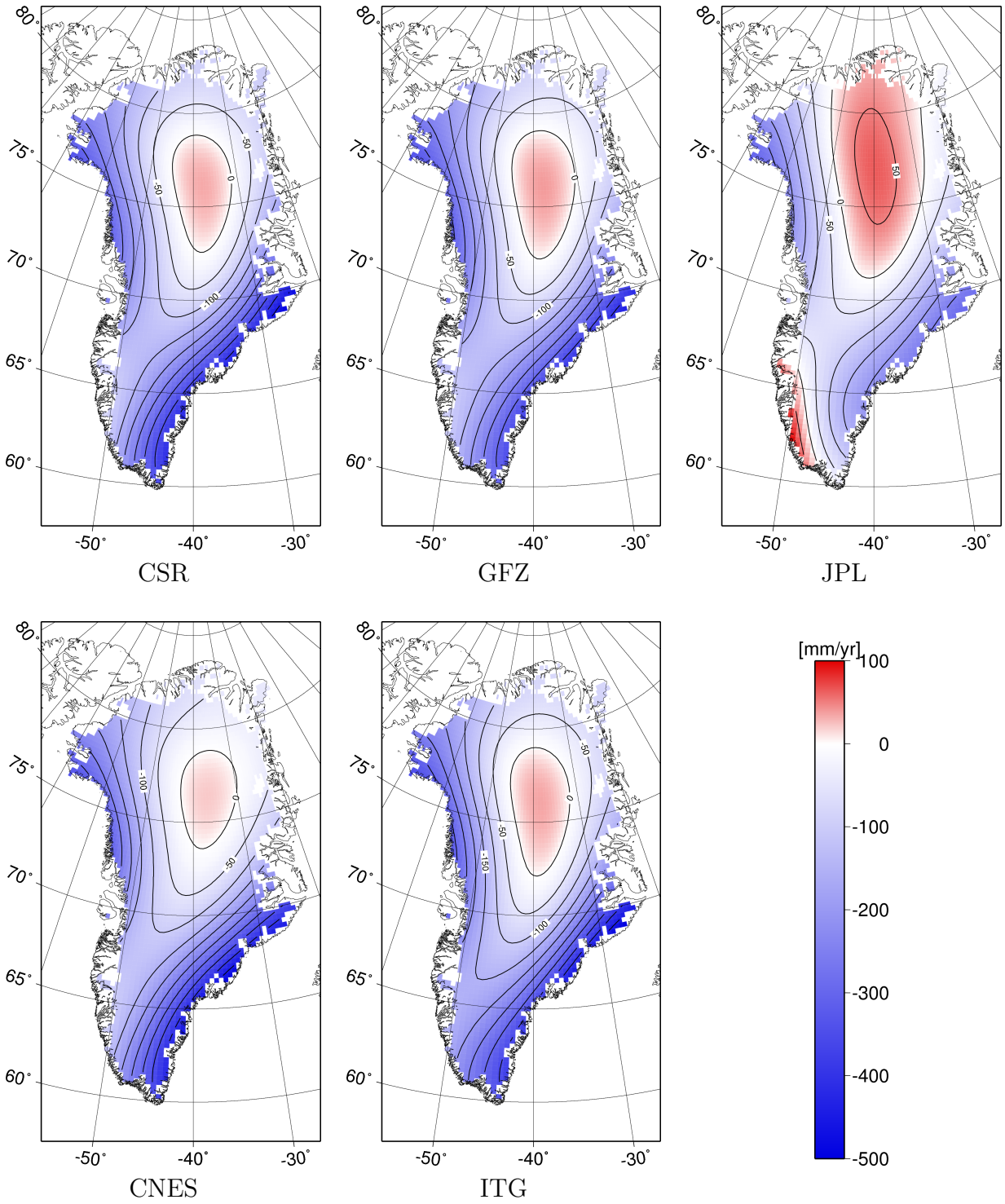

Figure 7.8: *Spatial pattern of mass changes, based on data from August 2002 to August 2009 from the five processing centres.*

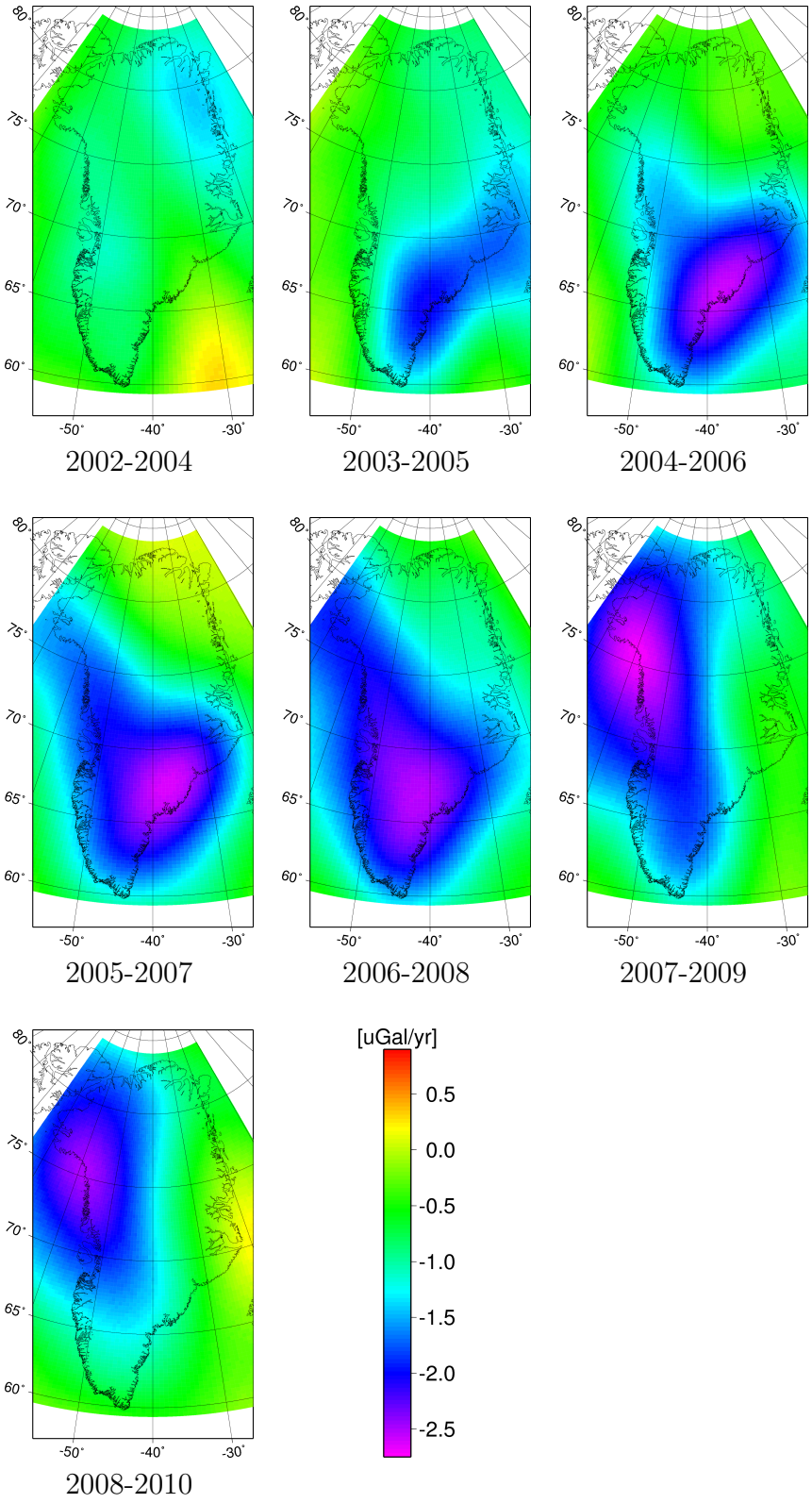

Figure 7.9: *Change in gravity trend in time over Greenland (altitude 480 km), based on intervals of three years of CSR GRACE data.*

Chapter 8

GrIS mass balance from ICESat

For this thesis, four methods (M1-M4) for deriving rates of elevation change $\left(\frac{\mathrm{d}H}{\mathrm{d}t}\right)$ from the ICESat altimetry data were developed. Based on elevation change corrections, interpolation and density modelling, the mass balance of the GrIS is derived. The methods and results are described in Sørensen et al. (2010a). This chapter elaborates on results, details, and descriptions not presented in Sørensen et al. (2010a).

8.1 Elevation changes of the GrIS

In Sørensen et al. (2010a), it is concluded that M3 is the preferred method, for deriving surface elevation changes $\left(\frac{\mathrm{d}H}{\mathrm{d}t}\right)$, and therefore the results described in this section are primarily based on this method.
M3 is a method to derive $\left(\frac{\mathrm{d}H}{\mathrm{d}t}\right)$ along-track in segments of 500 m. In M3, it is assumed that the surface elevation (H^{M3}), varies linearly with position (x, y), time (t), and a seasonal signal $s(t) = D\cos\left(\frac{2\pi}{T}t + \phi\right) = \alpha\cos(\omega t) + \beta\sin(\omega t)$, with $D = \sqrt{\alpha^2 + \beta^2}$ being the amplitude, T (365 days) the period, ϕ the phase.
A least squares linear regression is applied to solve for $\left(\frac{\mathrm{d}H}{\mathrm{d}t}\right)$, the along-track $\left(\frac{\mathrm{d}H}{\mathrm{d}x}\right)$ and cross-track slope $\left(\frac{\mathrm{d}H}{\mathrm{d}y}\right)$, the seasonal terms, and the reference surface elevation simultaneously:

$$H_{ij}^{M3} = \begin{pmatrix} A_{ij} \\ B_{ij} \\ \alpha_{ij} \\ \beta_{ij} \\ \left(\frac{\mathrm{d}H}{\mathrm{d}x}\right)_{ij} \\ \left(\frac{\mathrm{d}H}{\mathrm{d}y}\right)_{ij} \end{pmatrix} (\bar{t}, 1, \cos\omega t, \sin\omega t, (x - x_0), (y - y_0)) \,, \tag{8.1}$$

where $A_{ij} = \left(\frac{\mathrm{d}H}{\mathrm{d}t}\right)_{ij}$ in segment j of track j. B_{ij} is an estimate of the topography underlying the elevation changes, and (x_0, y_0) is the centroid point of the area spanned by all of the measurements in the track segment.

The elevation changes for the entire GrIS are seen in Fig. 8.1. The elevation change pattern shows wide spread coastal thinning and thickening in the central part of the ice sheet.

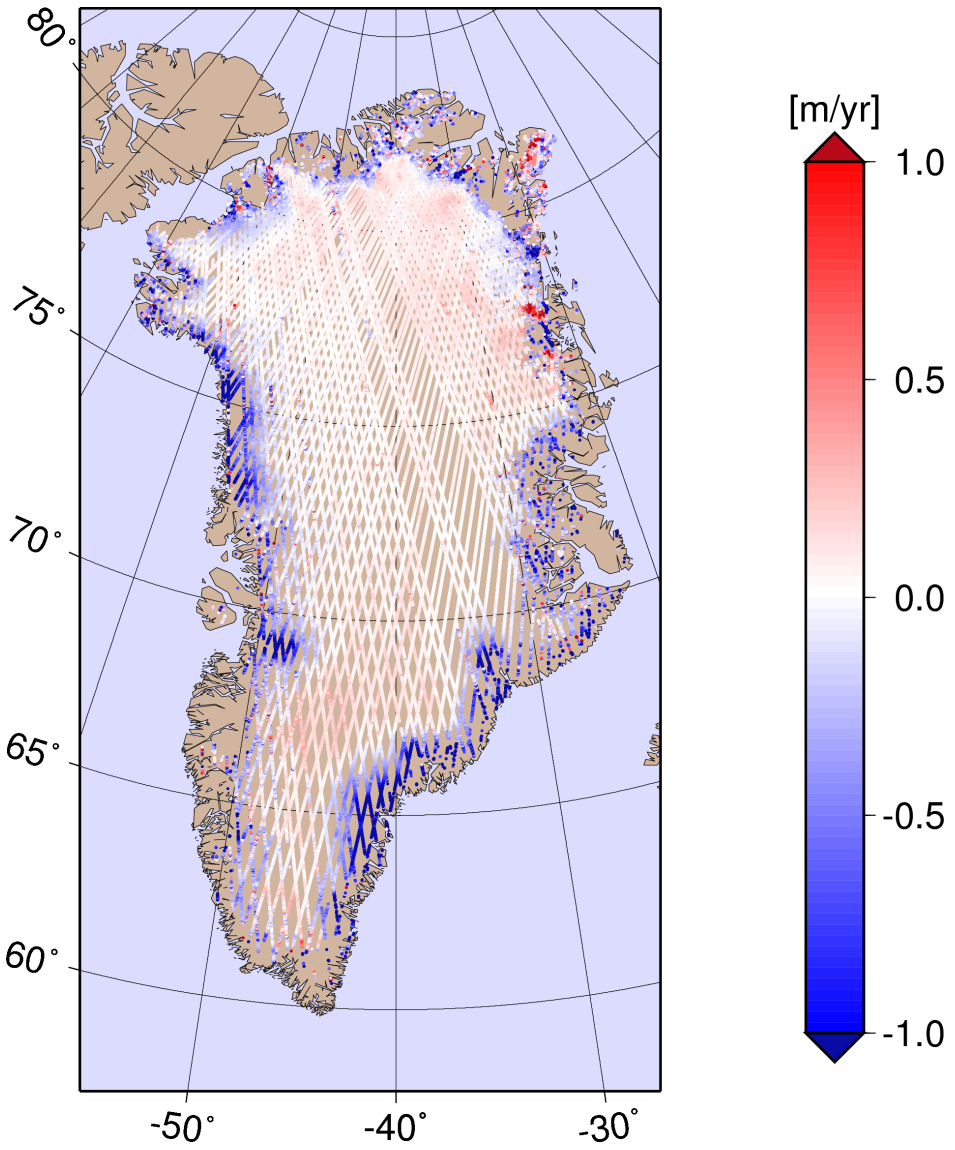

Figure 8.1: *Elevation changes of the GrIS from ICESat data, derived from method M3 (Sørensen et al., 2010a)*

Some regions show large change in elevation, such as Storstrømmen, Jakobshavn Isbræ, Flade Isblink and the Helheim glacier. These four regions are shown in Fig. 8.2(a)-(d), using color scales optimized for revealing the pattern and size of the local changes.

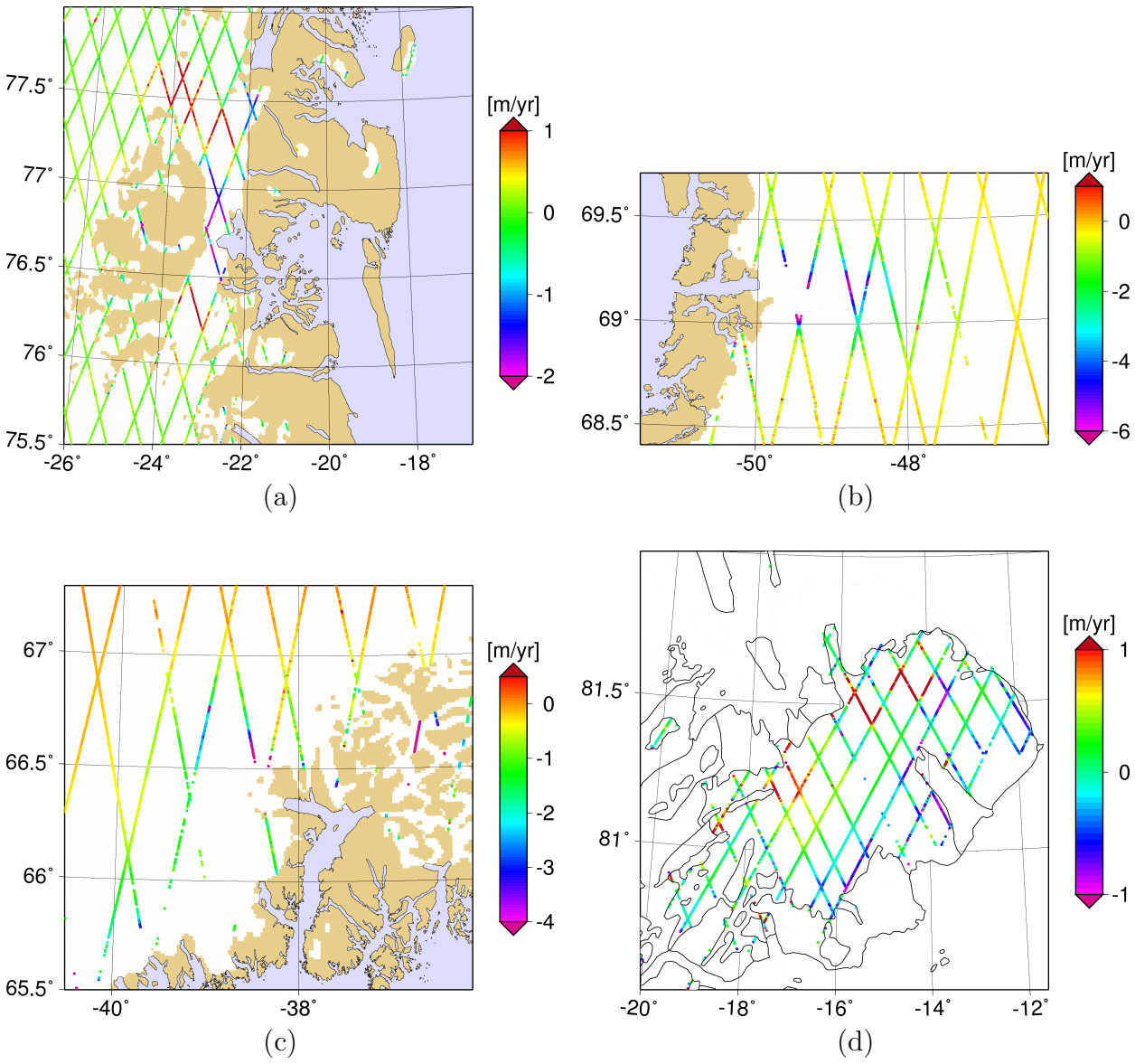

Figure 8.2: *Regional elevation changes of from ICESat data, derived from method M3 (a) Storstrømmen, (b) Jakobshavn Isbræ, (c) Helheim, and (d) Flade Isblink.*

Storstrømmen in north-east Greenland shows thinning of more than 2 $\mathrm{m\,yr^{-1}}$ near the terminus, and a thickening of more than 1 $\mathrm{m\,yr^{-1}}$ in higher regions of the glacier (Fig. 8.2(a)). This thickening of the higher part of the glacier could suggest a recovery from an earlier surge.
The thinning of Jakobshavn Isbræ in West Greenland has been the focus of much research (e.g. Krabill et al. (2004); Holland et al. (2008); Khan et al. (2010a)). Fig. 8.2(b) shows a rate of thinning of more than 6 $\mathrm{m\,yr^{-1}}$ (Fig. 8.2(b)). A theory is that the speed-up of Jakobshavn Isbræ is caused by warm water in the fjord, in which the glacier is terminating (e.g. Holland et al. (2008)).
Near the Helheim glacier in south-east Greenland, an elevation decrease of more than 4 $\mathrm{m\,yr^{-1}}$ is observed (Fig. 8.2(c)), and the thinning is observed in the whole coastal region in that area. This coastal thinning and associated mass loss is also seen as uplift, when monitored by GPS (Khan et al., 2007).
Far north, at the ice cap Flade Isblink, a complex pattern of elevation change is observed. The north-western part of the ice cap has thickened with maximum values of more than 1 $\mathrm{m\,yr^{-1}}$, while the south-eastern part shows a thinning of up to 0.5 $\mathrm{m\,yr^{-1}}$ (Fig. 8.2(d)). Both land-terminating and marine-terminating glaciers are draining the ice cap (Palmer, 2010), and the pattern of elevation change could be caused by changes in accumulation pattern of the Arctic sea ice cover.

Two comparisons of the rate of elevation change, derived from ICESat data and airborne LiDAR data respevtively, are shown in App. E. Results from the Upernavik and Jakobshavn area are shown, and good agreement between the two data sets is found.

8.1.1 Seasonal variations

As described in Sørensen et al. (2010a), the elevations in a given along-track segment are fitted to a function which include a seasonal signal (Eq. 2 in ibid). The amplitude of the seasonal elevation variation is a function of changes in the accumulation, flow and melt during the year. The amplitude estimated by M3 is shown in Fig. 8.3(a). For comparison, a map of accumulation from the PARCA project (Bales et al., 2009) is shown in Fig. 8.3(b). It is seen that the amplitude of the season signal - as would be expected - is largest in the coastal regions, while it is small in the interior part of the ice sheet. The pattern of the amplitude agrees with the accumulation map, which show the largest accumulation along the south-east and west coasts, and the least accumulation in the northern and central part of the ice sheet.

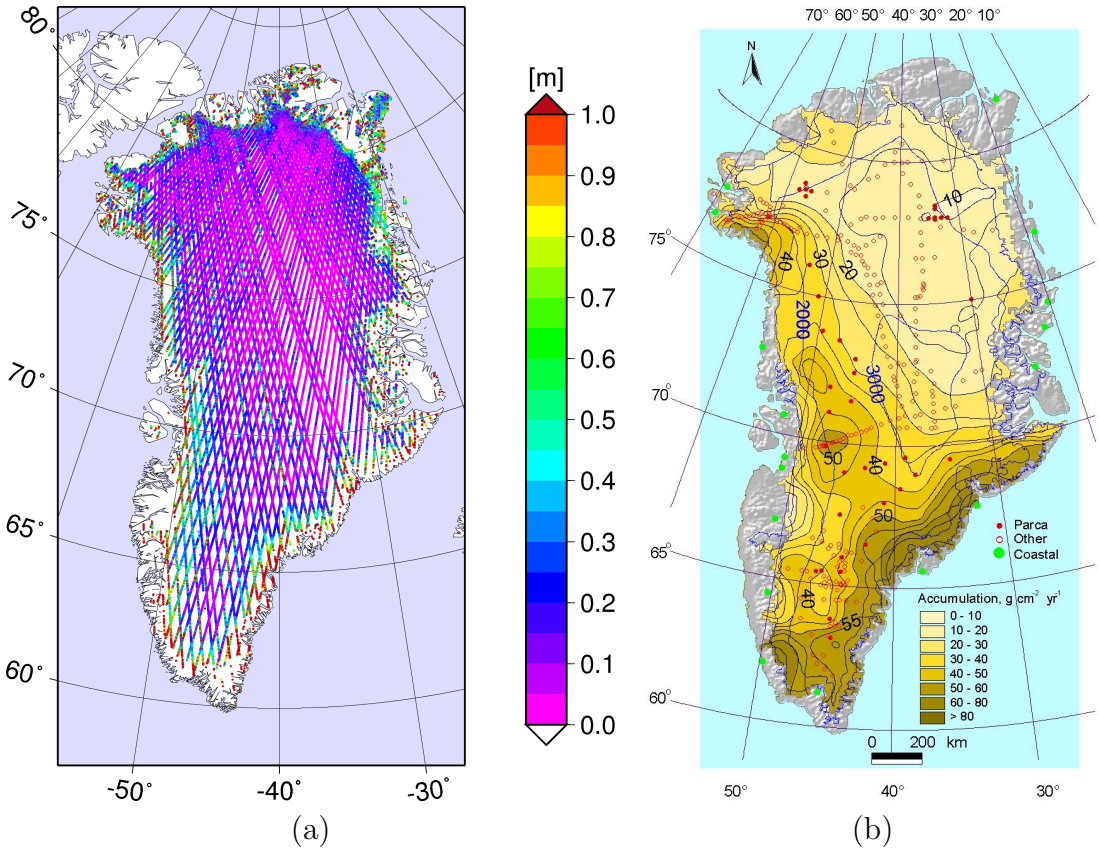

Figure 8.3: *(a) Amplitude of the seasonal elevation change variations, using M3 and (b) map of accumulation from the PARCA project Bales et al. (2009).*

8.1.2 Volume change

The total volume change estimates were found by interpolation of the $\left(\frac{\mathrm{d}H}{\mathrm{d}t}\right)$ estimates, using ordinary Kriging in a bootstrap approach, to estimates the error on the volume change, as described in Sørensen et al. (2010a). This work was carried out in collaboration with Karina Nielsen, DTU-Space.
The variances of the $\left(\frac{\mathrm{d}H}{\mathrm{d}t}\right)$ estimates are derived from the least squares linear regression, and are used as weights in the interpolation. The variances of $\left(\frac{\mathrm{d}H}{\mathrm{d}t}\right)$ from M3 are shown i Fig. 8.4. The largest variances are, as expected, found in the coastal regions of the ice sheet, due to the fact that the error on the individual measurements is increasing with surface slope (Brenner et al., 2007). Also the assumption in M3, that the topography is linear in each segment, is probably only valid in the flat central part of the ice sheet, whereas the coastal regions are characterized by highly varying topography. Furthermore, M3 assumes a linear elevation change with time, and it is likely, that the behaviour of some of the outlet glaciers is not linear in time, but that the thinning is variable. It is assumed, that the data culling (Sect 5.5) ensures, that the accuracy of the individual measurements

are the same in each 500 m segment.

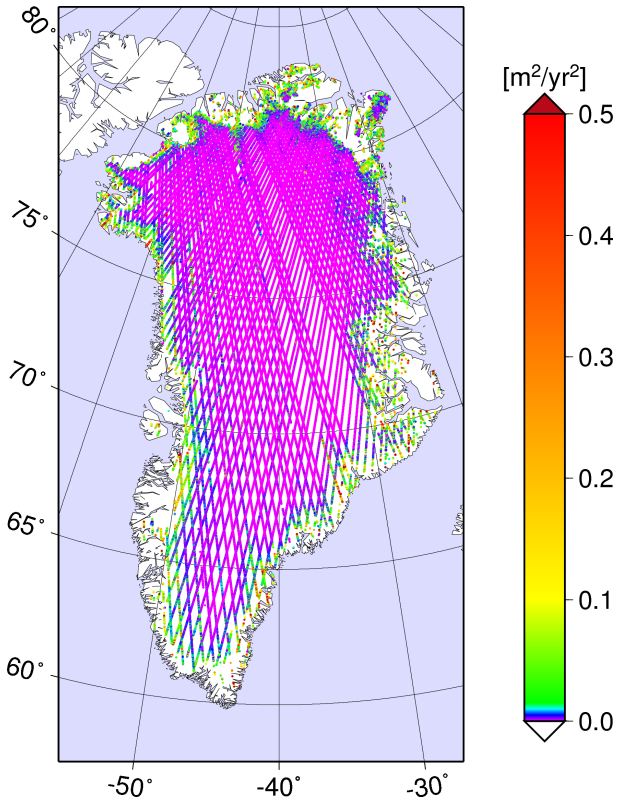

Figure 8.4: *Variance of* $\left(\frac{\mathrm{d}H}{\mathrm{d}t}\right)$ *from using M3. The variances are used as weights in the interpolation, which is used in the total volume change estimate.*

8.2 Elevation change corrections

Not all of the elevation changes observed by ICESat will contribute to the mass balance of the ice sheet, such as the bedrock movement, firn compaction and possible ICESat inter-campaign elevation biases. Therefore, it is necessary to apply corrections for the elevation change before the modeled snow/ice densities are applied, and the volume change is converted into a mass change. The largest elevation change correction that must be applied is the firn compaction correction. Besides this, the vertical movement of the bedrock, both the elastic response to present-day mass changes and GIA are determined and corrected for, along with the ICESat inter-campaign elevation biases (Sørensen et al., 2010a).

8.2.1 Firn compaction correction

The firn is the layer of snow from previous seasons, which is not yet glacial ice (see Fig. 8.5). The firn column responds to changes in the climate. A rise in temperature will cause the firn to compact, and this will be observed as an elevation decrease by ICESat. Since the firn compaction elevation change is not associated with a mass change, it must be corrected for, before determining the mass balance from the ICESat derived elevation changes. In this study, the HIRHAM5 regional climate model (RCM) provides the climate variables to which the firn layer profile responds (Christensen et al., 2006). The firn compaction model used in this study was developed by Sebastian B. Simonsen, Centre for Ice and Climate, NBI.

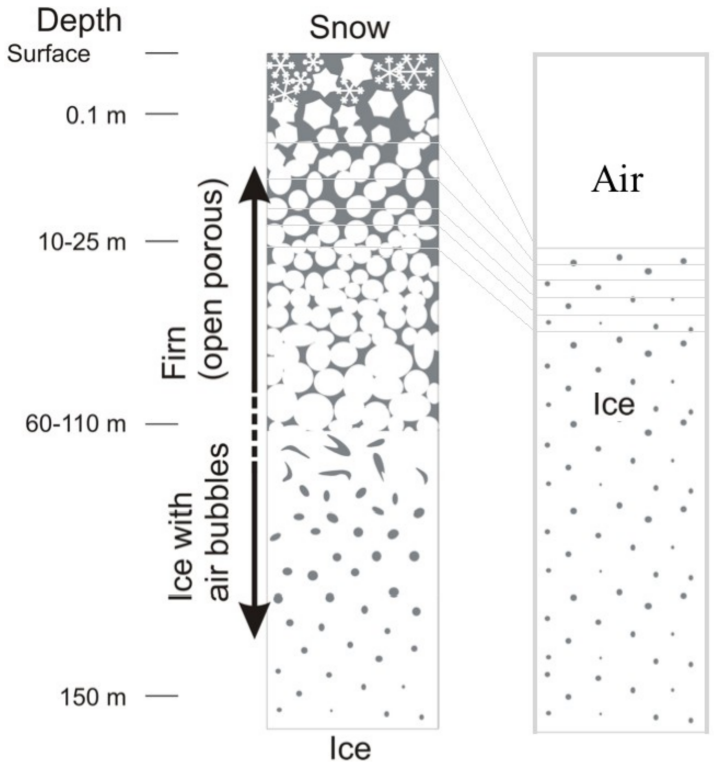

Figure 8.5: *Figure illustrating the concept of firn compaction. The firn column responds dynamically to changes in the climate. Illustration adapted from Rasmussen and Elbrønd Hansen (2008), and modified by S. Simonsen.*

8.2.2 Vertical bedrock movement

As described in Sect. 6, the Earth responds instantaneously to the present-day mass changes of the ice sheets. This elastic movement will be observed by ICESat, and must be subtracted from the elevation changes, since this bedrock movement does not contribute to the mass balance of the ice sheet.
An estimate of the elastic contribution is determined by defining the spatial distribution of the mass change estimates as a loading event, and then calculate the Earth's elastic response, by use of SELEN (Sect. 6.4). Off course this will only lead to an estimate of the magnitude of the elastic signal, since mass changes have not been corrected for the elastic contribution, before calculating this.

An iterative procedure was applied:
1. Elevation changes from ICESat are converted into mass changes.
2. Mass changes used to determine elastic uplift.
3. The uplift is used subtracted from the elevation changes in 1.
4. The corrected elevation changes are converted into mass changes.
5. The corrected mass changes are used to determine a new uplift.
6. repeat 3. - 4. to obtain new mass balance

This iterative approach showed, that the mass loss determined in step 1. and 4. differ with approximately 4 $\mathrm{Gt\,yr^{-1}}$ for M3, and shows that the elastic rebound is indeed an important correction. The difference between the mass balance determined from 6. and 4. was found to be negligible, hence the steps 1. - 4. are sufficient for correction of the elastic uplift.
The elastic uplift determined from M3 is shown in Fig. 8.6. It is seen, that maximum value of the elastic uplift, due to the present-day unloading is approximately 1 $\mathrm{cm\,yr^{-1}}$, which is at the same order of magnitude as the GIA signal, Sect. 6. By correcting for the elastic uplift, the mass loss estimates are increased, since some of the thinning of the ice sheet is compensated by the Earth rebounding. As expected, the pattern of the uplift is strongly correlated with the pattern and magnitude of the mass changes (Fig. 8.6 and 8.8(a)).
In Sørensen et al. (2010a) the MB estimates are derived, using the ICE5G GIA model in the elevation change correction. Using the three different GIA models shown in Fig. 6.4, MB estimates from M3 are found to vary between -209 and -214 $\mathrm{Gt\,yr^{-1}}$.

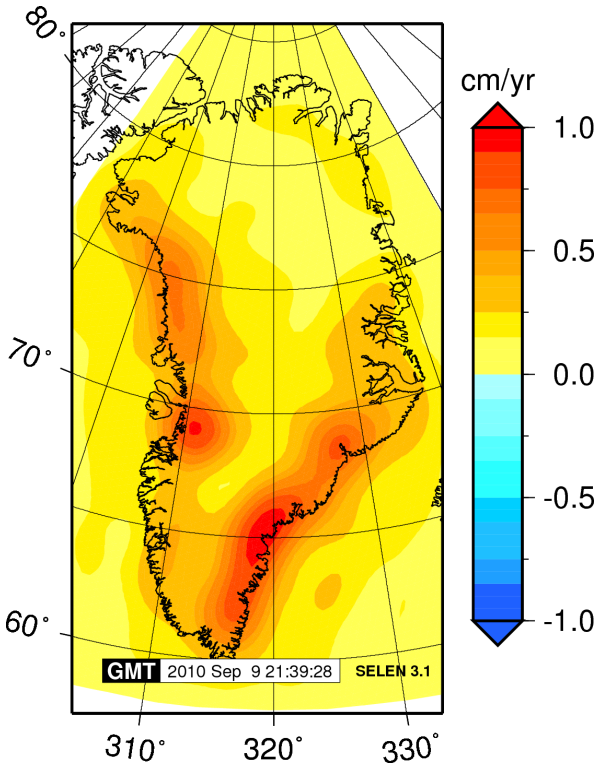

Figure 8.6: *The elastic response of the Earth due to the present-day mass changes of the GrIS determined from ICESat data using M3.*

8.2.3 ICESat inter-campaign elevation bias

The three lasers on-board ICESat, were used one at the time. It is important to take possible elevation biases between the campaigns into account, since such biases will be observed as elevation changes.
Following the method described in Gunter et al. (2009), for determining the inter-campaign elevation biases, ICESat measurements from the ocean were compared with a mean sea surface topography model. Here, the DNSC08 model was used as a reference (Andersen and Knudsen, 2009), and the comparison was limited to $\pm 66^o$ latitude. The weighted means of the differences in each ICESat laser campaign reveal an elevation bias. This analysis was done in collaboration with T. Bondo and O. B. Andersen, DTU-Space, and the result is shown in Fig. 8.7. The fitted trend is 1.59 ± 0.4 cm yr^{-1} and from this, an assumed global rate of sea level rise of 0.3 cm yr^{-1} (Leuliette et al., 2004) is subtracted.

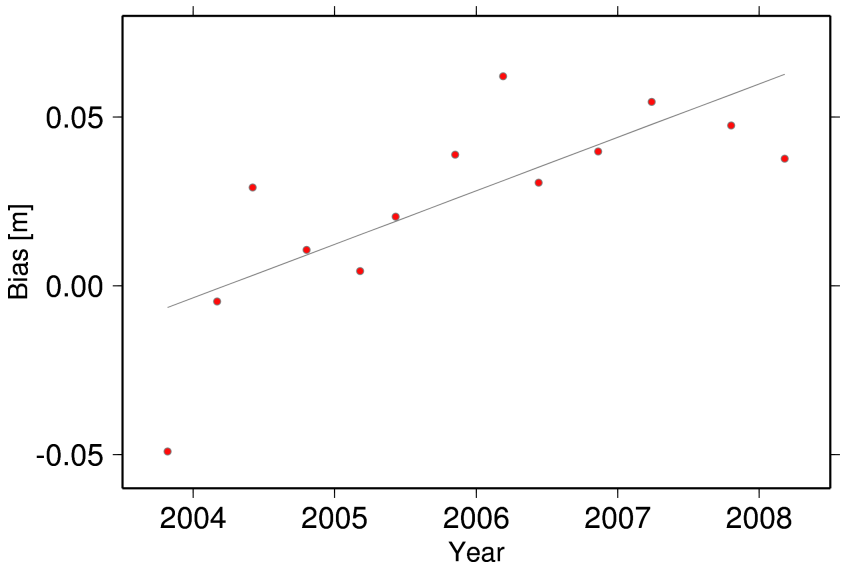

Figure 8.7: *ICESat inter-campaign elevation bias (red dots), and the fitted trend of 1.59 cm yr^{-1} (solid line).*

8.3 Mass change estimates

The mean mass balance estimates of the GrIS based on ICESat data from 2003-2008, and methods M1-M4 are presented in Sørensen et al. (2010a). Based on the prefered method, M3, we find the mass balance of the GrIS to be -210±21 Gt yr^{-1}. The mass changes given at a 5×5 km grid is shown in Fig. 8.8(a).

The elevation changes derived from ICESat are interpolated and corrected for elevation changes, which are not related to ice mass changes (Sect. 8.2). This is done in order to estimate the annual volume change of the ice sheet.

To convert the volume change into a mass change, information on the snow/ice densities is required. The density model used, was developed by Sebastian B. Simonsen, Centre for Ice and Climate, NBI, and is described in Sørensen et al. (2010a).

The average surface densities for the period 1989-2008 are shown in Fig. 8.8(b). These densities are applied to positive elevation changes, while negative elevation changes are assumed to be associated with an ice density of 900 kg m^{-3}. This ice density of 900 kg m^{-3} was chosen over the pure ice density of 917 kg m^{-3}, beacuse it is not likely that all of the thinning of the Greenland is associated with pure ice.

The basal melting of the ice sheet, caused by the geothermal heat flux, is not taken into account in this study. Neglecting this term, will lead to an error *only* where an elevation increase above the equilibrium line altitude (ELA) is found, since here a mass change is converted into mass change by using surface densities.

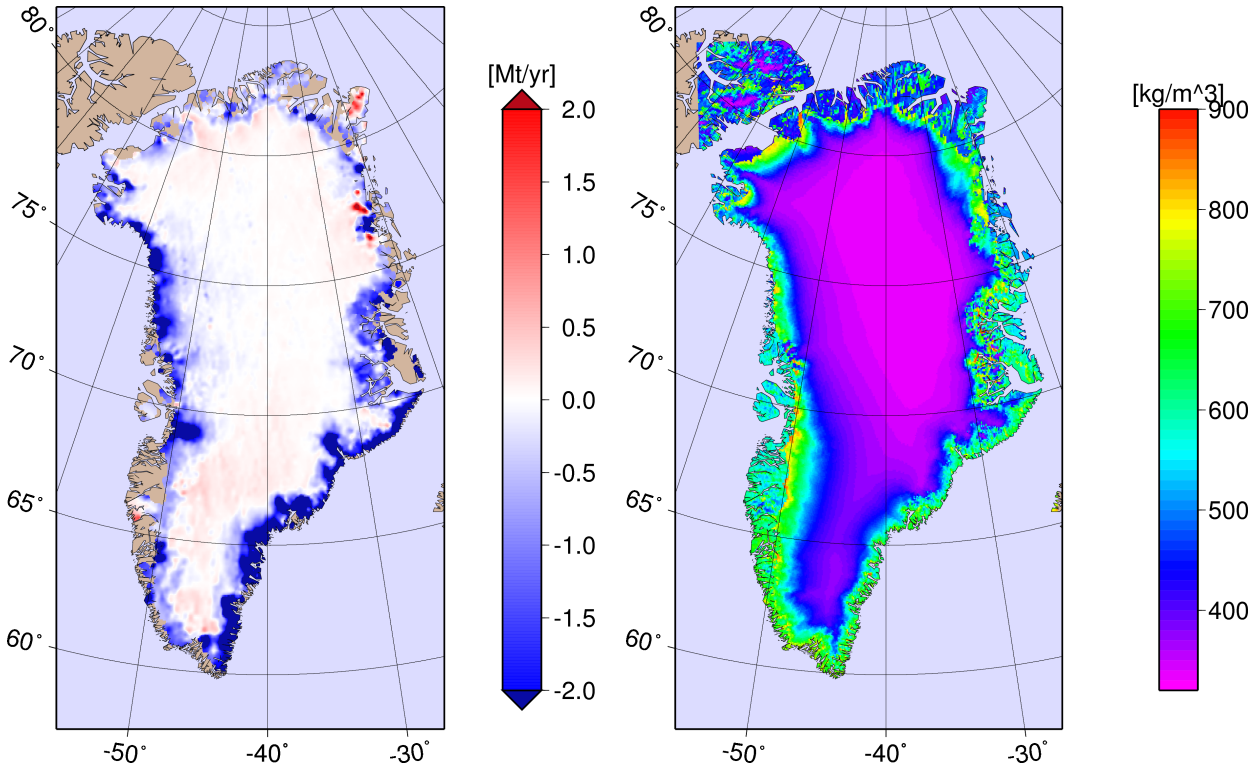

(a) (b)

Figure 8.8: *(a) The mass changes from M3 on a 5×5 km grid. From Sørensen et al. (2010a). (b) The average modelled surface densities for the period 1989-2008.*

Chapter 9

Comparison between GRACE and ICESat results

Mass balance estimates of the GrIS from GRACE data are presented in Sect. 7.5. These are based on different level-2 data in the time span 2002-2010, and three different GIA corrections are applied. In Sect 8.3, a mass balance estimate derived from ICESat data from 2003-2008 is presented. It is found that the MB estimates from GRACE and ICESat are in agreement within the uncertainties (when excluding the JPL GRACE solutions).

In this chapter, a more direct comparison of mass change results from GRACE and ICESat data is carried out, based on data sets overlapping in time. The comparison analysis includes a drainage basin scale study of the mass changes.

9.1 Overlapping GRACE and ICESat data.

The time coverage of the ICESat campaigns used in this study, are listed in Table 9.1. The data must be overlapping in time, for a direct comparison between mass changes calculations based on GRACE and ICESat data respectively.
Therefore, the 10-day CNES GRACE solutions which are overlapping the ICESat laser campaigns in time, are used to derive a GRACE mass balance estimate which can be compared to the one from ICESat data. In Sect. 7.5 it was concluded, that the CNES solutions agree well with those from CSR, GFZ and ITG. Because they are 10-day solutions, they are better suited for creating overlapping data sets, than the 1-month solutions from the other processing centres. Therefore, the GRACE results presented in this chapter, are based on 45 CNES solutions, and the time coverage of these are also listed in Table 9.1.

9.1.1 Mass changes

Monthly mass change estimates of the GrIS are derived from the 45 CNES solutions (Table 9.1), using the methods described in Chap. 7. The ICE-5G(VM2) GIA correction is used,

Table 9.1: *Time coverage of overlapping ICESat and CNES data.*

ICESat campaign	Time span [YYYY-DOY]	CNES solutions time span [YYYY-DOY]
L2A	2003-277 - 2003-322	2003-275 - 2003-324
L2B	2004-048 - 2004-080	2004-050 - 2004-079
L2C	2004-139 - 2004-172	2004-140 - 2004-169
L3A	2004-277 - 2004-313	2004-280 - 2004-309
L3B	2005-048 - 2005-083	2005-044 - 2005-083
L3C	2005-140 - 2005-173	2005-144 - 2005-173
L3D	2005-294 - 2005-327	2005-294 - 2005-323
L3E	2006-053 - 2006-086	2006-049 - 2006-088
L3F	2006-144 - 2003-176	2006-139 - 2006-178
L3G	2006-298 - 2003-331	2006-299 - 2006-328
L3H	2007-071 - 2007-104	2007-074 - 2007-103
L3I	2007-275 - 2007-308	2007-274 - 2007-313
L3J	2008-048 - 2008-081	2008-049 - 2008-078

both in the GRACE and ICESat analysis.
The mass change result is seen (in blue) in Fig. 9.1. The mass balance is found to be -216 $\pm$ 40 Gt yr^{-1}, indicated by the red line in Fig. 9.1.
This MB estimate is in good agreement with the ICESat derived MB of -210 $\pm$ 21 Gt yr^{-1} (Sørensen et al., 2010a). The spatial distribution of the mass changes from GRACE and ICESat are shown for comparison in Fig. 9.2, where the ICESat result is given in [Mt yr^{-1}] at a 5 km grid, and the GRACE result is given in [mm yr^{-1}] of water equivalent. As discussed earlier, in spite of the difference in resolution, both results show marginal mass loss, which is largest along the south-east and west coasts of Greenland, and a small mass gain in the interior part.

Basin scale comparison

Some regions of the ice sheet are responding much more dramatically to the climate changes than others (Chap. 3). This makes it interesting to investigate the behavior of the different regions. Here, the mass changes are investigated on a drainage basin scale. The basin scale definition used, is adapted from Hardy et al. (2000). It assumes a division of the GrIS into seven drainage basins. The outline of the drainage basins and the denoted numbering is shown in Fig. 9.3. Basin scale studies of mass and volume changes of the GrIS have also been carried out by e.g. Luthcke et al. (2006); Wouters et al. (2008); Slobbe et al. (2008).

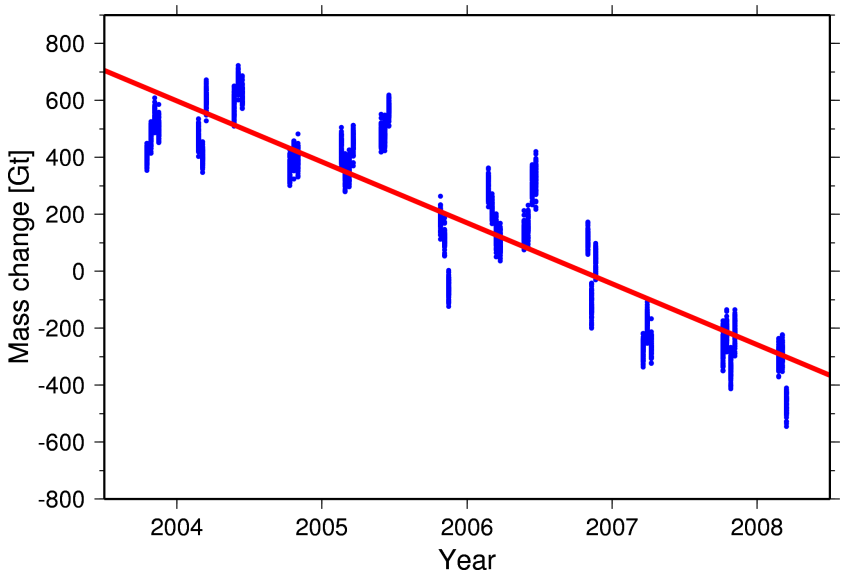

Figure 9.1: *Monthly mass changes from the 45 CNES solutions with time coverage approximately equal to that of the ICESat data.*

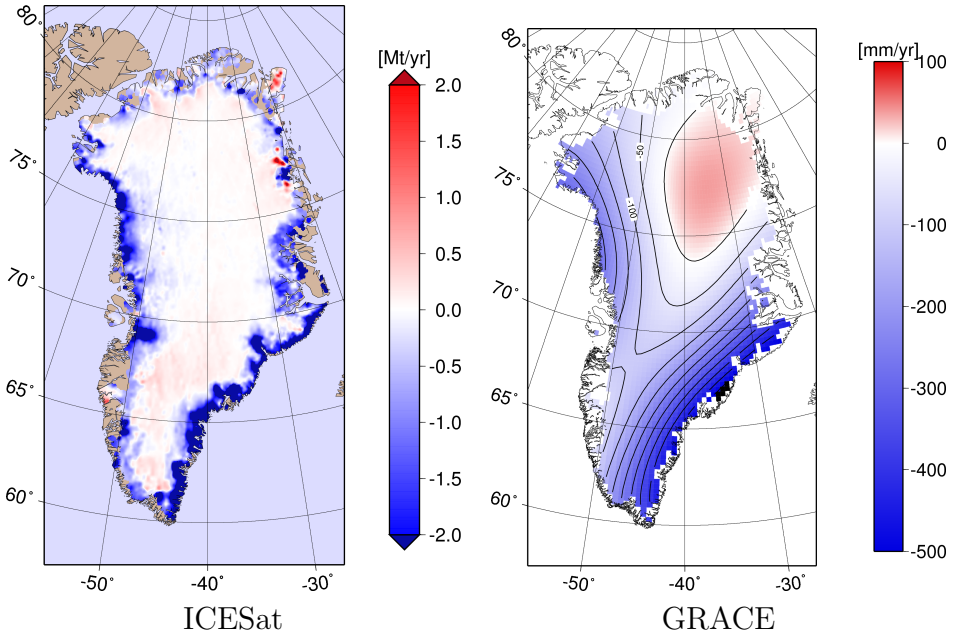

Figure 9.2: *Mass changes from overlapping ICEsat and GRACE data. The ICESat mass changes are given in [Mt] at a 5×5 km grid, while the GRACE result is given as mm water equivalent.*

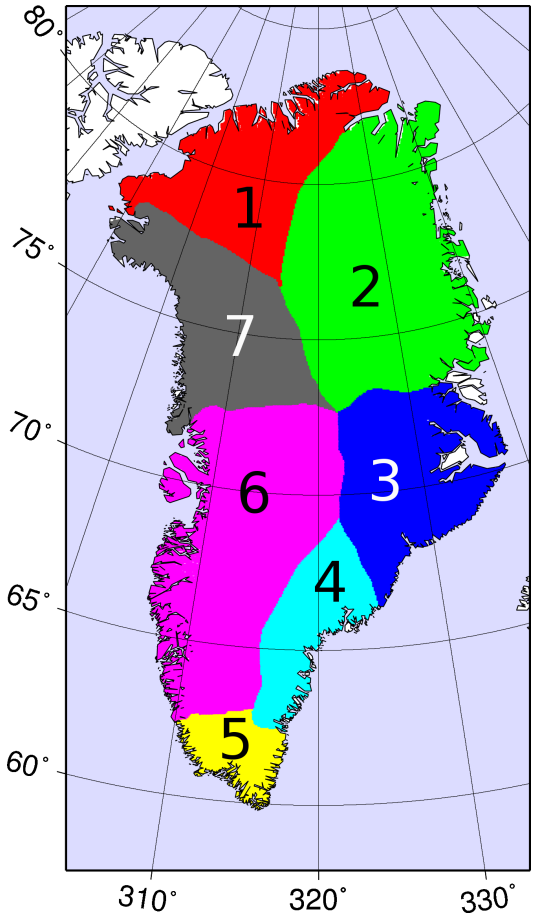

Figure 9.3: *Outline of Greenland divided into seven drainage basins. The drainage basin definition is adapted from Hardy et al. (2000).*

Table 9.2: *Basin scale mass changes from ICESat (M3) and GRACE. The basins are defined in Fig. 9.3.*

Basin	**Mass change [Gt/yr] ICESat, M3**	**Mass change [Gt/yr] GRACE**
1	-5.3	-13.5
2	-8.0	4.1
3	-41.3	-45.5
4	-53.3	-39.2
5	-20.1	-17.4
6	-38.1	-62.8
7	-43.5	-41.7
Total	-209.6	-216

The mass changes of each drainage basin, derived from overlapping ICESat and GRACE data, are listed in Table 9.2. It is seen that even though the total MB estimates of the ice sheet are very similar, there is not complete consensus on the results for all drainage basins.
A comparison shows, that the mass changes in basin 3, 5, and 7 agree well. For basin 1, GRACE predicts a larger mass loss than ICESat, and for basin 2, GRACE predicts a small mass increase, while ICESat predicts a small mass loss.
The largest ICESat derived mass change ($-53.3\,\mathrm{Gt\,yr^{-1}}$) is found in basin 4, while the largest mass change from GRACE ($-62.8\,\mathrm{Gt\,yr^{-1}}$) is located in basin 6.

The difference between the basin scale mass changes from ICESat and GRACE may be due to the difference in resolution. The smoothness of the GRACE solution might cause the mass change from one basin to leak into the neighbour basins.

9.1.2 Gravity trend comparisons

Besides comparing the total net mass balance derived from the two data sets, it is interesting also to compare the spatial pattern of changes observed, and to see how well they agree. In order to overcome the issue of different resolutions, a comparison in the gravity domain is also presented.
The mass changes derived from ICESat at a 5×5 km grid are treated as mass anomalies, and the gravity disturbance from these are determined in an altitude of 480 km (Tscherning et al., 1992), corresponding to the altitude of the GRACE satellites. The relative

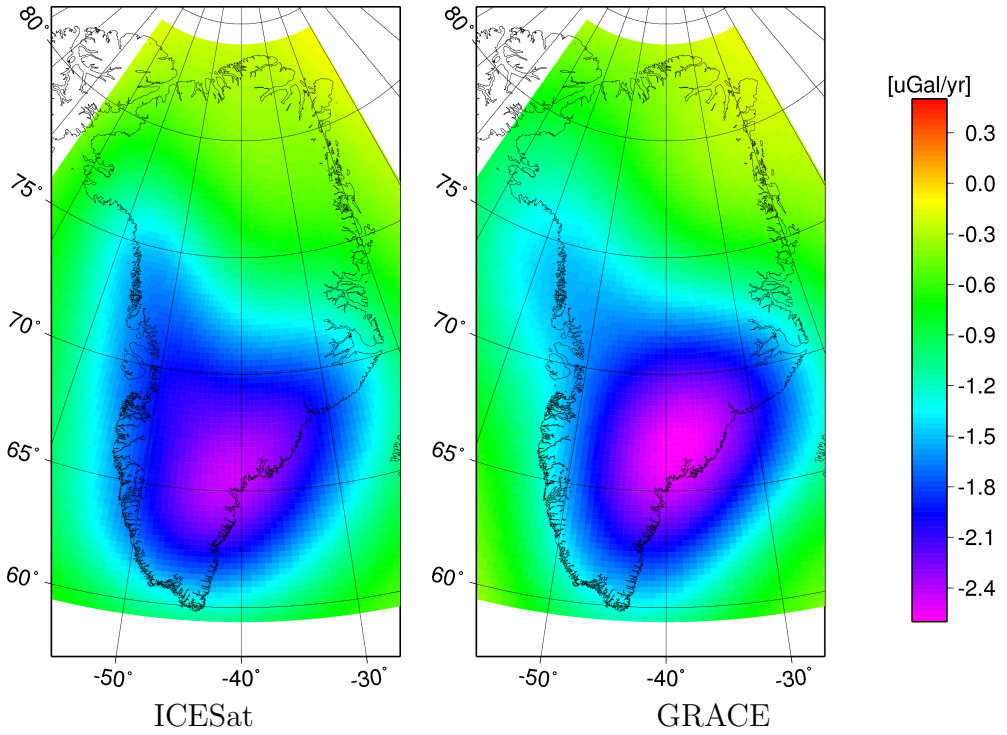

Figure 9.4: *Gravity trend in satellite altitude from overlapping ICEsat and GRACE data.*

elevations of the ICESat mass anomalies are based on the Greenland DEM from Bamber et al. (2001b). In order to make the gravity trend comparable with the GRACE observations, the ICESat signal is low-pass filtered.
A comparison of the GRACE and ICESat gravity signature is provided in Fig. 9.4. This comparison shows similar gravity signature from GRACE and ICESat, with a maximum negative trend located over Southeast Greenland, with a tail up along the west coast.
The amplitude of the GRACE gravity signature is larger than the one from ICESat. This could be the result of the undersampling of the southern part of the ice sheet by ICESat, see e.g. Fig. 8.1. Maybe some of the thinning in this region is not covered by the satellite groundtrack.

Chapter 10

The GrIS contribution to sea-level rise

This chapter contains a discussion of the GrIS contribution to the global sea level rise. The RSL changes caused by the GrIS mass loss, along with the eustatic sea level change obtained from the ICESat and GRACE derived MB estimates, are presented.

The observed present-day global warming of the Earth (Sect. 3.1), causes the global sea level to rise. Components of this sea level rise are the steric effect (thermal expansion), the melting of small glaciers and ice caps, and the increased melting and dynamic changes of the large ice sheets (Solomon et al., 2007).
Figure 10.1 shows the past, measured and projected future sea level changes. The estimate of past sea level is shown in grey, the measured sea level is shown in red, with the satellite measurements indicated by the green line. The blue area represents the range of model projections for the A1B (medium CO_2 growth) scenario. The IPCC projected sea level rise by year 2100 (compared to 1980-1999) from various scenarios, is in the range 0.18-0.59 m. It is based on the assumption, that the part of the present-day mass imbalance of the large ice sheets, which is due to an acceleration in flow, will remain unchanged.

As concluded in Chap. 9, analysis of GRACE and ICESat data agree, that the GrIS in the period 2003-2008 was experiencing a significant net mass loss. The mass loss of the GrIS contributes to the eustatic sea-level rise. Assuming a net mass balance of -210±21 $\mathrm{Gt\,yr^{-1}}$, as determined from the ICESat analysis (Sørensen et al., 2010a), the rate of eustatic sea level rise, caused by the GrIS, is 0.576±0.057 mm/yr.
The RSL change is calculated using a suitably modified version of SELEN (Sect. 6.4), from the ICESat derived GrIS mass changes shown in Fig. 8.8(a), Sect. 8.3. The mass changes are implemented as a one step ice history, and the result is seen in Fig. 10.2. It is seen, that the RSL changes, caused by the mass changes of the GrIS, are not evenly distributed over the globe. The re-distribution of mass in and on the Earth, caused by the ice disappearing, affects the shape of the geoid. The added water is distributed according to the altered geoid.

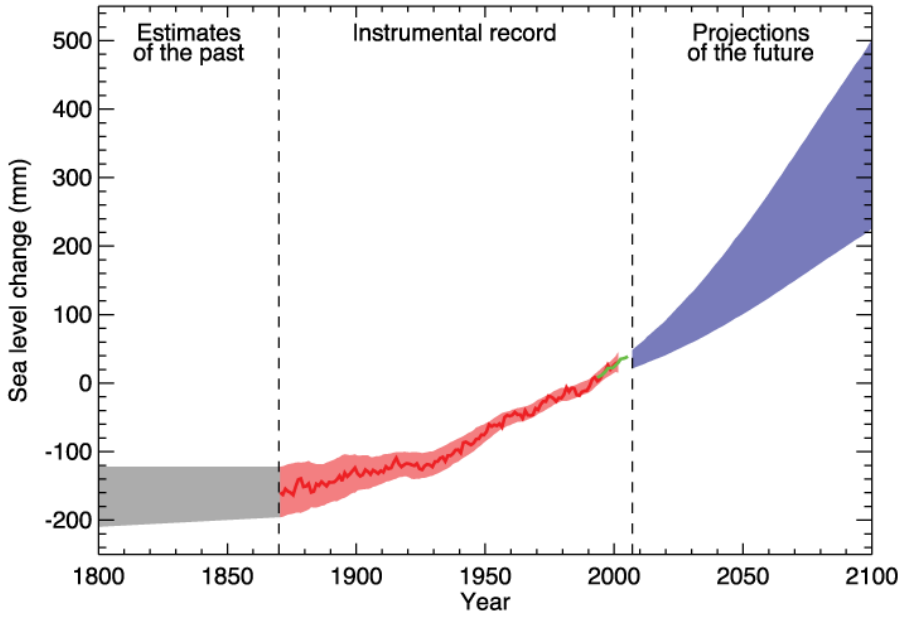

Figure 10.1: *Past, measured and projected sea level changes from Solomon et al. (2007). The estimates of past sea level are shown in grey and the measured sea level is shown in red, with the satellite measurements indicated by the green line. The blue area represents the range of model projections for the A1B (medium CO_2 growth) scenario.*

Table 10.1: *Rate of eustatic sea-level rise from GRACE and ICESat derived MB.*

	Time Span YYYY-MM	**Rate of eustatic sea level rise [mm/yr]**
ICESat, M1	2003-10 - 2008-11	0.549 ± 0.062
ICESat, M2	2003-10 - 2008-11	0.429 ± 0.040
ICESat, M3	2003-10 - 2008-11	0.580 ± 0.064
ICESat, M4	2003-10 - 2008-11	0.330 ± 0.064
GRACE, JPL	2002-04 - 2010-07	0.292 ± 0.075
GRACE, CSR	2002-04 - 2010-07	0.626 ± 0.094
GRACE, GFZ	2002-08 - 2010-07	0.601 ± 0.094
GRACE, CNES	2002-08 - 2010-05	0.637 ± 0.111
GRACE, ITG	2002-08 - 2009-08	0.634 ± 0.116

The geoid height, and hence the relative sea level, will be lowered near a melting ice sheet. Since mass is removed from land, the gravitational attraction is decreased. So, even though the eustatic sea level will rise as a result of the ice sheets loosing mass, the near-field RSL is lowered.
It is seen in Fig. 10.2, that the relative sea level is lowered by approximately 1 mm/yr in the whole Greenland region, both due to the lowered geoid, but also due to the elastic uplift of the bedrock. As an example, it is also seen that Denmark is located in a region, in which the RSL change from the GrIS is close to zero. The far-field (the whole southern hemisphere) sea-level change is dominated by the eustatic signal. Following these arguments, a mass loss of the Antarctic ice sheet would, in Denmark, be observed as a RSL change, close to the eustatic RSL.

The rate of eustatic sea level rise from the MB results obtained in this study, are listed in Table 10.1. The sea level rise and error estimates from the listed ICESat data, are based on the results of Sørensen et al. (2010a), together with the three different GIA corrections shown in Fig. 6.4.

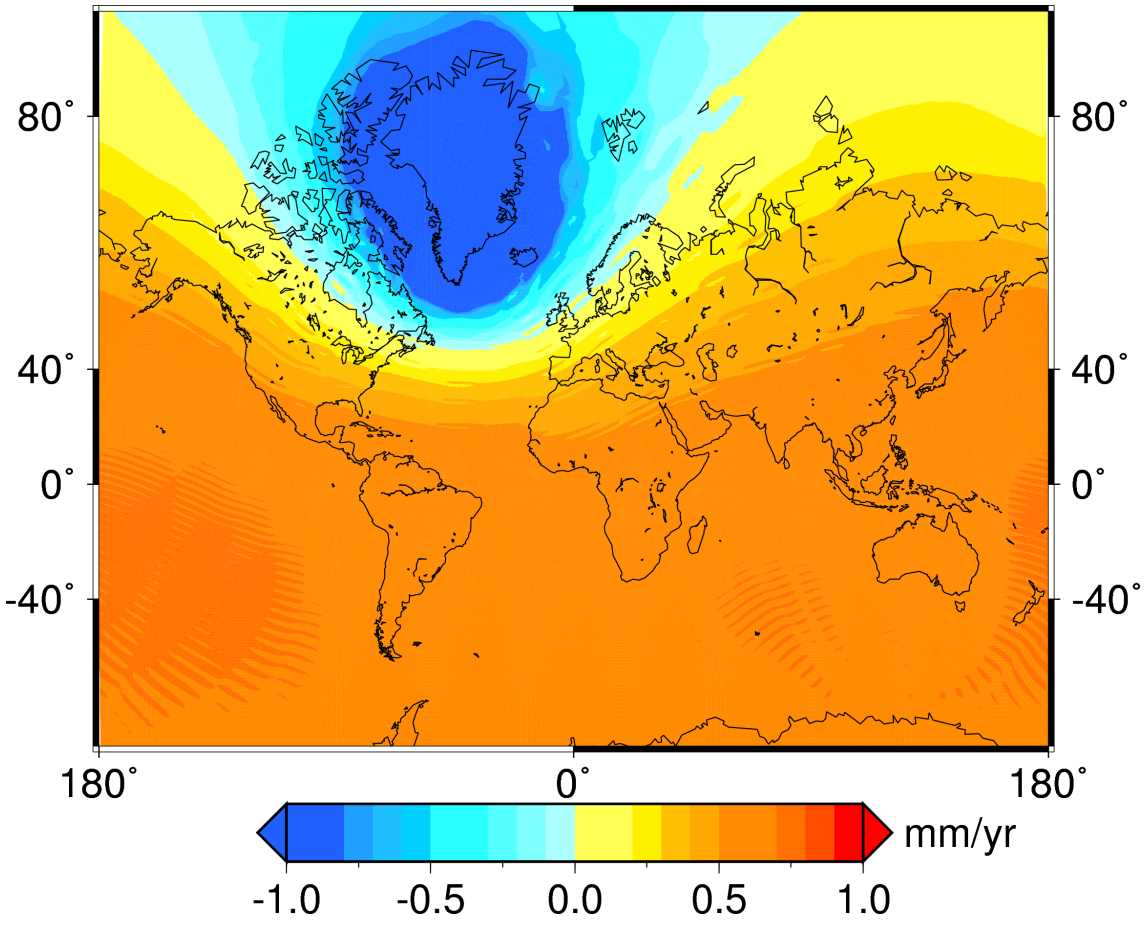

Figure 10.2: *The relative sea-level changes due to the present-day mass changes of the GrIS, determined from ICESat data using M3.*

Chapter 11

Antarctica - a case study

The methods developed for this Ph.D. project, can be used to investigate the changes of other ice covered regions than the GrIS.
In this chapter, a case study on the Antarctic ice sheet is presented, to highlight the applicability of the developed methods. Changes of the Antarctic ice sheet have been investigated, using ICESat and GRACE data by e.g. Ramillien et al. (2006); Shum et al. (2008); Barletta et al. (2008); Gunter et al. (2009); Velicogna (2009) and Pritchard et al. (2009)
Constraining the mass balance of the Antarctic ice sheet is of utmost importance, because it contains approximately 90% of the Earth's ice, and could become the largest contributor to sea level rise.

The M3 method for deriving along-track elevation changes from ICESat data (Sørensen et al., 2010a), was applied to the Antarctic ice sheet. The ICESat data culling procedure and the time span of data is the same as presented in ibid. The resulting $\left(\frac{\mathrm{d}H}{\mathrm{d}t}\right)$ estimates are shown in Fig. 11.1.
The ICESat analysis show significant rate of elevation change in some regions of the ice sheet. A distinct dipole pattern is observed in the region labeled **1** in Fig. 11.1, which is caused by a thickening of the Kamb ice stream and a thinning of the Whillans catchment. A clear thinning is also found in the Amundsen Sea Embayment (labeled **2** in Fig. 11.1), which is drained by the e.g. the Pine Island and Thwaites glaciers.

Figure 11.2 shows the gravity trend at satellite altitude (480 km) over Antarctica. It is derived from CSR level-2 GRACE data, which has been post-processed as described in Chap. 7. For Antarctica a smoothing parameter of $a = 10^{12}$ is chosen in the de-striping procedure applied to the monthly GRACE solutions (Sect. 7.3).
A clear negative trend in gravity, indicating mass loss, is seen over the Amundsen Sea Embayment. This is corresponding well with the large thinning observed by ICESat in this region.

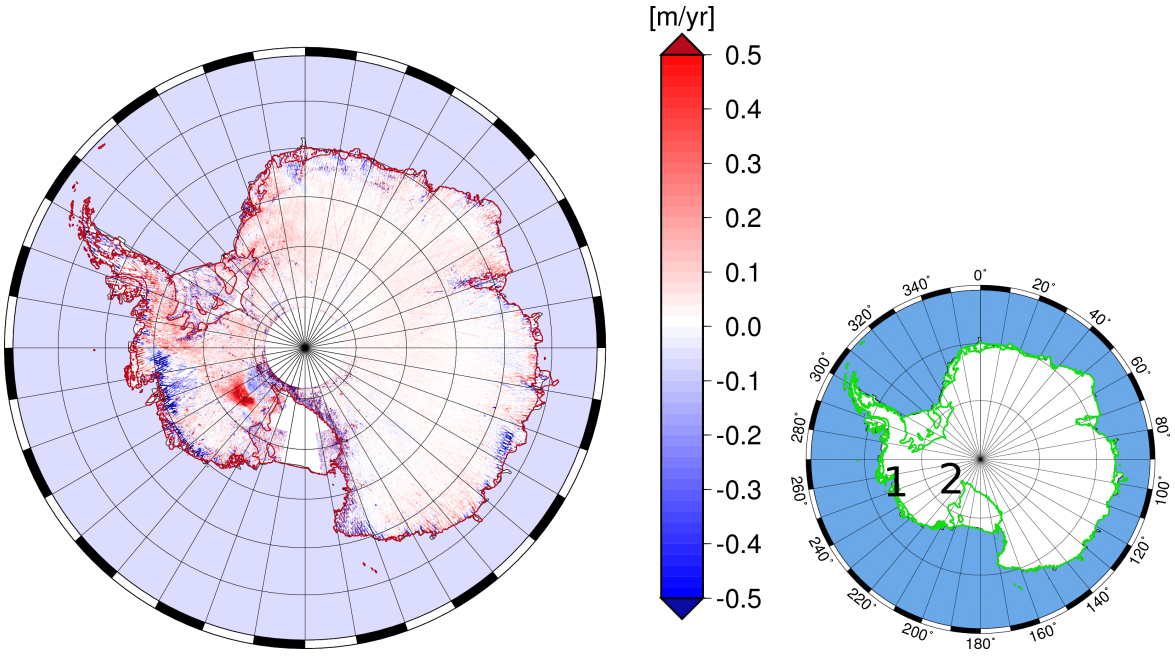

Figure 11.1: *Rate of elevation changes of the Antarctic ice sheet derived from ICESat data 2003-2008, using M3.*

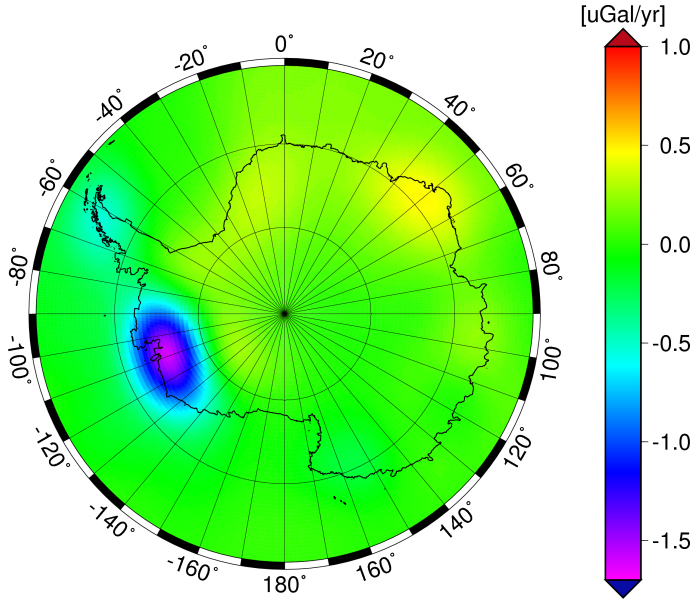

Figure 11.2: *Gravity changes over the Antarctic ice sheet derived from GRACE CSR level-2 data 2002-2010.*

Although GIA-induced trends in Amundsen Sea Embayment are considerably smaller than those induced by surface mass changes (Sasgen et al., 2010), seperating GIA and ice mass balance of the entire Antarctic continent remains challenging.
The GIA correction plays a major role in Antarctica, and the choice of GIA model greatly affects the GRACE derived MB (Shum et al., 2008). The GIA-induced rate of change of geoid height for ICE-3G (TP), ICE-5G (VM2) and ANU05 (KL) (Sect. 6.4) are shown in Fig. 11.3. Clear differences in the pattern and magnitude of the signal are seen. For Greenland, the uncertainty in the GIA modelling is a minor issue, but for Antarctica, the GIA signal is of the same order of magnitude as the MB (Cazenave and Chen, 2010).

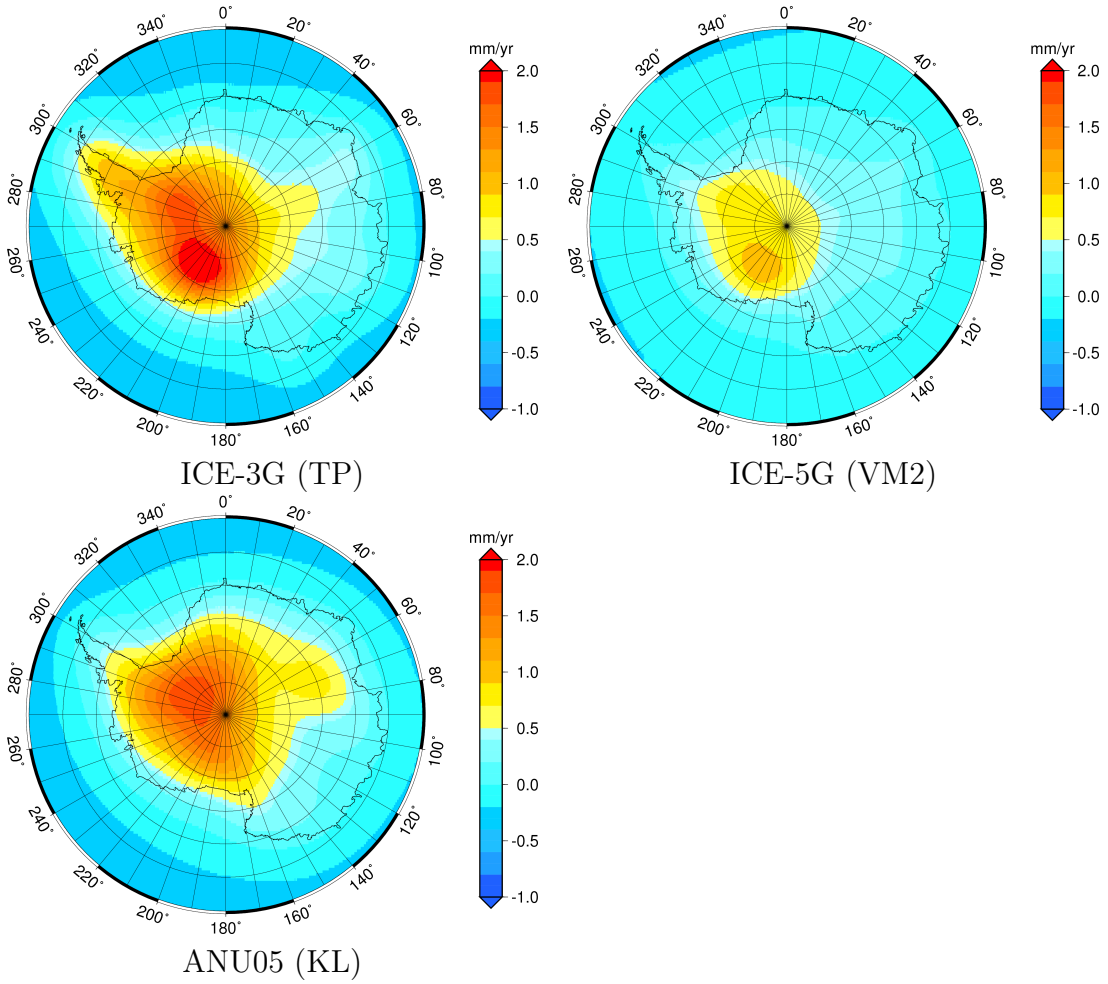

Figure 11.3: *Present-day rate of change of geoid height in Antarctica, based on ICE-3G (TP), ICE-5G (VM2) and ANU05 (KL), respectively.*

Chapter 12

Conclusions and suggestions for future work

In this PhD project, changes of the GrIS for the time period 2002-2010 were derived from GRACE data, and from ICESat data 2003-2008 .

The gravity changes observed by the GRACE satellites, were used in an inversion scheme to determine the associated ice mass changes on the GrIS. Post-processing of the GRACE data included substitution of the $\bar{C}_{20}$ coefficient with those obtained from SLR and correcting for the solid Earth response to mass unloading and de-striping of the monthly solutions. The spatial distribution of the obtained mass changes from GRACE showed large coastal mass losses and a small interior mass gain. The largest mass loss was found along the southeast coast, in which area the large outlet glaciers Helheim and Kangerdlussuaq are located. A clear mass loss was also seen propagating up along the west coast.
Results were derived from five level-2 data sets, and good agreement was found for mass loss models based on ITG, CSR, GFZ and CNES results, while the corresponding mass loss model based on JPL solutions, was significantly smaller. This lack of consensus between the JPL and the other solutions needs further investigation.
Excluding the JPL solution, the obtained net mass balance estimates from GRACE data from August 2002 - August 2009 are in the range -209$\pm$32Gt yr^{-1} to -242$\pm$36Gt yr^{-1}.

Four methods, to derive rate of elevation change from the ICESat altimetry data, were developed. The time coverage of the ICESat data was October 2003 to March 2008. Data culling was applied to remove data associated with a suspected high uncertainty. All four methods revealed a spatial pattern of coastal ice sheet thinning, which agrees with the GRACE results, though it did contain much more details. The thinning of several large outlet glaciers was clearly seen, and a small but consistent thickening of the central part of the ice sheet was observed.
Elevation change corrections were applied to the derived ICESat elevation changes, and it was concluded that the firn compaction was the most important of the applied corrections. This fact highlighted the need for validation of such models, and one approach to

such a validation is the use of layer detection in radar data and N-probe data. Such an approach was described in Sørensen et al. (2010b), which showed good correlation between the modelled firn layers and those from ASIRAS data along the EGIG line, west of the ice divide. Such validations should be expanded in the future, to determine how well the firn compaction model behaves.

A kriging interpolation was used to determine the total volume change of the GrIS. Modelled surface densities were then used to convert the volume change into a net mass balance estimate. The three methods (M1-M3) for deriving elevation changes along-track, resulted in mass balance estimates ranging from -155±12 Gt yr^{-1} to -210±21 Gt yr^{-1}. The cross-over method showed a mass loss of only -118±21 Gt yr^{-1}, but this low result was expected due to the poor spatial coverage, especially in southern Greenland. The preferred method (M3) yields a mass balance of -210±21 Gt yr^{-1}.

Fig. 12.1 shows how the results obtained in this study compare with other published results. A number of published GrIS MB estimates (corresponding to those shown in Fig. 3.5) are shown in grey. The range of the GRACE MB results (excluding JPL) obtained in this study, is shown in red, and the range of the ICESat results (excluding M4) is shown in blue.

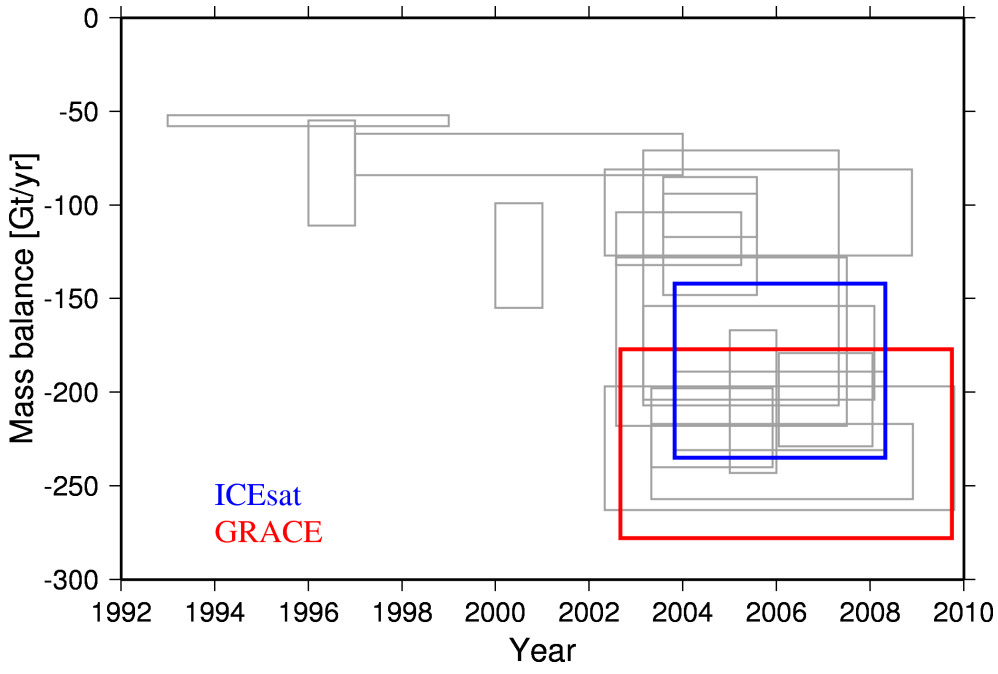

Figure 12.1: *Published mass balance estimates of the GrIS. The range of the GRACE MB results obtained in this study is shown in red and the range of the ICESat results is shown in blue.*

Some interesting future work would be to use the developed methods for deriving elevation changes on combined data sets, such as e.g. LiDAR data from different field campaigns currently conducted by DTU Space, and from the IceBridge project. In more regional studies, it would be very interesting to test if the elevation changes are better fitted to other functions than the linear trend in time, which is assumed in this study.
An approach that could lead to an increased spatial resolution of the GRACE derived mass changes, is forward modelling, in which maps of mass change based on ICESat results could be used as an initial model to optimally fit the GRACE measurements.

The results outlined in Chap. 6 indicate that the GIA modelling is uncertain. There is currently much research going on, focusing on better to constrain the ice history models and Earth parameters needed as input in the GIA predictions. It was shown that in spite of the large variability in the GIA corrections used, the effect was relatively small for Greenland. For Antarctica, it is of utmost importance to better constrain the GIA signal, to derive more reliable mass balance results.
In this respect, it could be interesting to use ICESat and GRACE measurement in combination, in order to derive the GIA signal, both in Greenland and Antarctica (Wahr et al., 2000; Riva et al., 2009).

The results of this study showed that the GrIS has indeed experienced large changes in recent years. Two independent mass balance estimates of the GrIS, from satellite data were presented. These were found to be in good agreement, and confirm a significant mass loss of the ice sheet for the period 2003 to present.
However, there is still not complete consensus on MB estimates, which are dependent on the data sets and methods chosen for the analysis. Therefore, it is important in the future, to investigate and understand the discrepancies.

Bibliography

Abdalati, W., Krabill, W., Frederick, E., Manizade, S., Martin, C., Sonntag, J., Swift, R., Thomas, R., Wright, W., and Yungel, J. (2001). Outlet glacier and margin elevation changes: Near-coastal thinning of the Greenland ice sheet. *J. Geophys. Res.*, 106(D24):33729–33741.

Abshire, J. B., Sun, X., Riris, H., Sirota, J. M., McGarry, J. F., Palm, S., Yi, D., and Liiva, P. (2005). Geoscience Laser Altimeter System (GLAS) on the ICESat Mission: On-orbit measurement performance. *Geophys. res. lett.*, 32:L21S02.

Andersen, O. B. and Knudsen, P. (2009). DNSC08 mean sea surface and mean dynamic topography models. *J. Geophys. Res.*, 114(C11):C11001.

Andersen, O. B., Seneviratne, S. I., Hinderer, J., and Viterbo, P. (2005). GRACE-derived terrestrial water storage depletion associated with the 2003 European heat wave. *Geophys. Res. Lett.*, 32(18):L18405.

Bae, S. and Schutz, B. E. (2002). Precision attitude determination (PAD). *Algorithm Theoretical Basis Documents (ATBD).*

Bales, R. C., Guo, Q., Shen, D., McConnell, J., Du, G., Burkhart, J., Spikes, V., Hanna, E., and Cappelen, J. (2009). Annual accumulation for Greenland updated using ice core data developed during 2000–2006 and analysis of daily coastal meteorological data. *J. Geophys. Res.*, 114(D6):D06116.

Bamber, J., Layberry, R., and Gogineni, S. (2001a). A new ice thickness and bed data set for the Greenland ice sheet. I- Measurement, data reduction, and errors. *J. Geophys. Res.*, 106(D4):33773–33780.

Bamber, J. L., Ekholm, S., and Krabill, W. B. (2001b). A new, high-resolution digital elevation model of Greenland fully validated with airborne laser altimeter data. *J. Geophys. Res.*, 106(B4):6733–6745.

Barletta, V. R., Sabadini, R., and Bordoni, A. (2008). Isolating the PGR signal in the GRACE data: impact on mass balance estimates in Antarctica and Greenland. *Geophys. J. Int.*, 172(1):18–30.

Baur, O., Kuhn, M., and Featherstone, W. E. (2009). GRACE-derived ice-mass variations over Greenland by accounting for leakage effects. *J. Geophys. Res.*, 114(B6):B06407.

Bettadpur, S. (2003). Level-2 gravity field product user handbook. *The GRACE Project*.

Bettadpur, S. (2007a). Gravity Recovery and Climate Experiment. Product Specification Document. *GRACE 327-720 (CSR-GR-03-02)*.

Bettadpur, S. (2007b). UTCSR level-2 processing standards document for level-2 product release 0004. GRACE 327-742. Technical report, CSR-GR-03-03, 17 pp., Center for Space Research, Univ. Texas, Austin.

Brenner, A. C., DiMarzio, J. P., and Zwally, H. J. (2007). Precision and accuracy of satellite radar and laser altimeter data over the continental ice sheets. *Geoscience and Remote Sensing, IEEE Transactions on*, 45(2):321–331.

Brenner, A. C., Zwally, H. J., Bentley, C. R., Csatho, B. M., Harding, D. J., Hofton, M. A., Minster, J. B., Roberts, L. A., Saba, J. L., Thomas, R. H., et al. (2003). Geoscience Laser Altimeter System (GLAS)-Derivation of Range and Range Distributions From Laser Pulse Waveform Analysis for Surface Elevations, Roughness, Slope, and Vegetation Heights. *Algorithm Theoretical Basis Document-Version*, 4.

Bruinsma, S., Lemoine, J.-M., Biancale, R., and Vales, N. (2010). CNES/GRGS 10-day gravity field models (release 2) and their evaluation. *Adv. in Space Res.*, 45:587–601.

Cazenave, A. and Chen, J. (2010). Time-variable gravity from space and present-day mass redistribution in the Earth system. *Earth and Planetary Science Letters*, 298:263–274.

Cazenave, A., Dominh, K., Guinehut, S., Berthier, E., Llovel, W., Ramillien, G., Ablain, M., and Larnicol, G. (2009). Sea level budget over 2003-2008: A reevaluation from GRACE space gravimetry, satellite altimetry and Argo. *Global Planet. Change*, 65(1-2):83–88.

Chambers, D. P., Wahr, J., and Nerem, R. S. (2004). Preliminary observations of global ocean mass variations with GRACE. *Geophys. Res. Lett.*, 31(13):L13310.

Chen, J. L., Rodell, M., Wilson, C. R., and Famiglietti, J. S. (2005). Low degree spherical harmonic influences on Gravity Recovery and Climate Experiment (GRACE) water storage estimates. *Geophys. Res. Lett*, 32.

Chen, J. L., Wilson, C. R., and Tapley, B. D. (2006). Satellite gravity measurements confirm accelerated melting of Greenland ice sheet. *Science*, 313(5795):1958.

Cheng, M. and Tapley, B. D. (2004). Variations in the Earth's oblateness during the past 28 years. *J. Geophys. Res.*, 109(B9):B09402.

Christensen, O. B., Drews, M., Christensen, J. H., Dethloff, K., Ketelsen, K., Hebestadt, I., and Rinke, A. (2006). The HIRHAM Regional Climate Model. Version 5. Technical Report 06-17, DMI technical report.

CU-GRACE (2010). Cu, boulder. *http://geoid.colorado.edu/grace/grace.php*, Accessed, Nov. 2010.

Dahl-Jensen, D., Mosegaard, K., Gundestrup, N., Clow, G. D., Johnsen, S. J., Hansen, A. W., and Balling, N. (1998). Past temperatures directly from the Greenland ice sheet. *Science*, 282(5387):268.

Denton, G. H. and Hughes, T. J. (1981). *The last great ice sheets*. Wiley New York.

Dziewonski, A. M. and Anderson, D. L. (1981). Preliminary reference Earth model* 1. *Physics of the Earth and Planetary Interiors*, 25(4):297–356.

Farrell, W. E. and Clark, J. A. (1976). On Postglacial Sea Level. *Geophys J. Roy. Astr. S.*, 46(3):647–667.

Fengler, M. J., Freeden, W., Kohlhaas, A., Michel, V., and Peters, T. (2007). Wavelet modeling of regional and temporal variations of the Earth's gravitational potential observed by GRACE. *J. Geod.*, 81(1):5–15.

Flechtner, F. (2007). GFZ Level-2 Processing Standards Document for Product Release 0004, GRACE 327-743. Technical report, GR-GFZ-STD-001, GeoForschungsZentrum, Potsdam.

Fleming, K. and Lambeck, K. (2004). Constraints on the Greenland Ice Sheet since the Last Glacial Maximum from sea-level observations and glacial-rebound models. *Quat. Sci. Rev.*, 23(9-10):1053–1077.

Fricker, H. A., Borsa, A., Minster, B., Carabajal, C., Quinn, K., and Bills, B. (2005). Assessment of ICESat performance at the salar de Uyuni, Bolivia. *Geophys. Res. Lett.*, 32:L21S06.

Funder, S. and Hansen, L. (1996). Greenland ice sheet - a model for its culmination and decay during and after the last glacial maximum. *Bulletin of the Geology Society of Denmark*, 42:137–152.

GRACE-CSR (2010). Center for Space Research, University of Texas. *http://www.csr.utexas.edu/grace/spacecraft/sis.html*, Accessed, Nov. 2010.

GRACE-GFZ (2010). GeoForschungsZentrum. *http://op.gfz-potsdam.de/grace/*, Accessed Oct. 2010.

GRACE-Tellus (2010). NASA, JPL. *http://grace.jpl.nasa.gov/*, Accessed, Nov. 2010.

Gunter, B., Urban, T., Riva, R., Helsen, M., Harpold, R., Poole, S., Nagel, P., Schutz, B., and Tapley, B. (2009). A comparison of coincident GRACE and ICESat data over Antarctica. *J. Geodesy*, 83:1051–1060.

Han, D. and Wahr, J. (1995). The viscoelastic relaxation of a realistically stratified earth, and a further analysis of postglacial rebound. *Geophys. J. Int.*, 120(2):287–311.

Han, S. C., Jekeli, C., and Shum, C. K. (2004). Time-variable aliasing effects of ocean tides, atmosphere, and continental water mass on monthly mean GRACE gravity field. *J. geophys. Res*, 109.

Han, S. C., Shum, C. K., Jekeli, C., Kuo, C. Y., Wilson, C., and Seo, K. W. (2005). Non-isotropic filtering of GRACE temporal gravity for geophysical signal enhancement. *Geophys. J. Int.*, 163(1):18–25.

Hanna, E., Cappelen, J., Fettweis, X., Huybrechts, P., Luckman, A., and Ribergaard, M. (2009). Hydrologic response of the Greenland ice sheet: the role of oceanographic warming. *Hydrol. Process.*, 23(1):7–30.

Hardy, R., Bamber, J., and Orford, S. (2000). The delineation of drainage basins on the Greenland ice sheet for mass-balance analyses using a combined modelling and geographical information system approach. *Hydrological Processes*, 14(11-12):1931–1941.

Heiskanen, W. A. and Moritz, H. (1967). *Physical Geodesy*. Freeman and Co., 1st edition.

Holland, D. M., Thomas, R. H., De Young, B., Ribergaard, M. H., and Lyberth, B. (2008). Acceleration of Jakobshavn Isbrae triggered by warm subsurface ocean waters. *Nature Geoscience*, 1(10):659–664.

Howat, I. M., Joughin, I., Fahnestock, M., Smith, B. E., and Scambos, T. A. (2008a). Synchronous retreat and acceleration of southeast Greenland outlet glaciers 2000-06: ice dynamics and coupling to climate. *J. Glaciol*, 54:646–660.

Howat, I. M., Joughin, I., and Scambos, T. A. (2007). Rapid changes in ice discharge from Greenland outlet glaciers. *Science*, 315(5818):1559–1561.

Howat, I. M., Smith, B. E., Joughin, I., and Scambos, T. A. (2008b). Rates of southeast Greenland ice volume loss from combined ICESat and ASTER observations. *Geophys. Res. Lett.*, 35:L17505.

Hvidegaard, S. M., Sørensen, L. S., and Forsberg, R. (2010). ASTER GDEM validation using LiDAR data over coastal regions of Greenland. *Rem. Sens. Lett.*

ICGEM (2010). Gfz, helmholtz centre potsdam. *http://icgem.gfz-potsdam.de/ICGEM/ICGEM.html*, Accessed, Nov. 2010.

Johnsen, S. J., Dahl-Jensen, D., Dansgaard, W., and Gundestrup, N. (1995). Greenland palaeotemperatures derived from GRIP bore hole temperature and ice core isotope profiles. *Tellus B*, 47(5):624–629.

Johnston, P. (1993). The effect of spatially non-uniform water loads on prediction of sea-level change. *Geophys. J. Int.*, 114(3):615–634.

Johnston, P. and Lambeck, K. (1999). Postglacial rebound and sea level contributions to changes in the geoid and the Earth's rotation axis. *Geophys. J. Int.*, 136(3):537–558.

Joughin, I., Das, S. B., King, M. A., Smith, B. E., Howat, I. M., and Moon, T. (2008). Seasonal speedup along the western flank of the Greenland Ice Sheet. *Science*, 320(5877):781.

Joughin, I., Smith, B. E., Howat, I. M., Scambos, T., and Moon, T. (2010). Greenland flow variability from ice-sheet-wide velocity mapping. *J. Glaciol.*, 56:415–430(16).

Khan, S. A., Liu, L., Wahr, J., Howat, I., Joughin, I., van Dam, T., and Fleming, K. (2010a). GPS measurements of crustal uplift near Jakobshavn Isbræ due to glacial ice mass loss. *J. Geophys. Res.*, 115(B9):B09405.

Khan, S. A., Van dam, T., Hamilton, G. S., Stearns, L. A., Wahr, J., Larson, K. M., and Francis, O. (2007). Elastic uplift in southeast Greenland due to rapid ice mass loss. *Geophys. Res. Lett.*, 34(21):L21701.

Khan, S. A., Wahr, J., Bevis, M., Velicogna, I., and Kendrick, E. (2010b). Spread of ice mass loss into northwest Greenland observed by GRACE and GPS. *Geophys. Res. Lett.*, 37:L06501.

Khan, S. A., Wahr, J., Leuliette, E., van Dam, T., Larson, K. M., and Francis, O. (2008). Geodetic measurements of postglacial adjustments in Greenland. *J. Geophys. Res.*, 113(B2):B02402.

Krabill, W., Abdalati, W., Frederick, E., Manizade, S., Martin, C., Sonntag, J., Swift, R., Thomas, R., Wright, W., and Yungel, J. (2000). Greenland Ice Sheet: High-Elevation Balance and Peripheral Thinning. *Science*, 289(5478):428–430.

Krabill, W., Hanna, E., Huybrechts, P., Abdalati, W., Cappelen, J., Csatho, B., Frederick, E., Manizade, S., Martin, C., Sonntag, J., Swift, R., Thomas, R., and Yungel, J. (2004). Greenland Ice Sheet: Increased coastal thinning. *Geophys. Res. Lett.*, 31(24):L24402.

Krogh, P. E., Andersen, O. B., Michailovsky, C. I. B., Bauer-Gottwein, P., Rowlands, D. D., Luthcke, S. B., and Chinn, D. S. (2010). Evaluating terrestrial water storage variations from regionally constrained GRACE mascon data and hydrological models over Southern Africa - preliminary results. *International Journal of Remote Sensing*, 31(14):3899–3912.

Kurtenbach, E., Mayer-Gürr, T., and Eicker, A. (2009). Deriving daily snapshots of the Earth's gravity field from GRACE L1B data using Kalman filtering. *Geophysical Research Letters*, 36(17):L17102.

Kusche, J. (2007). Approximate decorrelation and non-isotropic smoothing of time-variable GRACE-type gravity field models. *J. Geod.*, 81(11):733–749.

Kusche, J., Schmidt, R., Petrovic, S., and Rietbroek, R. (2009). Decorrelated GRACE time-variable gravity solutions by GFZ, and their validation using a hydrological model. *J. Geod.*, 83(10):903–913.

Lambeck, K., Smither, C., and Johnston, P. (1998). Sea-level change, glacial rebound and mantle viscosity for northern Europe. *Geophys. J. Int.*, 134(1):102–144.

Lemoine, J. M., Bruinsma, S., Loyer, S., Biancale, R., Marty, J. C., Perosanz, F., and Balmino, G. (2007). Temporal gravity field models inferred from GRACE data. *Adv. Space Res.*, 39(10):1620–1629.

Leuliette, E. W., Nerem, R. S., and Mitchum, G. T. (2004). Calibration of TOPEX/Poseidon and Jason Altimeter Data to Construct a Continuous Record of Mean Sea Level Changes. *Mar. Geod.*, 27:79–94.

Luthcke, S. B., Rowlands, D. D., Williams, T. A., and Sirota, M. (2005). Reduction of ICESat systematic geolocation errors and the impact on ice sheet elevation change detection. *Geophys. Res. Lett.*, 32(21):L21S05.

Luthcke, S. B., Zwally, H. J., Abdalati, W., Rowlands, D. D., Ray, R. D., Nerem, R. S., Lemoine, F. G., McCarthy, J. J., and Chinn, D. S. (2006). Recent Greenland Ice Mass Loss by Drainage System from Satellite Gravity Observations. *Science*, 314(5803):1286–1289.

Mayer-Gürr, T. (2006). *Gravitationsfeldbestimmung aus der Analyse kurzer Bahnbögen am Beispiel der Satellitenmissionen CHAMP und GRACE*. PhD thesis, Universitäts- und Landesbibliothek Bonn.

Mayer-Gürr, T., Kurtenbach, E., and Eicker, A. (2010). ITG-Grace2010. *http://www.igg.uni-bonn.de/apmg/index.php?id=itg-grace2010*, Accessed Oct. 2010.

Milne, G. A., Mitrovica, J. X., and Schrag, D. P. (2002). Estimating past continental ice volume from sea-level data. *Quat. Sci. Rev.*, 21(1-3):361–376.

Mitrovica, J. X. and Peltier, W. R. (1991). On post-glacial geoid subsidence over the equatorial ocean. *J. Geophys. Res.*, 96(B12):20053–20071.

Mote, T. L. (2007). Greenland surface melt trends 1973–2007: Evidence of a large increase in 2007. *Geophys. Res. Lett.*, 34(22):L22507.

NASA-GLAS (2010). Geoscience Laser Altimeter System. *http://glas.gsfc.nasa.gov/*, Accessed, Nov. 2010.

NASA-IceBridge (2010). IceBridge - An airborne mission for Earth's polar ice. *http://www.nasa.gov/mission_pages/icebridge*, Accessed, Nov. 2010.

NASA-ICESat (2010). Nasa. *http://icesat.gfsc.nasa.gov/icesat*, Accessed, Nov. 2010.

NSIDC (2010). GLAS Altimetry Product Usage Guidance. *http://nsidc.org/data/docs/daac/glas_altimetry/usage.html*, Accessed Mar. 2010.

NSIDC-Parameters (2010). GLAS Altimetry Data Dictionary. *http://nsidc.org/data/docs/daac/glas_altimetry/data_dictionary.html*, Accessed Nov. 2010.

Palmer, S. J. (2010). *Temporal fluctuations in the motion of Arctic ice masses from satellite radar interferometry*. PhD thesis, The University of Edinburgh.

Peltier, W. (2004). Global glacial isostasy and the surface of the ice-age Earth: The ICE-5G (VM2) Model and GRACE. *Annu. Rev. Earth Pl. Sc.*, 32(1):111–149.

Pritchard, H. D., Arthern, R. J., Vaughan, D. G., and Edwards, L. A. (2009). Extensive dynamic thinning on the margins of the Greenland and Antarctic ice sheets. *Nature*, 461(7266):971–975.

Ramillien, G., Lombard, A., Cazenave, A., Ivins, E., Llubes, M., Remy, F., and Biancale, R. (2006). Interannual variations of the mass balance of the Antarctica and Greenland ice sheets from GRACE. *Global Planet. Change*, 53(3):198–208.

Rasmussen, S. O. and Elbrønd Hansen, N. (2008). ISKERNER–vindue til fortidens klima: Naturvidenskab for alle.

Rignot, E., Braaten, D., Gogineni, S. P., Krabill, W. B., and McConnell, J. R. (2004). Rapid ice discharge from southeast Greenland glaciers. *Geophys. Res. Lett.*, 31(10):L10401.

Rignot, E. and Kanagaratnam, P. (2006). Changes in the Velocity Structure of the Greenland Ice Sheet. *Science*, 311(5763):986–990.

Rignot, E., Koppes, M., and Velicogna, I. (2010). Rapid submarine melting of the calving faces of West Greenland glaciers. *Nat. Geosci.*, 3(3):187–191.

Riva, R., Gunter, B., Urban, T., Vermeersen, B., Lindenbergh, R., Helsen, M., Bamber, J., van de Wal, R., van den Broeke, M., and Schutz, B. (2009). Glacial isostatic adjustment over Antarctica from combined ICESat and GRACE satellite data. *Earth and planetary science letters*, 288(3-4):516–523.

Sasgen, I. (2009). *Present-day ice-mass change and glacial-isostatic adjustment in the polar regions from satellite gravimetry and geophysical modelling*. PhD thesis, Freien Universitat Berlin.

Sasgen, I., Martinec, Z., and Bamber, J. (2010). Combined GRACE and InSAR estimate of West Antarctic ice-mass loss. *J. eophys. Res.*, 115(F4):F04010.

Sasgen, I., Martinec, Z., and Fleming, K. (2006). Wiener optimal filtering of GRACE data. *Studia Geophysica et Geodaetica*, 50(4):499–508.

Schmidt, R., Flechtner, F., König, R., Meyer, U., Neumayer, K., Reigber, C., Rothacher, M., Petrovic, S., Zhu, S., and Güntner, A. (2007). GRACE time-variable gravity accuracy assessment. In *Dynamic Planet*, pages 237–243. Proceedings of International Association of Geodesy Symposia 130.

Schutz, B. E. (2002). Laser footprint location (geolocation) and surface profiles. *Algorithm Theoretical Basis Document*.

Schutz, B. E., Zwally, H. J., Shuman, C., Hancock, D., and DiMarzio, J. P. (2005). Overview of the ICESat mission. *Geophys. Res. Lett*, 32:21.

Shepherd, A. and Wingham, D. (2007). Recent Sea-Level Contributions of the Antarctic and Greenland Ice Sheets. *Science*, pages 1529–1532.

Shum, C., Kuo, C., and Guo, J. (2008). Role of Antarctic ice mass balance in present-day sea-level change. *Polar Science*, 2(2):149–161.

Slobbe, D. C., Ditmar, P., and Lindenbergh, R. C. (2009). Estimating the rates of mass change, ice volume change and snow volume change in Greenland from ICESat and GRACE data. *Geophys. J. Int.*, 176:95–106.

Slobbe, D. C., Lindenbergh, R. C., and Ditmar, P. (2008). Estimation of volume change rates of Greenland's ice sheet from ICESat data using overlapping footprints. *Remote Sens. Environ.*, 112(12):4204–4213.

Smith, B. E., Fricker, H. A., Joughin, I. R., and Tulaczyk, S. (2009). An inventory of active subglacial lakes in Antarctica detected by ICESat (2003-2008). *J. Glaciol.*, 55(192):L21S09.

Sole, A., Payne, T., Bamber, J., Nienow, P., and Krabill, W. (2008). Testing hypotheses of the cause of peripheral thinning of the Greenland Ice Sheet: is land-terminating ice thinning at anomalously high rates? *The Cryosphere*, 2(4):673–710.

Solomon, S., Qin, D., Manning, M., Chen, Z., Marquis, M., Averyt, K., Tignor, M., and Miller, H. (2007). *Climate change 2007: the physical science basis*. Cambridge University Press.

Sørensen, L. S. and Forsberg, R. (2010). Greenland Ice Sheet Mass Loss from GRACE Monthly Models. In Mertikas, S. P., editor, *Gravity, Geoid and Earth Observation*, pages 527–532. Proceedings of International Association of Geodesy Symposia 135.

Sørensen, L. S., Simonsen, S. B., Nielsen, K., Lucas-Picher, P., Spada, G., Adalgeirsdottir, G., Forsberg, R., and Hvidberg, C. S. (2010a). Mass balance of the Greenland Ice Sheet - A study of ICESat data, surface density and firn compaction modelling. *The cryosphere Discussions*, 4:2103–2141.

Sørensen, L. S., Stenseng, L., Simonsen, S. B., Forsberg, R., Poulsen, S. K., and Helm, V. (2010b). Greenland Ice Sheet changes from space using laser, radar and gravity. In *Proceedings of the ESA Living Planet Symposium, 28 June - 2 July*, pages SP–686. ESA Publication Division, Nordwijk, The Netherlands.

Spada, G. and Stocchi, P. (2006). *The Sea Level Equation - Theory and Numerical Examples*. Aracne.

Spada, G. and Stocchi, P. (2007). SELEN: a Fortran 90 program for solving the "Sea Level Equation". *Comput. Geosci.*, 33 (4):538–562.

Steffen, H., Denker, H., and Müller, J. (2008). Glacial isostatic adjustment in Fennoscandia from GRACE data and comparison with geodynamical models. *J. Geodyn.*, 46(3-5):155–164.

Swenson, S. and Wahr, J. (2006). Post-processing removal of correlated errors in GRACE data. *Geophys. Res. Lett.*, 33(8):L08402.

Tapley, B., Bettadpur, S., Watkins, M., and Reigber, C. (2004). The gravity recovery and climate experiment: Mission overview and early results. *Geophys. Res. Lett*, 31(9):L09607.

Tarasov, L. and Richard Peltier, W. (2002). Greenland glacial history and local geodynamic consequences. *Geophys. J. Int.*, 150:198–229.

Thomas, R., Davis, C., Frederick, E., Krabill, W., Li, Y., Manizade, S., and Martin, C. (2008). A comparison of Greenland ice-sheet volume changes derived from altimetry measurements. *J. Glaciol.*, 54:203–212.

Thomas, R., Frederick, E., Krabill, W., Manizade, S., and Martin, C. (2009). Recent changes on Greenland outlet glaciers. *J. Glaciol.*, 55:147–162.

Tscherning, C. C. (1985). Local approximation of the gravity potential by least squares collocation. In *Proceedings of the International Summer School on Local Gravity Field Approximation, Beijing, China, Aug*, pages 277–362.

Tscherning, C. C., Arabelos, D., and Strykowski, G. (2001). The 1-cm geoid after GOCE. In *The IAG Symposia*, volume 123, pages 267–270.

Tscherning, C. C., Forsberg, R., and Knudsen, P. (1992). The GRAVSOFT package for geoid determination. In *Proc. 1. Continental Workshop on the Geoid in Europe, Prague*, pages 327–334.

Tushingham, A. M. and Peltier, W. R. (1991). ICE-3G: A new global model of Late Pleistocene deglaciation based upon geophysical predictions of post-glacial relative sea level change. *J. Geophys. Res.*, 96(B3):4497–4523.

van den Broeke, M., Bamber, J., Ettema, J., Rignot, E., Schrama, E., van de Berg, W. J., van Meijgaard, E., Velicogna, I., and Wouters, B. (2009). Partitioning Recent Greenland Mass Loss. *Science*, 326(5955):984–986.

Velicogna, I. (2009). Increasing rates of ice mass loss from the Greenland and Antarctic ice sheets revealed by GRACE. *Geophys. Res. Lett.*, 36(19):L19503.

Velicogna, I. and Wahr, J. (2005). Greenland mass balance from GRACE. *Geophys. Res. Lett.*, 32(18):L18505.

Wahr, J., Molenaar, M., and Bryan, F. (1998). Time variability of the Earth's gravity field: Hydrological and oceanic effects and their possible detection using GRACE. *J. Geophys. Res.*, 103:30–30.

Wahr, J., Swenson, S., and Velicogna, I. (2006). Accuracy of GRACE mass estimates. *Geophys. Res. Lett*, 33(6).

Wahr, J. and Velicogna, I. (2003). What might GRACE contribute to studies of post glacial rebound? *Space Science Reviews*, 108(1):319–330.

Wahr, J., Wingham, D., and Bentley, C. (2000). A method of combining ICESat and GRACE satellite data to constrain Antarctic mass balance. *J. Geophys. Res.*, 105(B7):16279.

Watkins, M. M. (2007). JPL level-2 processing standards document for level-2 product release 04. GRACE 327-744. Technical report, Jet Propulsion Laboratory, Pasadena.

Weidick, A. (1996). Neoglacial changes of ice cover and sea level in Greenland - a classical enigma. *The Palaeo-Eskimo Cultures of Greenland: New Perspectives in Greenlandic Archaeology*, pages 257–270.

Whitehouse, P. (2009). Glacial isostatic adjustment - State of the art report. Technical Report TR-09-11, Durham University.

Wouters, B., Chambers, D., and Schrama, E. J. O. (2008). GRACE observes small-scale mass loss in Greenland. *Geophys. Res. Lett.*, 35(20):L20501.

Wu, X., Heflin, M., Schotman, H., Vermeersen, B., Dong, D., Gross, R., Ivins, E., Moore, A., and Owen, S. (2010). Simultaneous estimation of global present-day water transport and glacial isostatic adjustment. *Nat. Geosci.*, 3(9):642–646.

Zwally, H. J., Abdalati, W., Herring, T., Larson, K., Saba, J., and Steffen, K. (2002a). Surface Melt-Induced Acceleration of Greenland Ice-Sheet Flow. *Science*, 297:218–222.

Zwally, H. J., Schutz, B., Abdalati, W., Abshire, J., Bentley, C., Brenner, A., Bufton, J., Dezio, J., Hancock, D., Harding, D., et al. (2002b). ICESat's laser measurements of polar ice, atmosphere, ocean, and land. *J. Geodyn.*, 34(3-4):405–445.

Zwally, H. J., Schutz, R., Bentley, C., Bufton, J., Herring, T., Minster, J., Spinhirne, J., and Thomas, R. (2010). GLAS/ICESat L2 Antarctic and Greenland Ice Sheet Altimetry Data V031. *http://nsidc.org/data/gla12.html*, Accessed, Mar. 2010.

Appendix A

Paper 1

Sørensen, Louise Sandberg and Forsberg, R. (2010), *Greenland Ice Sheet Mass Loss from GRACE Monthly Models*, Gravity, Geoid and Earth Observation, vol. 135, pp. 527–532, doi:10.1007/978-3-642-10634-7_70. Sørensen and Forsberg (2010)

Chapter 70

Greenland Ice Sheet Mass Loss from GRACE Monthly Models

L. Sandberg Sørensen and R. Forsberg

Abstract The Greenland ice sheet is currently experiencing a net mass loss. There are however large discrepancies between the published qualitative mass loss estimates, based on different data sets and methods. There are even large differences between the results based on the same data sources, as is the case with those estimated from GRACE data.

In this chapter we have used a generalized inversion method to estimate the Greenland ice sheet mass change from the monthly global gravity solutions, provided by three different GRACE processing centers; CSR, JPL and GFZ.

In order to derive mass change from these monthly global gravity models, we first calculate the gravity trend from these. When isolating the gravity trend signal, which is caused by the ice mass change, we first subtract the signal produced by the postglacial rebound (PGR) in Greenland. This is done by a simple method based on the ice history model ICE-5G and on ground measurements made in Scandinavia. We find that the PGR signal corresponds to a mass change signal of approximately –4 Gt per year.

We conclude that there are large differences between these estimated mass change models. We find a total mass loss of 189, 146 and 67 Gt/year based on the CSR, GFZ and JPL solution respectively.

L.S. Sørensen (✉)
Department of Geodynamics, National Space Institute, DTU-Space, Copenhagen Ø DK-2100, Denmark
e-mail: slss@space.dtu.dk

70.1 Introduction

The Greenland ice sheet mass change is currently a hot topic. The IPCC report from 2007 stated that the response of the Greenland ice sheet to the observed climate changes is very poorly understood (Solomon et al., 2007). Much research has been done in order to improve our knowledge of the ice sheet, and in particular in estimating the mass loss of the ice sheet and hence the resulting sea level rise.

In recent years, many research groups have published Greenland ice sheet mass loss estimates, based on different data sets and methods (Chen et al., 2006; Rignot and Kanagaratnam, 2006; Veligcogna and Wahr, 2006; Luthcke et al., 2006).

It is clear though, that there is poor agreement between these estimates, which indicates that there are large differences in the way to handle the data. Even published results based on data solely from the Gravity Recovery and Climate Experiment (GRACE) are not all in agreement (Velicogna and Wahr, 2006; Luthcke et al., 2006; Wouters et al., 2008). Some of the published GRACE mass change estimates are listed in Table 70.1.

Table 70.1 Ice mass change estimates of the Greenland Ice Sheet by different authors, using different GRACE data time spans and methods

Authors	Time span	Mass change
Chen et al. (2006)	2002–2005	–219 ± 21 Gt/year
Luthcke et al. (2006)	2003–2005	–101 ± 16 Gt/year
Velicogna and Wahr (2006)	2002–2006	–227 ± 33 Gt/year
Wouters et al. (2008)	2003–2008	–179 ± 25 Gt/year

S.P. Mertikas (ed.), *Gravity, Geoid and Earth Observation*, International Association of Geodesy Symposia 135,
DOI 10.1007/978-3-642-10634-7_70,

This problem will be addressed in this paper, where we estimate the mass loss from monthly global gravity models derived from GRACE data using a new method.

The data used in this investigation are the monthly GRACE solutions provided by the three processing centers CSR, GFZ and JPL.

70.2 Data and Methods

The GRACE data consists of monthly spherical harmonic expansions of the Earth's gravity potential (GRACE Level-2 data). They are provided by the three processing centers CSR (Center for Space Research, University of Texas, USA), JPL (Jet Propulsion Laboratories, California, USA) and GFZ (now Helmholtz-Centre Potsdam GFZ, Germany). These solutions are represented by a set of Stokes harmonic coefficients up to a defined degree and order (Bettadpur, 2007).

We use the release 4 data sets (for JPL release 4.1), which are the latest public available data sets. The data sets are shortly described in Table 70.2. In this study we use the 68 epochs which are available from all three centers. Hence, the data time span is from 08-2002 to 08-2008, but with the months 09-2002, 12-2002, 01-2003, 06-2003, and 01-2004 missing. We have filtered the data by truncating all of the spherical harmonic expansions at degree and order 40, to limit the errors introduced to the GRACE data by the higher order coefficients.

With the new method, described in this paper, the gravity disturbance trends are stacked data, which strongly reduces noise. Hence it is not necessary to do any "de-striping" or filtering.

Table 70.2 Description of the available data sets. For all three data sets, the months June–July 2002 and June 2003 are missing due to missing accelerometer data. $(n,m)_{max}$ is the maximum degree and order of the spherical harmonic expansions as delivered by the processing centers

	CSR	GFZ	JPL
Release	04	04	04.1
Epochs	75	69	72
Start	04-2002	08-2002	04-2002
End	09-2008	09-2008	08-2008
$(n,m)_{max}$	60	120	120

70.2.1 Gravity Disturbance Trend

The ice mass change of the Greenland ice sheet, will be estimated from the gravity trend in the area. The first step is therefore to determine the change of the monthly gravity fields, δg, in time, which is done by a 4-parameter trend analysis of the gravity disturbances. A bias, trend and two seasonal terms are estimated in each grid cell of size 0.5° × 0.5° (1).

$$\delta g\,(t) = a + bt + c\,\cos(2\pi t) + d\,\sin(2\pi t)\,, \quad (1)$$

where t is given in decimal years. The resulting gravity trends at satellite altitude (500 km), based on the CSR, JPL and GFZ epochs respectively, are shown in Fig. 70.1.

There are clear differences between these gravity trends, but they do agree on a strong negative trend over southeast Greenland, indicating a mass loss in this region.

70.2.2 Post-Glacial Rebound

Postglacial rebound (PGR) is the viscoelastic response of the Earth as a result of the glacial unloading since the last glacial maximum. Some of the observed gravity trend originates from the PGR.

The gravity trend generated by the postglacial rebound must be subtracted from the observed gravity trend, in order to isolate the gravity trend signal from the ice mass change.

There is much debate on how to determine the PGR signal, and different approaches and models are used (Barletta et al., 2008; Velicogna et al., 2006). There are large uncertainties in both the Earth models and the ice history models used.

Due to the significant uncertainty in the Earth models, we choose to correct for the PGR gravity signal in a more empirical way. The uplift in Greenland, according to the ICE-5G model (Peltier, 2004), is shown in Fig. 70.2.

In order to convert the uplift model into a gravity trend, we assume a linear relationship (2) between height change, dh, and gravity change, dg, as found in Scandinavia 1965–2002 (Routsalainen, 2002)

$$dg = 0.23\left[\frac{\mu gal}{mm}\right] dh \quad (2)$$

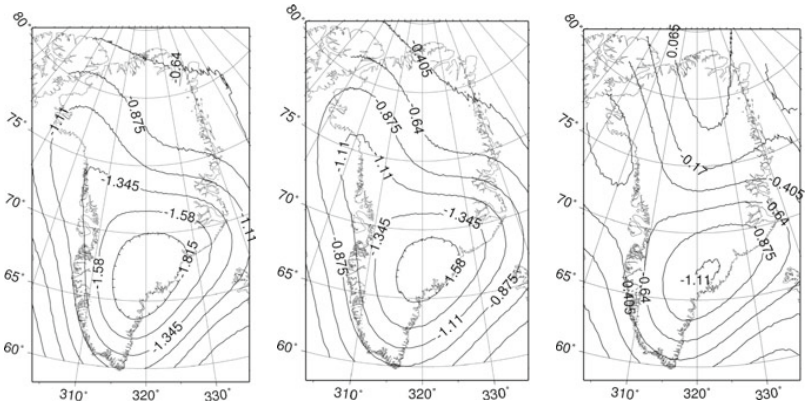

Fig. 70.1 Gravity trends at satellite altitude (500 km), given in μgal per year, based on (**a**) CSR-RL04, (**b**) GFZ-RL04 and (**c**) JPL-RL04.1 epochs. The large differences are apparent

The gravity change include the height change effect and the free air gradient is therefore subtracted.

The ICE-5G uplift is converted into a gravity signal at ground level, and upward continued to satellite altitude, where it is subtracted from the GRACE gravity disturbance trend.

The total PGR signal, found by this method, corresponds to a gravity trend generated by a mass loss of approximately 4 Gt per year, which agrees well with the PGR estimates from Velicogna and Wahr (2005).

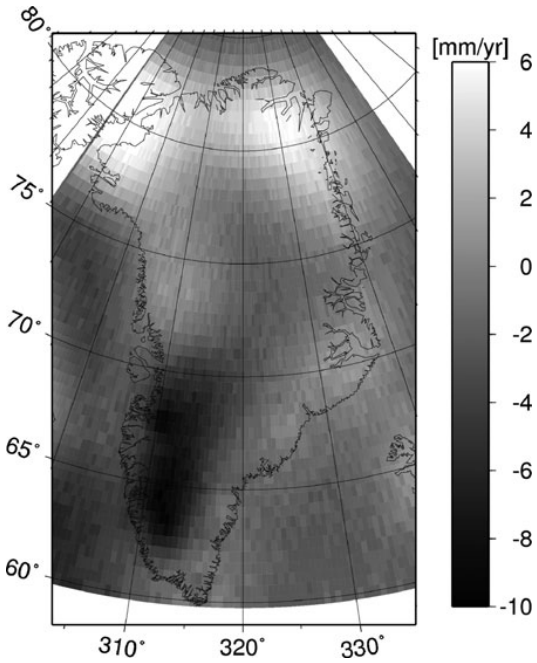

Fig. 70.2 Uplift in Greenland [mm/year] based on the ICE-5G ice history model

70.2.3 Inversion Method

We use a generalized inversion method to derive mass change estimates from gravity trends. This can be stated as a linear problem (3), with the response matrix **A**.

The observation vector, **y** (4) consists of the gravity trends at satellite altitude, defined in a grid covering the area in which the gravity trend is shown, see Fig. 70.1.

The model parameter vector, **x** (5) contains the point mass changes, and these will be solved for in a grid defined by the ice covered area of Greenland. This solution domain is shown in red in Fig. 70.3.

The relationship between the gravity trend and the mass points are given by (6) (Heiskanen and Moritz, 1967), where R is the Earth radius, r is the distance from the Earth center to the satellite and ψ is the spherical distance.

The problem is solved by using Tychonov generalized inversion with regularization λ (7).

$$\bar{y} = \underline{\underline{A}}\,\bar{x} \tag{3}$$

$$\bar{y} = \frac{\delta g_i}{\delta t}, \quad i = 1, \ldots, n \tag{4}$$

$$\bar{x} = \frac{\delta m_j}{\delta t}, \quad j = 1, \ldots, m \tag{5}$$

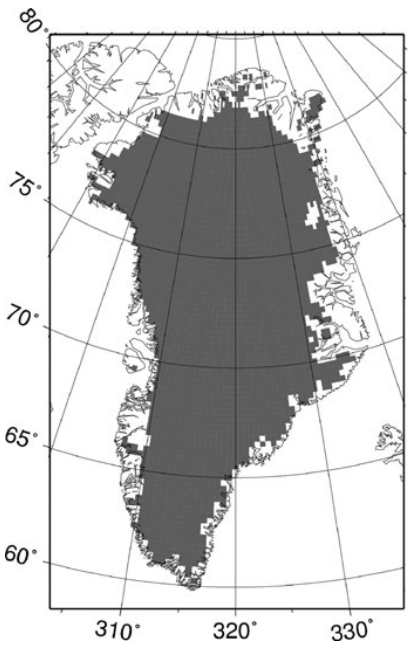

Fig. 70.3 The marked area is the solution domain for the inversion. In this grid, the point masses will be estimated

$$\delta g_i = \sum_j \left\{ \frac{G\delta m_j \left(R^2 r - R^3 \cos\Psi_{ij}\right)}{\left(r^2 + R^2 - 2Rr\cos\Psi_{ij}\right)^{3/2}} \right\} \quad (6)$$

$$\bar{x} = \left[\underline{\underline{A}}^T \underline{\underline{A}} + \lambda \underline{\underline{I}}\right]^{-1} \underline{\underline{A}}^T y \quad (7)$$

The elastic uplift of the Earth, due to the present day unloading, generates a gravity change. This gravity change has not been taken into account in this study.

An estimate of the total mass change of the ice sheet is then found by summation of all the point mass changes, using point masses located only within the area of the ice sheet.

Because the inversion is an improperly posed problem, there is a strong correlation between the regularization parameter λ, and the resolution in parameter space. However, the total mass change remains nearly constant over a wide range of λ-values.

When deriving the mass change models, we use data of the observed gravity trend in an area that extend outside Greenland (the area is shown in Fig. 70.1). This means that our result can be biased by other mass change sources outside Greenland, such as for example the ice caps on Svalbard and Iceland, or changes in sea level. Such masses are easily included in the estimation scheme, and we found the aliasing effect of these small ice caps to be negligible for Greenland.

70.3 Mass Change Results

We derive three mass change models of the Greenland ice sheet, using the inversion method on the gravity trends (with PGR signal subtracted) over Greenland, as described above. These results are presented in Fig. 70.4, and are derived from CSR, JPL and GFZ gravity epochs respectively.

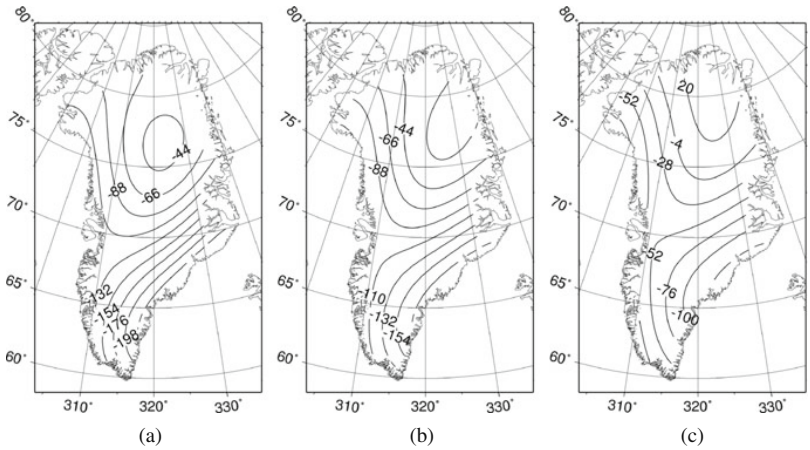

Fig. 70.4 Models of mass change in Greenland, given in mm equivalent water height per year, based on (**a**) CSR-RL04, (**b**) GFZ-RL04 and (**c**) JPL-RL04.1 epochs. We use here a regularization parameter which gives a relatively poor spatial resolution

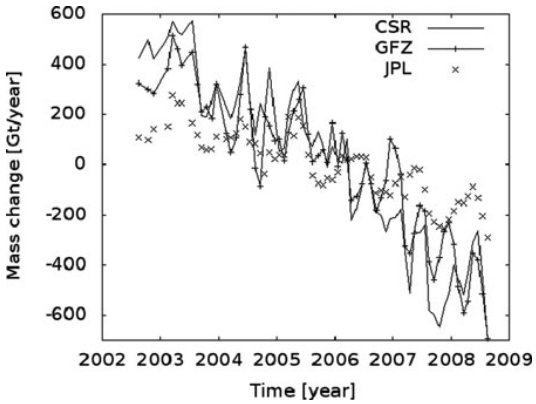

Fig. 70.5 Monthly mass change estimates for the Greenland Ice Sheet, given in Gt, from CSR-RL04, GFZ-RL04 and JPL-RL04.1 epochs

It is clear from Fig. 70.4, that the mass change models are significantly different in magnitude, but that the overall trend in the models are similar, represented by a mass loss near the ice edge and a mass gain in the central northern part of the ice sheet.

The total annual mass changes are found by summing up all of the mass points in the models, and they are found to be;

- 189 Gt/year based on CSR-RL04
- 146 Gt/year based on GFZ-RL04 and
- 67 Gt/year based on JPL-RL04.1 epochs.

The mass change derived from each monthly gravity field is shown in Fig. 70.5.

70.4 Conclusion

In this paper we show that significantly different mass loss results are obtained, when using GRACE epochs from the three different processing centers. We find mass change estimates of –189 Gt/year from CSR, –146 Gt/year from GFZ and –67 Gt/year from JPL data.

Even though the total mass loss estimates are very different, the same pattern is seen in the three mass change models (Fig. 70.4). There is a clear trend, that the mass loss is strongest near the ice edge, and the largest mass loss is found in southeast Greenland. This pattern is in good agreement with other observations (Rignot et al., 2004; Howat et al., 2007; Krabill et al., 2004).

As mentioned, we have neglected the gravity change due to present day elastic uplift in this study, which introduces an error in the mass change estimates. The choice is justified by the fact that the focus of this study is on the comparison between the 3 centers monthly solutions, rather than on the absolute mass change estimates. The elastic uplift signal will be implemented in future studies.

The large differences in mass change estimates, based on data sets from different processing centers, indicate that the GRACE data processing has not yet been fully exploited.

Acknowledgements The GRACE data were provided through the NASA-JPL PODAAC system.

We thank the two anonymous reviewers for their comments, which improved the manuscript.

References

Barletta, V.R., R. Sabadini, and A. Bordoni (2008). Isolating the PGR signal in the GRACE data: impact on mass balance estimates in Antarctica and Greenland. In:*Geophys. J. Int.,* doi:10.1111/j.1365-246X.2007.03630.x].

Bettadpur, S. (2007). Level-2 gravity field product user handbook (Rev 2.3), Center for Space Research, The University of Texas at Austin, February 20.

Chen, J.L., C.R. Wilson, and B.D. Tapley (2006). Satellite gravity measurements confirm accelerated melting of Greenland ice sheet. In: *Science,* doi: 10.1126/science.1129007.

Heiskanen, W.A. and H. Moritz (1967). Physical geodesy. Freeman and Co*,* San Francisco.

Howat, I.M., I. Joughin, and T.A. Scambos (2007). Rapid changes in ice discharge from Greenland Outlet Glaciers. In: *Science*, doi:10.1126/science.1138478.

Krabill, W., E. Hanna, P. Huybrechts, W. Abdalati, J. Cappelen, B. Csatho, E. Frederick, S. Manizade, C. Martin, J. Sonntag, R. Swift, R. Thomas, and J. Yungel (2004). Greenland Ice Sheet: Increased coastal thinning. In: *Geophys. Res. Lett.*, doi:10.1029/2004GL021533.

Luthcke, S.B., H.J. Zwally, W. Abdalati, D.D. Rowlands, R.D. Ray, R.S. Nerem, F.G. Lemoine, J.J. McCarthy, and D.S. Chinn (2006). Recent Greenland ice mass loss by drainage system from satellite gravity observations. In: *Science.* doi: 10.1126/science.1130776.

Peltier, W.R. (2004) Global glacial isostasy and the surface of the ice-age earth: the ice-5G (VM2) model and GRACE. In: *Annu. Rev. Earth Planet. Sci.* 32. 111–149.

Rignot, E., D. Braaten, S.P. Gogineni, W.B. Krabill, and J.R. McConnell (2004). Rapid ice discharge from southeast

Greenland glaciers, In: *Geophys. Res. Lett.*, doi:10.1029/2004GL019474.

Rignot, E. and P. Kanagaratnam (2006). Changes in the velocity structure of the Greenland ice sheet. In: *Science*, doi: 10.1126/science.1121381.

Ruotsalainen, H. (2002), The Fennoscandian land uplift gravity lines – a tool for the Nordic geodynamical studies. In: *Proceedings of 14th general meeting of the Nordic Geodetic Commission*, Espoo, Finland, 2002, pp. 107–110.

Solomon, S. D. Qin, M. Manning, Z. Chen, M. Marquis, K.B. Averyt, M. Tignor and H.L. Miller (2007). IPCC Summary for Policymakers. In: *Climate Change 2007: The Physical Science Basis*. Cambridge University Press, Cambridge, United Kingdom and New York, NY, USA.

Velicogna, I. and J. Wahr (2005). Greenland mass balance from GRACE. In: *Geophys. Res. Lett.*, doi: 10.1029/2005GL023955.

Veligcogna, I. and J. Wahr (2006). Acceleration of Greenland ice mass loss in spring 2004. In: *Nature*, doi:10.1038/nature05168.

Wouters, B., D. Chambers, and E.J.O. Schrama (2008). GRACE observes small-scale mass loss in Greenland. In: *Geoph. Res. Lett.*, doi: 10.1029/2008GL034816.

Appendix B

Paper 2

Sørensen, Louise Sandberg, Simonsen, S. B., Nielsen, K., Lucas-Picher, P., Spada, G., Adalgeirsdottir, G., Forsberg, R. and Hvidberg, C. S. (2010), *Mass balance of the Greenland ice sheet - A study of ICESat data, surface density and firn compaction modelling*, under review in The Cryosphere Discussions. Sørensen et al. (2010a)
Available at : http://www.the-cryosphere-discuss.net/4/2103/2010/tcd-4-2103-2010.pdf

The Cryosphere Discuss., 4, 2103–2141, 2010
www.the-cryosphere-discuss.net/4/2103/2010/
doi:10.5194/tcd-4-2103-2010

The Cryosphere Discussions

Mass balance of the Greenland ice sheet – a study of ICESat data, surface density and firn compaction modelling

L. S. Sørensen[1,2,*], S. B. Simonsen[3,4,*], K. Nielsen[5], P. Lucas-Picher[4], G. Spada[6], G. Adalgeirsdottir[4], R. Forsberg[1], and C. S. Hvidberg[3]

[1]Geodynamics Department, DTU Space, Juliane Maries vej 30, 2100 Copenhagen, Denmark
[2]Planet and Geophysics, NBI, University of Copenhagen, Juliane Maries Vej 30, 2100 Copenhagen, Denmark
[3]Centre for Ice and Climate, NBI, University of Copenhagen, Juliane Maries Vej 30, 2100 Copenhagen, Denmark
[4]Danish Climate Centre, DMI, Lyngbyvej 100, 2100 Copenhagen, Denmark
[5]Geodesy Department, DTU Space, Juliane Maries vej 30, 2100 Copenhagen, Denmark

[6]Dept. of Mathematics, Informatics, Physics, and Chemistry, Urbino University "Carlo Bo", Via Santa Chiara, 27, 61029 Urbino (PU), Italy
*These authors contributed equally to this work.

Received: 20 September 2010 – Accepted: 29 September 2010 – Published: 15 October 2010

Correspondence to: L. S. Sørensen (slss@space.dtu.dk)
and S. B. Simonsen (sbs@nbi.ku.dk)

Published by Copernicus Publications on behalf of the European Geosciences Union.

Abstract

ICESat has provided surface elevation measurements of the ice sheets since the launch in January 2003, resulting in a unique data set for monitoring the changes of the cryosphere. Here we present a novel method for determining the mass balance of the Greenland ice sheet derived from ICESat altimetry data.

Four different methods for deriving the elevation changes from the ICESat altimetry data set are used. This multi method approach gives an understanding of the complexity associated with deriving elevation changes from the ICESat altimetry data set.

The altimetry can not stand alone in estimating the mass balance of the Greenland ice sheet. We find firn dynamics and surface densities to be important factors in deriving the mass loss from remote sensing altimetry. The volume change derived from ICESat data is corrected for firn compaction, vertical bedrock movement and an intercampaign elevation bias in the ICESat data. Subsequently, the corrected volume change is converted into mass change by surface density modelling. The firn compaction and density models are driven by a dynamically downscaled simulation of the HIRHAM5 regional climate model using ERA-Interim reanalysis lateral boundary conditions.

We find an annual mass loss of the Greenland ice sheet of $210 \pm 21\,\mathrm{Gt\,yr^{-1}}$ in the period from October 2003 to March 2008. This result is in good agreement with other studies of the Greenland ice sheet mass balance, based on different remote sensing techniques.

1 Introduction

Different satellite based measuring techniques have been used to observe the present-day changes of the Greenland ice sheet (GrIS). Synthetic Aperture Radar (SAR) imaging reveals an acceleration of a large number of outlet glaciers in Greenland (Abdalati et al., 2001; Rignot et al., 2004; Rignot and Kanagaratnam, 2006; Joughin et al., 2010).

Gravity changes observed by the Gravity Recovery And Climate Experiment (GRACE) show a significant mass loss (Velicogna and Wahr, 2005; Luthcke et al., 2006; Wouters et al., 2008; Sørensen and Forsberg, 2010; Wu et al., 2010). Local elevation changes of the GrIS with significant thinning along the ice margin are revealed by laser altimetry (Slobbe et al., 2008; Howat et al., 2008; Pritchard et al., 2009).

We provide a novel mass balance estimate of the GrIS for the period 2003–2008, derived from elevation measurements from NASA's Ice, Cloud, and land Elevation Satellite (ICESat), firn compaction and surface density modelling.

Different methods have been used to derive secular surface elevation change estimates $\left(\frac{\mathrm{d}H}{\mathrm{d}t}\right)$ of snow or ice covered areas from ICESat data (Fricker and Padman, 2006; Howat et al., 2008; Slobbe et al., 2008; Pritchard et al., 2009). Here we use four different methods to derive $\frac{\mathrm{d}H}{\mathrm{d}t}$, and the differences are investigated.

The total volume change of the GrIS is found by fitting a smooth surface, which covers the entire ice sheet, to the ICESat derived $\frac{\mathrm{d}H}{\mathrm{d}t}$ estimates. The conversion of the derived $\frac{\mathrm{d}H}{\mathrm{d}t}$ values to mass changes is based on firn compaction and surface density modelling, forced by climate parameters from a regional climate model (RCM). Other studies have linked climate models and surface mass balance models in order to estimate the mass balance of the GrIS (Li et al., 2007; van den Broeke et al., 2009), but in our approach we directly use the estimated $\frac{\mathrm{d}H}{\mathrm{d}t}$ values from ICESat to derive the total mass balance including firn dynamics, driven by the HIRHAM5 high resolution RCM. The HIRHAM5 simulation is a dynamical downscaling of the ECMWF ERA-Interim reanalysis (Sect. 5.2).

The first part of this paper is dedicated to the description of the ICESat data and the methods used for deriving elevation and volume changes of the GrIS (Sects. 2 to 3). The volume change estimates and their associated uncertainties are presented in Sect. 4.

In the second part of this paper, the volume to mass conversion is described (Sects. 5 to 7). This includes the changes in the firn compaction and surface density of the GrIS. The theoretical treatment of the firn dynamics involved in elevation changes without

contributing to the mass balance of the GrIS is presented in Sect. 5. The findings from both observations and model treatment are combined to derive the total mass balance of the GrIS in Sect. 7.

2 ICESat data

ICESat carries the Geoscience Laser Altimeter System (GLAS) instrument (Abshire et al., 2005). Technical problems with the GLAS instrument early in the mission have resulted in a significant reduction in repeated tracks, and hence in spatial resolution. Successive tracks are separated by approximately 30 km in the southern part of Greenland, because the GLAS instrument has been operating only 2–3 months per year.

The GLAS/ICESat Antarctic and Greenland Ice Sheet Altimetry Data product (GLA12) (Zwally et al., 2010) was downloaded from the National Snow and Ice Data Center. This level-2 altimetry product provides geolocated and time tagged ice sheet surface elevation estimates, with respect to the TOPEX/Poseidon reference ellipsoid. The satellite laser footprint size is 30–70 m and the distance between the footprint centers is approximately 170 m. This study is based on the 91-day repeat cycle ICESat data (release 31) from October 2003 to March 2008. The time span and release number of the laser campaigns in the data set are listed in Table 1.

2.1 ICESat data pre-processing

A procedure of data culling and application of corrections is necessary to reduce some of the systematic errors in the ICESat data set, and to remove problematic measurements (Smith et al., 2005). Saturation of the waveform can induce errors in surface elevation estimates (Fricker et al., 2005). Applying the saturation correction to the relevant measurements, which are flagged in the data files, reduces these errors (NSIDC, 2010). We have also used the difference between the shape of the return signal and a Gaussian fit (the IceSvar parameter), to evaluate data. Large differences indicate

less reliable surface elevation estimates, and measurements for which the misfit is large (IceSvar $\geq$ 0.04 V) are rejected from the further analysis. Multiple peaks can be caused by reflections from clouds. All measurements that contain more than one peak in the return signal are rejected from the analysis. Besides these two criteria, we have also used data quality flags and warnings given with the data to reject problematic measurements. We find that these thresholds result in a satisfactory size of crossover error.

Only measurements from the GrIS and the surrounding glaciers and ice caps are considered in the elevation change analysis. The total number of ICESat measurements from the ice covered areas is 10 367 807. After rejecting problematic measurements in the data culling procedure, the number is reduced by approximately 13% to 9 053 639. The details are listed in in Table 1.

3 Methods for deriving surface elevation changes

The individual ICESat tracks are not precisely repeated but can be up to several hundred meters apart. Thus the observed elevation difference between tracks contains contributions from terrain, seasonal variations and secular trends.

The fact that the ICESat tracks are not exactly repeated, complicates the methods for deriving $\frac{dH}{dt}$ along-track, due to the presence of a cross-track slope, caused by the topography. The cross-track slope must be determined and subtracted in order to derive the actual elevation change. Several methods for doing this have previously been published (Fricker and Padman, 2006; Howat et al., 2008; Slobbe et al., 2008; Pritchard et al., 2009). We present $\frac{dH}{dt}$ results obtained by using four different methods (M1–M4). The methods have different strengths and weaknesses, which become apparent when comparing the results. M1–M3 are along-track analysis and are all set up to estimate $\frac{dH}{dt}$ at a 500 m along-track resolution. M4 is a crossover analysis, and hence the spatial resolution obtained by this method is lower. An observed elevation difference between tracks will also include a seasonal signal, caused by variations in accumulation, flow

and melt during the year. In all four approaches we solve for both a secular trend $\frac{dH}{dt}$ and a seasonal signal, $s(t)$. Hence, the time dependent surface elevation, $\tilde{H}(t)$, is parameterised as:

$$\tilde{H}(t) = \left(\frac{dH}{dt}\right) t + s(t), \quad (1)$$

where the seasonal signal is given by:

$$s(t) = D\cos\left(\frac{2\pi}{T}t + \phi\right) = \alpha\cos(\omega t) + \beta\sin(\omega t), \quad (2)$$

with amplitude $D = \sqrt{\alpha^2 + \beta^2}$, period T (365 days), and a phase ϕ.

Each of the $\frac{dH}{dt}$ estimates from the four methods are associated with a variance from the regression procedure applied. $\frac{dH}{dt}$ values associated with a large variance are not used in the mass balance calculation.

3.1 Method 1

In principle, a Digital Elevation Model (DEM) could be used to correct for the surface slope, and this approach is used in the first method (M1). Unfortunately there are no independent, sufficiently accurate high resolution DEM's available which cover the entire GrIS. Following Slobbe et al. (2008), we choose the DEM generated from the first campaigns of ICESat data (DiMarzio et al., 2007). The grid spacing of this DEM is 1 km and the elevations are given relative to the WGS 84 ellipsoid.

In order to subtract the DEM from the ICESat data, the DEM is linearly interpolated to estimate the value in each data location. The height of each ICESat measurement above the reference DEM is given by:

$$\Delta H^{M1} = H^{ICESat} - H^{DEM}, \quad (3)$$

where H^{ICESat} is translated into elevations above the WGS84 ellipsoid, to be comparable with the DEM elevations (H^{DEM}).

The measurements are catagorized according to the ICESat track (i) and 500 m along-track segment denoted j. The mean of the ΔH^{M1} values of each ICESat campaigns is calculated in each segment, creating time series of $\Delta\bar{H}^{M1}$ values along-track.

$$\Delta\bar{H}^{M1}_{ij} = \begin{pmatrix} A_{ij} \\ B_{ij} \\ \alpha_{ij} \\ \beta_{ij} \end{pmatrix} \left(\bar{t}, 1, \cos\omega t, \sin\omega t\right), \quad (4)$$

where $A_{ij} = \left(\frac{dH}{dt}\right)_{ij}$, B_{ij} is the offset between the DEM and the ICESat elevations in the segment, and $\bar{t}$ is the mean time of a campaign in a given segment.

The governing equation, Eq. (4) is solved using ordinary least squares regression.

Only the long wavelength component of the terrain slope is removed, due to the relative low resolution of the DEM, compared to the spacing of the ICESat along-track measurements. The 1 km resolution is too low to capture the true topography in some areas, and this will most likely be reflected in the elevation changes calculated using this method.

3.2 Method 2

The second method (M2) is similar to the one presented by Pritchard et al. (2009). In each of the along-track segments, a reference surface is created from elevation measurements from two ICESat campaigns. The reference surface is represented by a centroid point (x_0, y_0, H_0) and slopes $\left(\frac{dH}{dx}, \frac{dH}{dy}\right)$. The choice of the two campaigns which are used to generate the reference surface is based on two criteria. The first criterium is that the two campaigns are separated by one year in time. This ensures that both the seasonal signal and the actual change in elevation between the two are minimized. The second criterium is the ICESat tracks used to generate the reference surface, are the ones that span the largest area. These criteria help to ensure that the reference surface is representative of the surface slope. Hence, it is considered the

reference for all other ICESat measurements in a given along-track segment, similar to the use of a DEM in M1:

$$\Delta H^{\mathrm{M2}} = H^{\mathrm{ICESat}} - H^{\mathrm{ref}}, \tag{5}$$

The height of the reference surface in a point (x, y) is given by:

$$H_{ij}^{\mathrm{ref}} = \left(\frac{\mathrm{d}H}{\mathrm{d}x}\right)_{ij}(x - x_0) + \left(\frac{\mathrm{d}H}{\mathrm{d}y}\right)_{ij}(y - y_0) + H_0. \tag{6}$$

The approach of solving for $\frac{\mathrm{d}H}{\mathrm{d}t}$ is similar to Eq. (4).

In spite of the criteria used to select the ICESat campaigns from which the reference surface is generated, method M2 is sensitive to seasonal variations and actual elevation changes between the two campaigns chosen. The $\frac{\mathrm{d}H}{\mathrm{d}t}$ estimates will therefore be biased.

3.3 Method 3

The third method (M3) is similar to the one presented in Howat et al. (2008) and Smith et al. (2009). In each along-track segment, the surface elevation H^{M3} is assumed to vary linearly with position (x, y), time (t) and a sine and cosine term, describing the seasonal signal:

$$H_{ij}^{\mathrm{M3}} = \begin{pmatrix} A_{ij} \\ B_{ij} \\ \alpha_{ij} \\ \beta_{ij} \\ \left(\frac{\mathrm{d}H}{\mathrm{d}x}\right)_{ij} \\ \left(\frac{\mathrm{d}H}{\mathrm{d}y}\right)_{ij} \end{pmatrix} \left(\bar{t}, 1, \cos\omega t, \sin\omega t, (x - x_0), (y - y_0)\right), \tag{7}$$

where $A_{ij} = \left(\frac{\mathrm{d}H}{\mathrm{d}t}\right)_{ij}$, $\left(\frac{\mathrm{d}H}{\mathrm{d}x}\right)$ is the along-track slope, $\left(\frac{\mathrm{d}H}{\mathrm{d}y}\right)$ is the cross-track slope, and B_{ij} is an estimate of the topography underlying the elevation changes. (x_0, y_0) is the

centroid point of the area spanned by all of the measurements in the track segment. In each segment, a least squares linear regression is performed to estimate the elevation change.

This method is sensitive to track geometry, since the method assumes that the H dependence in x, y and t is independent. For certain track constellations this will certainly not be the case.

3.4 Method 4

In the fourth method (M4), elevation changes are estimated only at crossover locations. From the ICESat data set (2003–2008), we find 458 432 crossovers.

The surface elevation at a track crossover location is found by linear interpolation of the closest points on the two tracks, located at each side of the crossover. In order to secure a fair estimate of the elevation at the crossover, a crossover is rejected if the north-south distance between the two closest points are grater than 500 m. This rejection criterium results in a subset of approximately 266 701 crossovers accepted for further analysis.

In contrary to the other three methods M1–M3, the elevation change at the crossover locations only contains the seasonal signal and the actual change in elevation. The elevation change is estimated in the crossover location of track n and m by a simple least squares linear regression.

$$\Delta \boldsymbol{H}_{nm}^{\mathrm{M4}} = A_{nm}\Delta \boldsymbol{t}_{nm} + s_{nm}(t) + B_{nm}, \tag{8}$$

where $\Delta \boldsymbol{H}_{nm}^{\mathrm{M4}}$ contains the elevation differences between track n and m, and $\Delta \boldsymbol{t}_{nm}$ contains the corresponding time differences. $A_{nm} = \left(\frac{\mathrm{d}H}{\mathrm{d}t}\right)_{nm}$ is the estimated elevation change in the location of the crossover between track n and m, $s_{nm}(t)$ is the seasonal signal and B_{nm} is the offset.

The disadvantage of this method is the poor spatial coverage of elevation change results, especially in the southern part of Greenland.

3.5 Elevation change results

The elevation changes obtained by the four methods show that there is a good agreement between the patterns of elevation changes (see Fig. 1a–d). A distinct thinning of the ice sheet is generally found along the southeast and west coast, while a smaller but consistent thickening is found in the interior part of the ice sheet, which is in agreement with other altimetry studies (Abdalati et al., 2001; Thomas et al., 2008, 2009; Slobbe et al., 2008; Pritchard et al., 2009). On the more local scale, the thickening of Flade Isblink (81.4° N, 15.1° W) and Storstrømmen (77.1° N, 22.6° W) are identified by all methods.

A fixed threshold of $6\,m^2$ for the variance associated with the fit of the regression is applied, and the number of output values from each method is an indication of how well a given method performs. The number of $\frac{dH}{dt}$ estimates with variance below the threshold is 264 635 for M1, 257 241 for M2, 276 717 for M3, and 4457 for M4.

This result indicates that M3 is preferable, since the largest number of accepted output values is obtained with this method.

4 Deriving volume changes

In order to estimate the total annual volume change, a smooth surface is fitted through the $\frac{dH}{dt}$ estimates, which covers the entire ice sheet. For this purpose ordinary kriging is used. The uncertainty in the total volume change is quantified using a bootstrap method.

4.1 Interpolation of volume changes

The $\frac{dH}{dt}$ estimates are interpolated onto a 5×5 km grid, using ordinary kriging. For all 4 method results, an exponential variogram model with a practical range of 150 km has been used. The range and the choice of model are based on the experimental

variogram. Due to the large number of the $\frac{dH}{dt}$ estimates, local neighborhood kriging is used. Cross validation analysis is applied in order to determine the sufficient number of closest points to be used in the interpolation. In order to pass on the variances from the regression analysis, from which the elevation changes are determined, these have been added to the variogram model (Pebesma, 1996). The R package gstat has been used for the kriging procedure (Pebesma, 2004).

The estimated volume changes are summarized in Table 2. The estimates are of little significance without knowing their associated uncertainties. It is often difficult analytically to keep track of the error when different calculations have been performed on data, and therefore a bootstrap method (Davison and Hinkley, 2006) is used to quantify the uncertainty.

4.2 Bootstrapping

Bootstrap is a resampling method (Davison and Hinkley, 2006). The basic idea of this method can be explained by the following steps.

(1) Create a resample by drawing random samples with replacements from an original data set, where it is assumed that the observations are independent. In this way a new data set is obtained with the same length as the original data set.

(2) Estimate the wanted parameter from the resample, in this case the annual volume change.

(3) Repeat step 1 and 2 *N* times.

These estimates represents a distribution of the wanted parameter, from which information of the uncertainty can be obtained.

Here, the original data set is the set of $\frac{dH}{dt}$ estimates. For each method 1000 resamples are created, from which an error estimate can be found. For method M1, M2, and M3 a resample is made by sampling between entire tracks contrary to individual

$\frac{dH}{dt}$ values, since these are highly correlated along-track. In method M4 the $\frac{dH}{dt}$ values are independent at the crossover locations, hence a resample is made by sampling between the $\frac{dH}{dt}$ values.

4.3 Volume change results

The 1000 bootstrap resamples make up the distributions of the volume changes. For all methods these distributions are approximately normally distributed and centered around the point estimate of the volume change (see Fig. 2). Hence the 95% confidence interval of the volume change will be $\pm 2\sigma$, where σ is the standard deviation. The error estimates of the volume changes are summarized in Table 2.

There is a relatively large spread in the resulting volume changes. In order to determine which method gives the best estimate, the four methods must be reevaluated.

Method M4 gives the smallest volume change estimate of $-147 \pm 24\,\mathrm{km^3\,yr^{-1}}$. This was expected since the density of crossovers is clearly under-represented in the southern part of Greenland (see Fig. 1) where the largest thinning is found, and many of the outlet glaciers in these regions will then not be captured correctly. We believe that the volume estimate found from M2 of $-179 \pm 15\,\mathrm{km^3\,yr^{-1}}$ is also an under-estimation. It is likely that the reference surface, which is created in M2, contains an actual elevation change, and this will result in biased $\frac{dH}{dt}$ values. The fact that M2 most likely dampens the signal of areas with large elevation changes, is also reflected in the relatively low standard deviation of the bootstrap procedure. The volume change results from methods M1 and M3 are similar, with volume change estimates of $-225 \pm 23\,\mathrm{km^3\,yr^{-1}}$ and $-237 \pm 25\,\mathrm{km^3\,yr^{-1}}$, respectively. We find that a larger number of accepted $\frac{dH}{dt}$ are obtained from M3 than M1, see Sect. 3.5, and that the M1 estimates are associated with larger variances than those of M3. Furthermore, it is seen in Fig. 2 that the M1 distribution is wider than the M3 distribution.

From the above argumentation it is concluded that method M3 gives the most reliable estimate of the volume change.

5 Modelling firn compaction and surface densities

Firn compaction and surface density of the ice sheet must be taken into account, in order to relate the ICESat measurements of changes in surface elevation to mass changes. The firn compaction responds dynamically to changes in surface temperature and precipitation. This dynamic response will not contribute to the mass balance of the GrIS, and therefore it is subtracted from the observed elevation change before converting it into mass change.

In general the change in surface elevation can be parameterised by

$$\frac{\mathrm{d}H}{\mathrm{d}t} = \frac{\dot{b}}{\rho} + w_\mathrm{c} + w_\mathrm{ice} + \frac{\dot{b}_\mathrm{m}}{\rho} + w_\mathrm{br} - u_\mathrm{s}\frac{\mathrm{d}S}{\mathrm{d}x} - u_\mathrm{b}\frac{\mathrm{d}B}{\mathrm{d}x}, \tag{9}$$

where $\dot{b}$ is the surface mass balance, ρ is the density of the snow or ice, w_c is the vertical velocity of the surface due to the changes in firn compaction, in the following referred to as the firn compaction velocity. w_ice is the vertical velocity of the ice matrix, $\dot{b}_\mathrm{m}$ is the basal mass balance, w_br is the vertical velocity of the underlying bedrock associated with glacio-isostatic adjustment, u_s is the horizontal ice velocity of the surface, S, and u_b is the horizontal velocity of the ice at the bed B (Paterson, 2002; Zwally and Li, 2002; Helsen et al., 2008). A cartesian coordinate system with a vertical axis pointing upwards is used and we define accumulation positive and ablation negative. Changes in w_ice can be neglected over short time spans (Zwally and Li, 2002) and $\dot{b}_\mathrm{m}$, $u_\mathrm{s}\frac{\mathrm{d}S}{\mathrm{d}x}$ and $u_\mathrm{b}\frac{\mathrm{d}B}{\mathrm{d}x}$ are assumed to be constant. Thus, over the short time span of the ICESat measurement Eq. (9) can be used to express the rate of mass change of the GrIS, derived from observations of the elevation change,

$$\dot{b} = \left(\frac{\mathrm{d}H^\mathrm{ICESat}}{\mathrm{d}t} - w_\mathrm{c} - w_\mathrm{br}\right)\rho, \tag{10}$$

where $\frac{\mathrm{d}H^\mathrm{ICESat}}{\mathrm{d}t}$ is the estimated elevation change observed from ICESat altimetry. w_c

and ρ can only be estimated from models of the firn compaction and density and w_{br} is estimated in accordance to Sect. 6.1.

5.1 Firn compaction model

In order to estimate the effect of firn compaction on short time scales, a time-dependent densification model is needed. Following Reeh (2008), the time-dependent contribution to the elevation change from changes in firn compaction is the sum of annual firn layer anomalies with respect to a steady state reference. The steady state reference is defined as the youngest layer in the firn column which is unaffected by the inter-annual variability in the surface temperature and surface mass balance. The firn compaction velocity is then defined as

$$w_{\mathrm{c}} = \frac{1}{\Delta t} \sum_{t_2=0}^{t-t_0} \sum_{t_i=0}^{t-t_0-t_2} \left(\lambda(t_0+t_2, t_0+t_i) - \lambda_{\mathrm{ref}}(t_0+t_i)\right), \tag{11}$$

where t_0 is the time of deposition, $\lambda(t_0, t)$ is the annual layer thickness at a time $t = t_0 + t_i$ after deposition, and λ_{ref} is the steady state reference. $\lambda(t_0, t)$ depends on the local mass balance and is given by

$$\lambda(t_0, t) = \begin{cases} \left(\frac{(b(t_0)-r(t_0))\rho_{\mathrm{i}}}{\rho_{\mathrm{f}}(t_0,t)} + r(t_0)\right)\tau & \text{, if } b(t_0) \geq 0 \\ b(t_0)\delta(t-t_0)\tau & \text{, if } b(t_0) < 0 \end{cases}, \tag{12}$$

where $r(t_0)$ is the amount of refrozen melt water, ρ_{i} is the density of ice, τ is a time constant usually equivalent to one year and δ is the Kronecker delta function (Reeh et al., 2005). The firn density $\rho_{\mathrm{f}}(t_0, t)$ can be derived from the Zwally and Li (2002) parameterisation of the Herron and Langway (1980) densification model

$$\rho_{\mathrm{f}}(t_0, t) = \begin{cases} \rho_{\mathrm{i}} - (\rho_{\mathrm{i}} - \rho_{\mathrm{s}}(t_0))\exp(-ct_i) & \text{, if } \rho_{\mathrm{f}}(t_0,t) \leq \rho_{\mathrm{c}} \\ \rho_{\mathrm{i}} - (\rho_{\mathrm{i}} - \rho_{\mathrm{c}})\exp(-c(t_i - t_c)) & \text{, if } \rho_{\mathrm{f}}(t_0,t) > \rho_{\mathrm{c}} \end{cases} \tag{13}$$

where ρ_{c} is the critical firn density of 550 kg/m^3 defined by Herron and Langway (1980), t_{c} is the time it takes for the firn to reach the critical density, and c is the densification constant describing the linear change in air volume in the firn due to the overlaying pressure (Reeh, 2008). The Zwally and Li parameterisation differs from the original Herron and Langway densification model by the parameterisation of c, where the Zwally and Li parameterisation is more sensitive to the temperature (Reeh, 2008). This sensitivity is important when evaluating changes in firn compaction on short time scales.

The densification constant is given by

$$c = \frac{b(t)\rho_{\mathrm{i}}}{\rho_{\mathrm{w}}} \beta(T) K_{\mathrm{G}}(T), \tag{14}$$

where $\beta(T)$ is a scale factor accounting for changes in grain growth with temperature T and ρ_{w} is the density of water. K_{G} is the rate factor for densification adjusted for grain growth

$$K_{\mathrm{G}} = K_{0_{\mathrm{G}}} \exp\left(\frac{E(T)}{RT}\right) = 8.36 T^{-2.061} \tag{15}$$

Here, $K_{0_{\mathrm{G}}}$ is the rate factor only for grain growth, E is the activation energy and R is the gas constant (Zwally and Li, 2002; Reeh, 2008). The effect of grain growth (β) was assumed to be eight by (Zwally and Li, 2002). Later empirical studies reported a site dependency of β between seven and three (Li et al., 2003) at sites with an annual mean temperature between −30 and −22 °C. We assume $\beta = 8$, since this study covers the entire GrIS, where annual mean temperature is exceeding temperatures of −22 °C in some areas.

5.2 HIRHAM5 – forcing of the firn compaction model

The annual mean temperature at two meter above the surface, runoff, snowfall and precipitation variables, required for the firn compaction model, are produced by dynamically downscaling the European Centre for Medium-Range Weather Forecast

(ECMWF) ERA-Interim reanalysis with the HIRHAM5 regional climate model (RCM). The HIRHAM5 RCM (Christensen et al., 2006) is a hydrostatic RCM developed at the Danish Meteorological Institute (DMI). It is based on the HIRLAM7 dynamics (Eerola, 2006) and ECHAM5 physics (Roeckner et al., 2003). The ERA-Interim reanalysis (Simmons et al., 2007), provided by the ECMWF, is a comprehensive reanalysis of the state of the atmosphere, using measurements from satellite, weather balloons and ground stations.

A continuous simulation with HIRHAM5 at 0.05 deg. (∼5.55 km) resolution on a rotated grid is realized from 1989–2008 using the ECMWF ERA-Interim at T255 (∼0.7° or ∼77 km) as lateral boundary conditions. The sea-surface temperature and sea-ice distribution, taken from ERA-Interim, were interpolated to the HIRHAM5 grid and prescribed to the model. The wind components, atmospheric temperature, specific humidity and surface pressure from ERA-Interim were transmitted to HIRHAM5 every six hours for each atmospheric model level of the HIRHAM5 RCM. At the lateral boundaries of the model domain, a relaxation scheme according to Davies (1976) is applied with a buffer zone of ten grid boxes. The high 5.5 km horizontal resolution data are appropriate to determine the precipitation distribution over the sharp edge of the ice sheet, where the ablation zone is located. The dynamical downscaling with a RCM allows to simulate climate variables, which are physically consistent, for every grid cell of the domain.

A comparison of the publicly available 1.5° × 1.5° ERA-Interim and the HIRHAM5 dynamical downscaling are shown in Fig. 3. It is clear how the high resolution HIRHAM5 RCM run is able to account for the complex coastal topography in Greenland. The coastal precipitation patterns propagate far inland to areas above the equilibrium line altitude (ELA), where the firn compaction is applied. This pattern is not captured by the ERA-Interim (see Fig. 3) and shows the need for the high resolution RCM's input to the firn compaction modelling.

5.3 Interpolated metric grid

In order to derive the mass change of the GrIS the area of each grid box has to be known. To ensure equal area of each grid box the high resolution data from the HIRHAM5 RCM is interpolated onto the equal distance 5 × 5 km grid by a nearest neighbor interpolation. The snowfall of 2008 in the two different map projections is shown in Fig. 3. It is seen that the pattern of snowfall is preserved after the grid transformation. However, the interpolation becomes noisier the greater the distance is to the equator of the original HIRHAM map projection. The noise is seen in the high precipitation area near Station Nord in the Northeastern Greenland. Despite the noise induced by the transformation of map projections, the equal distance grid gives a good approximation of the precipitation and temperature field over the GrIS produced by the HIRHAM5 model. We will use the HIRHAM5 on the equal distance grid, to force the surface density and firn compaction.

5.4 Refreezing of melt water and formation of ice lenses

On the GrIS, 60% of the run-off given by the HIRHAM5 RCM is assumed to refreeze in the snowpack (Reeh, 1991). The accumulation is calculated as the sum of snowfall and the refrozen run-off. To simplify the following derivation of a time dependent densification model the refrozen run-off is assumed to refreeze inside the annual layer in the firn, from which it originates, and the water is not allowed to penetrate deeper into the firn column. This assumption is in violation with observations from the Arctic snowpack where melt water is often seen to penetrate the snowpack until it reaches a hard layer where the melt water flows along until it refreezes or finds a crack to propagate downwards into the deeper firn (Benson, 1962; Bøggild, 2000; Jansson et al., 2003). In order to be able to model this behavior, sub-annual layering of the densification model and knowledge of grain growth in water-saturated firn would be required. Both of these are outside the scope of the present study of firn compaction, where the overburden

pressure is believed to be the driving force, despite the fact that melt water percolation may redistribute the load on a layer.

5.5 Results of firn compaction and density modelling

The density of the snow/ice involved in the mass change of the GrIS in Eq. (10), is modeled in order to derive the mass change of the GrIS from the ICESat measurements. The density is assumed to be either the density of ice or firn, depending on the location on the ice sheet. The density of the surface firn is highly dependent on the temperature during the precipitation event.

In the ablation zone, defined here for simplification as the area below the ELA, all elevation change is assumed to be caused by ice. Above the ELA, in the accumulation zone, an elevation increase is assumed to be caused by an addition of snow/firn. However, an elevation decrease is assumed to be caused by the remote removal of ice in the ablation zone as a response to ice dynamics. The surface density is then parameterised by

$$\rho = \begin{cases} \rho_s \text{ , if } \frac{dH}{dt} \geq 0 \text{ and H } \geq \text{ELA} \\ \rho_i \text{ , else} \end{cases}, \tag{16}$$

where ρ_s is the surface density of firn including ice lenses, and is given by

$$\rho_s = \frac{\rho_0}{1 - \frac{r}{b}\left(1 - \frac{\rho_0}{\rho_i}\right)}. \tag{17}$$

Here, r is the amount refrozen melt water inside an annual firn layer, $\rho_i = 900\ \mathrm{kg\,m^{-3}}$ and ρ_0 is the temperature dependent density of new firn before formation of ice lenses

$$\rho_0 = 625 + 18.7T + 0.293T^2 \tag{18}$$

(Reeh et al., 2005). T is the temperature given in °C. The ELA is determined using the polynomial parameterisation described by Box et al. (2004), where the ELA is given by

a 2nd order polynomial in West Greenland and a 5th order polynomial in East Greenland as a function of the latitude.

Based on the HIRHAM5 climatology for the period 1989 to 2008, the annual firn layer thickness has been computed according to Eq. (12). To derive the firn compaction velocity from Eq. (11) a steady state reference (λ_{ref}) has to be defined. The time span of the climate record is too short to define a robust steady state reference for the firn compaction. Moreover, the inter-annual variation in temperature and precipitation will bias a chosen reference to the climate pattern that is dominant in the time span of the reference period. To avoid defining the steady state reference layer thickness we have chosen to compare the thickness of the top firn layers in the period from 2003 to 2008. The maximum number of layers, which can be evaluated in 2003, is 15. Hence the thickness of the top 15 layers is compared from year to year in the period 2003 to 2008 at each grid point above the ELA. The change in the thickness is seen in Fig. 4a, along with the error in the linear fit in Fig. 4d. The change in the thickness of the 15 layers is a combination of changes in accumulation/surface melt and changes in the firn compaction. The change in the accumulation given in ice equivalent for the top 15 layer thickness is seen in Fig. 4b. By subtracting the change in the thickness of the 15 layers in ice equivalent from the 15 layer firn thickness, the change in air volume of the top firn, is found. The rate of change in this air volume in the firn is equivalent to the firn compaction velocity defined in Eq. (11). The approach of evaluating the relative change in air volume in each grid point above the ELA avoids the definition of a steady state reference for the firn compaction. The resulting firn compaction velocity is the linear trend in air volume of the top 15 layers for period 2003 to 2008, and is depicted in Fig. 4c. The error in the linear fit is seen Fig. 4f.

In Fig. 4c it is seen how the firn compaction velocity is mainly increasing in the central area of the GrIS, whereas, the firn in the coastal areas is becoming more dense. This pattern shows the importance of taking the firn processes into account, when relating an observed elevation change to a change in total mass balance of the GrIS. Depending on the assumed density of the volume changes the firn correction decreases the

mass loss of the ice sheet with 33–67 Gt yr^{-1}. This is a reduction of the mass loss of up to 30%, when compared to the direct mass loss estimate from the ICESat measurements without any firn compaction correction.

The error induced by the HIRHAM5 RCM in the firn compaction model is difficult to account for. Further studies have to be conducted to compare the modeled firn densities with in situ measurements before it is possible to estimate the total errors in the firn compaction velocity. Hence, the only error estimate of the firn compaction model is from the error in the linear fit of the inter-annual variability of the firn column. The 2σ are seen in the lower panel of Fig. 4. As seen in the figure the error associated with the firn compaction velocity is most pronounced in coastal areas near large outlet glaciers, where the HIRHAM5 RCM has the largest variability.

The error in the fitted firn compaction velocities will result in an error in the estimate of the total mass loss of the GrIS. The error seen in Fig. 4f has been summed over each of the 5×5 km grid boxes above the ELA, to give the resulting volume error. This volume induced by the error in the fitted firn velocities is then converted into mass by the surface density, resulting in a firn compaction induced error between 14–30 Gt yr^{-1} depending on which ice or firn density is assumed.

6 Additional elevation change corrections

The elevation changes observed by ICESat include signals from processes which do not contribute to the mass balance of the GrIS. The most significant contribution is the firn compaction, but it is also necessary to correct for glacial isostatic adjustment (GIA), elastic uplift caused by the present-day mass changes and the ICESat intercampaign elevation biases.

6.1 Vertical bedrock movement

Elevation changes which are not related to ice volume changes will be detected by ICESat, and these must be removed from the estimated $\frac{dH}{dt}$ values in order to determine the mass balance of the ice sheet. A bedrock movement (w_{br}) caused by GIA and elastic uplift from present-day mass changes will be a part of the elevation changes observed by ICESat.

We use a GIA contribution, according to Peltier (2004). It is based on the ice history model ICE-5G and the VM2 Earth model (http://pmip2.lsce.ipsl.fr/design/ice5g/). The rate of vertical motion caused by GIA is removed from the ICESat $\frac{dH}{dt}$ estimates. We find that this correction contributes to the mass balance of the GrIS with an amount of approximately +1 Gt yr^{-1}.

The present-day ice sheet mass changes cause an elastic response of the bedrock (e.g., Khan et al., 2010). These vertical displacements are computed by solving the Sea Level Equation, the fundamental equation that governs the sea level changes associated with glacial isostatic adjustment (Farrell and Clark, 1976). Since the time scale of the mass changes considered here is extremely short compared with the Maxwell relaxation time of the mantle (Spada et al., 2010), any viscoelastic effect is neglected and the ice thickness variations deduced by ICESat are spatially convolved with purely elastic loading "h" Love numbers. Sea level variations associated with melting are computed first, taking into account the elastic response of the Earth and the gravitational interaction between the ice sheets, the oceans and the mantle. Then, vertical displacements are retrieved by the surface load history over the entire surface of the Earth, associated with ice thickness variations and sea level changes. The results in Fig. 5 are obtained from a suitably modified version of the code SELEN 2.9 (Spada and Stocchi, 2007), which solves the Sea Level Equation iteratively, essentially following a variant of the pseudo-spectral method introduced by Mitrovica and Peltier (1991). A maximum harmonic degree $l_{max} = 128$ is used here. Vertical displacement is computed in the reference frame with the origin in the center of mass of the system (Earth+Load), and

includes the harmonic component of degree one (Greff-Lefftz and Legros, 1997). We find that the elastic uplift correction correspond to -4 to $-2\,\mathrm{Gt\,yr^{-1}}$, dependent on the mass loss. The elastic vertical displacement based on the results from method M3 (Sect. 3.3) is shown in Fig. 5.

6.2 ICESat intercampaign bias correction

It has been documented that there are elevation biases between the different ICESat laser campaigns. Following the method described in Gunter et al. (2009), the trend in the ICESat intercampain bias is estimated by (O. B. Andersen and T. Bondo, personal communication, 2010). The GLA15 release 31 ocean altimetry elevations are compared to a mean sea surface topography model (DNSC08). The trend is found to be $1.29 \pm 0.4\,\mathrm{cm\,yr^{-1}}$, when corrected for an assumed actual sea level rise of $0.3\,\mathrm{cm\,yr^{-1}}$ (Leuliette et al., 2004). This trend in intercampaign biases contributes with approximately $14 \pm 4\,\mathrm{Gt\,yr^{-1}}$ to the mass balance.

7 Mass balance of the GrIS

Determining the mass change of the GrIS is a complex problem with multiple solutions, depending on the type of observation and/or the level of theoretical complexity applied to solve the problem. This complexity can explain the different estimates of the total mass balance of the GrIS, which appear in the literature. To summarize the results of our studies, the total mass balance estimates of the GrIS are listed in Table 2. We have chosen to derive the mass change with and without the firn compaction correction of elevation change, to highlight the importance of this correction. The second key assumption in the derivation of the mass loss is ρ, from which the volume change is related to mass. The assumption, that an elevation decrease above the ELA is caused by a loss of glacial ice somewhere in the ablation area by ice dynamics, enhances the estimated mass loss of the GrIS. Therefore, the total mass balances estimates

(Table 2) are derived with and without this remote mass loss of ice. In the calculation without remote ice loss, ρ_s is applied for all elevation changes above the ELA.

Our best estimate of the present total mass balance of the GrIS is $-210 \pm 21\,\mathrm{Gt\,yr^{-1}}$ based on the comprehensive error analysis of the ICESat observations and theoretical treatment of the surface density and firn compaction modelling. The spatial distribution of the mass balance is seen in Fig. 6. This mass loss is equivalent to a global sea level rise of $0.58\,\mathrm{mm\,yr^{-1}}$. The uncertainty estimate on the mass change is obtained from the bootstrap procedure. Each resample is transformed into a mass change estimates according to Sect. 5, hence the 1000 resamples will make up a distribution from which the error is obtained.

The mass loss of the major outlet glaciers is evident in the figure, along with the interior part of the GrIS showing no changes over the period. The western side of the South Greenland ice divide is appearing to gain mass, which may be caused by the increasing precipitation (cf. Fig. 4c). The most prominent area of mass increase is the upper area of the Storstrømmen (Bøggild et al., 1994) outlet glacier in Northeast Greenland. The ice sheet drainage basin ending in Storstrømmen is believed to originate in the central part of the GrIS near the summit area (Rignot and Kanagaratnam, 2006). Therefore, changes in Storstrømmen glacier may be caused by effects inland, or the dynamical response of the GrIS due to changes in climate. However, this has to be verified by additional studies of this area.

8 Discussion and conclusions

Using four different methods to derive elevation changes of the GrIS from ICESat data during the period 2003–2008 reveals a consistent picture of massive ice thinning along the margin of the GrIS and a smaller elevation increase in the interior parts. The thinning is most evident along the southeast and the west coasts. An interpolation and bootstrap approach is applied, in order to derive a total annual vol-

ume change of snow/ice together with uncertainties for all four methods. We find volume changes of $-237 \pm 25\,km^3\,yr^{-1}$ to $-147 \pm 24\,km^3\,yr^{-1}$ depending on the method used. We conclude that method 3 is preferable, corresponding to a volume change of $-237 \pm 25\,km^3\,yr^{-1}$.

In order to correct the observed elevation changes for processes not contributing to the mass balance, we have estimated the firn compaction, vertical bedrock movement caused by GIA and elastic uplift, and the ICESat intercampaign elevation bias.

The firn compaction model is forced by the HIRHAM5 RCM, and we find this correction to be the largest and that it contributes with approximately $+57 \pm 14\,Gt\,yr^{-1}$ to the total mass balance. The trend in the ICESat intercampaign bias is found to be $-1.29 \pm 0.4\,cm\,yr^{-1}$ which corresponds to a mass gain of approximately $14 \pm 4\,Gt\,yr^{-1}$. The elastic uplift of the bedrock, caused by the present-day mass changes are found to contribute with -4 to $-2\,Gt\,yr^{-1}$ to the total mass balance and the GIA correction is $+1\,Gt\,yr^{-1}$.

The firn compaction model can, beside its application shown here, also be used to validate the RCM forcing, by comparing the modelled stratification of the firn with in situ observation from the GrIS. However, a model comparison study of different RCs for the GrIS has not been within the scope of the presented work, but might be elaborated in the future.

Modelled surface densities are used to convert the volume change into mass balance. Based on the preferred method M3, for deriving elevation changes, we estimate a mass balance of the GrIS for 2003–2008 of $-210 \pm 21\,Gt\,yr^{-1}$. This mass loss is equivalent to a global sea level rise of $0.58\,mm\,yr^{-1}$.

This mass balance estimate is in good agreement with results by others. Based on GRACE data, Velicogna (2009) has estimated the mass loss to be $230 \pm 33\,Gt\,yr^{-1}$ during the period 2002–2009, and Wouters et al. (2008) find a mass loss of $179 \pm 25\,Gt\,yr^{-1}$ for the years 2003–2008. van den Broeke et al. (2009) find a total mass balance of $-237 \pm 20\,Gt\,yr^{-1}$ for 2003–2008, from modeled surface mass balance and observed discharge.

Finally, our total mass balance result is large compared to the ICESat derived mass loss of $139 \pm 68\,Gt\,yr^{-1}$ found by Slobbe et al. (2009), based on data from 2003 to 2007. We believe that we have improved the application of ICESat data to estimate the total mass balance of the GrIS, by using a novel approach including firn compaction and density modelling.

Acknowledgements. We acknowledge the Danish National Research Foundation for funding the CIC. This work was supported by funding to the ice2sea programme from the European Union 7th Framework Programme, grant number 226375 (Ice2sea contribution number 014). Code SELEN is available from GS or it can be downloaded from http://www.fis.uniurb.it/spada/SELEN_minipage.html. Part of this work was supported by COST Action ES0701 "Improved constraints on models of Glacial Isostatic Adjustment". ECMWF ERA-interim data have been provided by ECMWF from the ECMWF Data Server. ICESat data was downloaded from the NSIDC web site.

References

Abdalati, W., Krabill, W., Frederick, E., Manizade, S., Martin, C., Sonntag, J., Swift, R., Thomas, R., Wright, W., and Yungel, J.: Outlet glacier and margin elevation changes: near-coastal thinning of the Greenland ice sheet, J. Geophys. Res., 106, 33729–33741, doi:10.1029/2001JD900192, 2001. 2105, 2113

Abshire, J. B., Sun, X., Riris, H., Sirota, J. M., McGarry, J. F., Palm, S., Yi, D., and Liiva, P.: Geoscience Laser Altimeter System (GLAS) on the ICESat mission: on-orbit measurement performance, Geophys. Res. Lett., 32, L21S02, doi:10.1029/2005GL024028, 2005. 2107

Benson, C. S.: Stratigraphic Studies in the Snow and Firn of the Greenland Ice Sheet, Tech. Rep. 70, SIPRE (Snow Ice and Permafrost Research Establishment) Research Report, US army corps of engineers, Hanover, New Hampshire, 1962. 2120

Bøggild, C. E.: Preferential flow and melt water retention in cold snow packs in West-Greenland, Nord. Hydrol., 31, 287–300, 2000. 2120

Bøggild, C. E., Reeh, N., and Oerter, H.: Modelling ablation and mass-balance sensitivity to climate change of Storstrømmen, Northeast Greenland, Global Planet. Change, 9, 79–90, doi:10.1016/0921-8181(94)90009-4, 1994. 2126

Box, J. E., Bromwich, D. H., and Bai, L.-S.: Greenland ice sheet surface mass balance 1991–2000: application of Polar MM5 mesoscale model and in situ data, J. Geophys. Res., 109, 16105, doi:10.1029/2003JD004451, 2004. 2121

Christensen, O. B., Drews, M., Christensen, J., Dethloff, K., Ketelsen, K., Hebestadt, I., and Rinke, A.: The HIRHAM regional climate model. Version 5, Tech. Rep. 06-17, DMI technical report, available at: http://www.dmi.dk/dmi/tr06-17.pdf, Cambridge University Press, Cambridge, 2006. 2119

Davies, H. C.: A laterul boundary formulation for multi-level prediction models, Q. J. Roy. Meteor. Soc., 102, 405–418, doi:10.1002/qj.49710243210, 1976. 2119

Davison, A. C. and Hinkley, D.: Bootstrap Methods and their Application, 8th edn., Cambridge Series in Statistical and Probabilistic Mathematics, Meteorological Institute, University of Bonn, Bonn, 2006. 2114

DiMarzio, J., Brenner, A., Schutz, R., Shuman, C., and Zwally, H.: GLAS/ICESat 1 km laser altimetry digital elevation model of Greenland, Digital media, National Snow and Ice Data Center, Boulder, CO, 2007. 2109

Eerola, K.: About the performance of HIRLAM version 7.0, Tech. Rep. 51 Article 14, HIRLAM Newsletter, available at: http://hirlam.org/, Danish Meteorological Institute, Copenhagen, 2006. 2119

Farrell, W. E. and Clark, J. A.: On postglacial sea level, Geophys. J. Roy. Astr. S., 46, 647–667, doi:10.1111/j.1365-246X.1976.tb01252.x, 1976. 2124

Fricker, H. A. and Padman, L.: Ice shelf grounding zone structure from ICESat laser altimetry, Geophys. Res. Lett., 33, L15502, doi:10.1029/2006GL026907, 2006. 2106, 2108

Fricker, H. A., Borsa, A., Minster, B., Carabajal, C., Quinn, K., and Bills, B.: Assessment of ICESat performance at the salar de Uyuni, Bolivia, Geophys. Res. Lett., 32, L21S06, doi:10.1029/2005GL02342, 2005. 2107

Greff-Lefftz, M. and Legros, H.: Some remarks about the degree one deformations of the Earth, Geophys. J. Int., 131, 699–723, doi:10.1111/j.1365-246X.1997.tb06607.x, 1997. 2125

Gunter, B., Urban, T., Riva, R., Helsen, M., Harpold, R., Poole, S., Nagel, P., Schutz, B., and Tapley, B.: A comparison of coincident GRACE and ICESat data over Antarctica, J. Geodesy, 83, 1051–1060, doi:10.1007/s00190-009-0323-4, 2009. 2125

Helsen, M. M., van den Broeke, M. R., van de Wal, R. S. W., van de Berg, W. J., van Meijgaard, E., Davis, C. H., Li, Y., and Goodwin, I.: Elevation changes in Antarctica mainly determined by accumulation variability, Science, 320, 1626–1629, doi:10.1126/science.1153894,

2008. 2116

Herron, M. and Langway, C.: Firn densification: an empirical model, J. Glaciol., 25, 373–385, 1980. 2117, 2118

Howat, I. M., Smith, B. E., Joughin, I., and Scambos, T. A.: Rates of Southeast Greenland ice volume loss from combined ICESat and ASTER observations, Geophys. Res. Lett., 35, L17505, doi:10.1029/2008GL034496, 2008. 2106, 2108, 2111

Jansson, P., Hock, R., and Schneider, T.: The concept of glacier storage: a review, J. Hydrol., 282, 116–129, doi:10.1016/S0022-1694(03)00258-0, 2003. 2120

Joughin, I., Smith, B. E., Howat, I. M., Scambos, T., and Moon, T.: Greenland flow variability from ice-sheet-wide velocity mapping, J. Glaciol., 56, 415–430(16), doi:10.3189/002214310792447734, 2010. 2105

Khan, S. A., Wahr, J., Bevis, M., Velicogna, I., and Kendrick, E.: Spread of ice mass loss into Northwest Greenland observed by GRACE and GPS, Geophys. Res. Lett., 37, L06501, doi:10.1029/2010GL042460, 2010. 2124

Leuliette, E. W., Nerem, R. S., and Mitchum, G. T.: Calibration of TOPEX/Poseidon and Jason altimeter data to construct a continuous record of mean sea level changes, Mar. Geod., 27, 79–94, doi:10.1080/01490410490465193, 2004. 2125

Li, J., Zwally, H. J., Cornejo, H., and Yi, D.: Seasonal variation of snow-surface elevation in North Greenland as modeled and detected by satellite radar altimetry, Ann. Glaciol., 37, 233–238, doi:10.3189/172756403781815889, 2003. 2118

Li, J., Zwally, H. J., and Comiso, J. C.: Ice-sheet elevation changes caused by variations of the firn compaction rate induced by satellite-observed temperature variations (1982–2003), Ann. Glaciol., 46, 8–13, doi:10.3189/172756407782871486, 2007. 2106

Luthcke, S. B., Zwally, H. J., Abdalati, W., Rowlands, D. D., Ray, R. D., Nerem, R. S., Lemoine, F. G., McCarthy, J. J., and Chinn, D. S.: Recent Greenland ice mass loss by drainage system from satellite gravity observations, Science, 314, 1286–1289, doi:10.1126/science.1130776, 2006. 2106

Mitrovica, J. X. and Peltier, W. R.: On post-glacial geoid subsidence over the equatorial ocean, J. Geophys. Res., 96, 20 053–20 071, 1991. 2124

NSIDC: GLAS altimetry product usage guidance, available at: http://nsidc.org/data/docs/daac/glas_altimetry/usage.html, National Snow and Ice data Center, University of Colorado, Boulder, 2010. 2107

Paterson, W. S. B.: Physics of Glaciers, 3rd edn., Butterworth-Heinemann, 3rd edn. 1994,

reprinted with corrections 1998, 2001, 2002, Oxford, 2002. 2116
Pebesma, E. J.: Mapping groundwater quality in The Netherlands, Netherlands Geographical studies, 199, avilable at: http://www.geog.uu.nl/ngs/ngs.html,Utrecht University, Utrecht, 1996. 2114
Pebesma, E. J.: Multivariable geostatistics in S: the gstat package, Comput. Geosci., 30, 683–691, doi:10.1016/j.cageo.2004.03.012, 2004. 2114
Peltier, W.: Global glacial isostasy and the surface of the ice-age Earth: the ICE-5G (VM2) model and GRACE, Annu. Rev. Earth Pl. Sc., 32, 111–149, doi:10.1146/annurev.earth.32.082503.144359, 2004. 2124
Pritchard, H. D., Arthern, R. J., Vaughan, D. G., and Edwards, L. A.: Extensive dynamic thinning on the margins of the Greenland and Antarctic ice sheets, Nature, 461, 971–975, doi:10.1038/nature08471, 2009. 2106, 2108, 2110, 2113
Reeh, N.: Parameterization of melt rate and surface temperature on the Greenland ice sheet, Polarforschung 1989, 5913, 113–128, 1991. 2120
Reeh, N.: A nonsteady-state firn-densification model for the percolation zone of a glacier, J. Geophys. Res., 113, F03023, doi:10.1029/2007JF000746, 2008. 2117, 2118
Reeh, N., Fisher, D. A., Koerner, R. M., and Clausen, H. B.: An empirical firn-densification model comprising ice lenses, Ann. Glaciol., 42, 101–106, doi:10.3189/172756405781812871 http://www.ingentaconnect.com/content/igsoc/agl/2005/00000042/00000001/art00017, 2005. 2117, 2121
Rignot, E. and Kanagaratnam, P.: Changes in the velocity structure of the Greenland ice sheet, Science, 311, 986–990, doi:10.1126/science.1121381, 2006. 2105, 2126
Rignot, E., Braaten, D., Gogineni, S. P., Krabill, W. B., and McConnell, J. R.: Rapid ice discharge from Southeast Greenland glaciers, Geophys. Res. Lett., 31, L10401, doi:10.1029/2004GL019474, 2004. 2105
Roeckner, E., Bauml, G., Bonaventura, L., Brokopf, R., Esch, M., Giorgetta, M., Hagemann, S., Kirchner, I., Kornblueh, L., Manzini, E., Rhodin, A., Schlese, U., Schulzweida, U., and Tompkins, A.: The atmospheric general circulation model ECHAM 5. Part I: model description, Tech. Rep. 349, Max-Planck-Institute for Meteorology, Hamburg, 2003. 2119
Simmons, A., Uppala, S., Dee, D., and Kobayashi, S.: ERA-interim: new ECMWF reanalysis products from 1989 onwards, ECMWF Newsletter, 110, 25–35, 2007. 2119
Slobbe, D., Lindenbergh, R., and Ditmar, P.: Estimation of volume change rates of Greenland's ice sheet from ICESat data using overlapping footprints, Remote Sens. Environ., 112, 4204–

4213, doi:10.1016/j.rse.2008.07.004, 2008. 2106, 2108, 2109, 2113
Slobbe, D., Ditmar, P., and Lindenbergh, R.: Estimating the rates of mass change, ice volume change and snow volume change in Greenland from ICESat and GRACE data, Geophys. J. Int., 176, 95–106, doi:10.1111/j.1365-246X.2008.03978.x, 2009. 2128
Smith, B. E., Bentley, C. R., and Raymond, C. F.: Recent elevation changes on the ice streams and ridges of the Ross Embayment from ICESat crossovers, Geophys. Res. Lett., 32, L21S09, doi:doi:10.1029/2005GL024365, 2005. 2107
Smith, B. E., Fricker, H. A., Joughin, I. R., and Tulaczyk, S.: An inventory of active subglacial lakes in Antarctica detected by ICESat (2003-2008), J. Glaciol., 55, L21S09, 2009. 2111
Sørensen, L. S. and Forsberg, R.: Greenland ice sheet mass loss from GRACE monthly models, Gravity Geoid Earth Observ., 135, 527–532, doi:10.1007/978-3-642-10634-7_70, 2010. 2106
Spada, G. and Stocchi, P.: SELEN: a Fortran 90 program for solving the "Sea Level Equation", Comput. Geosci., 33(4), 538–562, doi:10.1016/j.cageo.2006.08.006., 2007. 2124
Spada, G., Colleoni, F., and Ruggieri, G.: Shallow upper mantle rheology and secular ice sheets fluctuations, Tectonophysics, doi:10.1016/j.tecto.2009.12.020, 2010. 2124
Thomas, R., Davis, C., Frederick, E., Krabill, W., Li, Y., Manizade, S., and Martin, C.: A comparison of Greenland ice-sheet volume changes derived from altimetry measurements, J. Glaciol., 54, 203–212, doi:10.3189/002214308784886225, 2008. 2113
Thomas, R., Frederick, E., Krabill, W., Manizade, S., and Martin, C.: Recent changes on Greenland outlet glaciers, J. Glaciol., 55, 147–162, doi:10.3189/002214309788608958, 2009. 2113
van den Broeke, M., Bamber, J., Ettema, J., Rignot, E., Schrama, E., van de Berg, W. J., van Meijgaard, E., Velicogna, I., and Wouters, B.: Partitioning recent greenland mass loss, Science, 326, 984–986, doi:10.1126/science.1178176, 2009. 2106, 2127
Velicogna, I.: Increasing rates of ice mass loss from the Greenland and Antarctic ice sheets revealed by GRACE, Geophys. Res. Lett., 36, L19503, doi:10.1029/2009GL040222, 2009. 2127
Velicogna, I. and Wahr, J.: Greenland mass balance from GRACE, Geophys. Res. Lett., 32, L18505, doi:10.1029/2005GL023955, 2005. 2106
Wouters, B., Chambers, D., and Schrama, E. J. O.: GRACE observes small-scale mass loss in Greenland, Geophys. Res. Lett., 35, L20501, doi:10.1029/2008GL034816, 2008. 2106, 2127

Wu, X., Heflin, M., Schotman, H., Vermeersen, B., Dong, D., Gross, R., Ivins, E., Moore, A., and Owen, S.: Simultaneous estimation of global present-day water transport and glacial isostatic adjustment, Nat. Geosci., 3, 642–646, doi:10.1038/ngeo938, 2010. 2106

Zwally, H., Schutz, R., Bentley, C., Bufton, J., Herring, T., Minster, J., Spinhirne, J., and Thomas, R.: GLAS/ICESat L2 Antarctic and Greenland ice sheet altimetry data V031, National Snow and Ice Data Center, Boulder, CO, avilable at: http://nsidc.org/data/gla12.html, 2010. 2107

Zwally, H. J. and Li, J.: Seasonal and interannual variations of firn densification and ice-sheet surface elevation at the Greenland summit, J. Glaciol., 48, 199–207, doi:10.3189/172756502781831403, 2002. 2116, 2117, 2118

Table 1. ICESat data description. Shown is the laser campaign identifier (ID), data release number (RL), and time span of the campaigns. *N* and *M* are the number of measurements from the GrIS before and after the data culling, respectively.

ID	RL	Time span	*N*	*M*
L2A	531	4 Oct 2003–18 Nov 2003	1 095 647	941 052
L2B	531	17 Feb 2004–20 Mar 2004	815 998	695 242
L2C	531	18 May 2004–20 Jun 2004	739 672	680 031
L3A	531	3 Oct 2004–8 Nov 2004	851 789	727 425
L3B	531	17 Feb 2005–24 Mar 2005	829 689	704 680
L3C	531	20 May 2005–22 Jun 2005	800 876	679 827
L3D	531	21 Oct 2005–23 Nov 2005	821 825	695 949
L3E	531	22 Feb 2006–27 Mar 2006	883 492	752 123
L3F	531	24 May 2006–25 Jun 2003	743 702	626 463
L3G	531	25 Oct 2006–27 Nov 2003	809 655	698 710
L3H	531	12 Mar 2007–14 Apr 2007	838 647	778 350
L3I	531	2 Oct 2007–4 Nov 2007	761 576	705 639
L3J	531	17 Feb 2008–21 Mar 2008	375 239	368 148
Total			10 367 807	9 053 639

Table 2. The total mass balance the GrIS estimated based on the different methods of ICESat processing and assumptions in the firn compaction modelling. The contribution to the total mass balance above and below the ELA is specified, along with the total mass balance above an altitude of 2000 m. The error estimate from the firn compaction modelling is derived only for the full firn correction. Note that the mass balance below the ELA is unaffected by firn model processes and is therefore the same for all firn assumptions.

		With remote removal of ice				Without remote removal of ice		
	ICESat Volume [$km^3\,yr^{-1}$]	Total [$Gt\,yr^{-1}$]	Above ELA [$Gt\,yr^{-1}$]	Above 2000 m [$Gt\,yr^{-1}$]	Below ELA [$Gt\,yr^{-1}$]	Total [$Gt\,yr^{-1}$]	Above ELA [$Gt\,yr^{-1}$]	Above 2000 m [$Gt\,yr^{-1}$]
With firn correction								
M1	-225 ± 23	-199 ± 20	−72	−7	−127	−157	−30	+6
M2	-179 ± 15	-155 ± 12	−54	−5	−101	−121	−20	+7
M3	-237 ± 25	-210 ± 21	−77	−8	−133	−166	−33	+5
M4	-147 ± 24	-118 ± 21	−40	−9	−78	−92	−14	+2
Without firn correction								
M1	−225	−256	−129	−28	−127	−190	−63	−5
M2	−179	−212	−111	−25	−101	−154	−53	−4
M3	−237	−267	−134	−29	−133	−199	−66	−5
M4	−147	−177	−99	−31	−78	−126	−48	−9

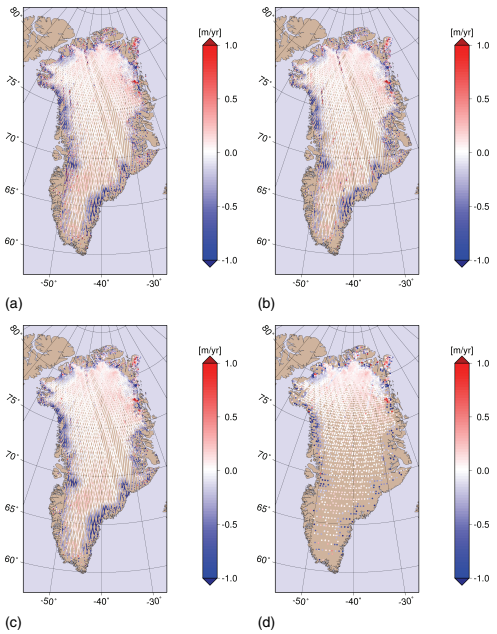

Fig. 1. Elevation changes derived from ICESat data using 4 different methods. **(a)** M1, **(b)** M2, **(c)** M3, and **(d)** M4.

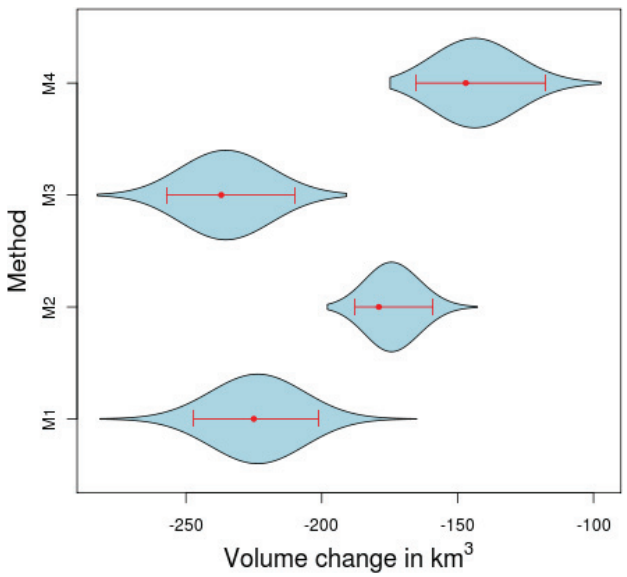

Fig. 2. Violin plot of the 4 method results. The blue area indicates the distribution of 1000 bootstrap samples. The red dots are the point estimates of volume change, and the red bars indicate the 95% confidence interval.

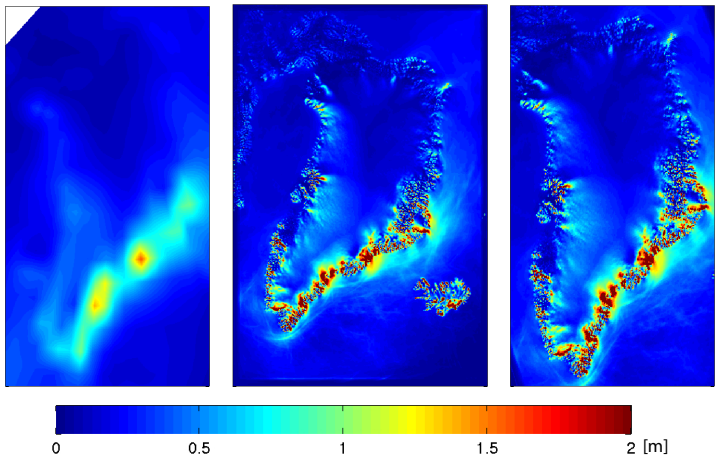

Fig. 3. The 2008 snowfall on a scale at 0 to 2 m of water equivalent (from blue to red). (Left) The ERA-Interim 1.5° × 1.5° resolution linear interpolated onto the equal distance 5 km × 5 km grid. (Middle) The regional HIRHAM5 dynamical downscaling of the ERA-Interim. HIRHAM5 applies a rotated map projection, with a grid spacing of 0.05° × 0.05°. This projection gives a metric resolution of ~5.5 km × 5.5 km. (Right) Nearest neighbor interpolation of the HIRHAM5 onto the equal distance 5 km × 5 km grid. The highly dynamic behavior of the precipitation from the HIRHAM5 model is preserved in the transformation of the map projections.

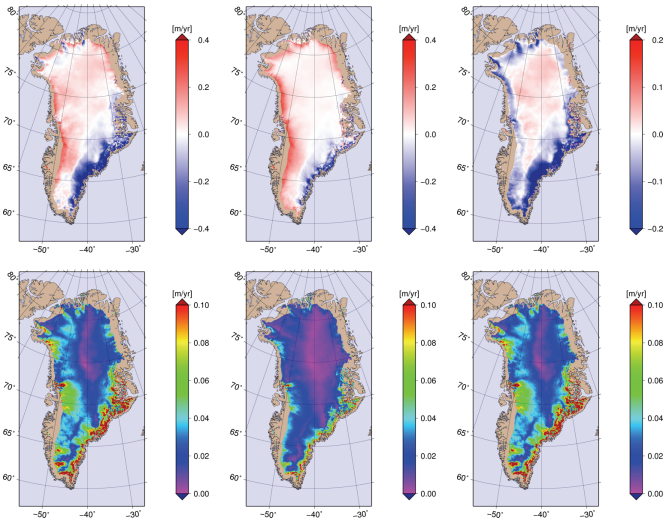

Fig. 4. The different contributions to the the firn compaction modelling for the period from 2003 to 2008, forced by the HIRHAM5 climatology. Only the area above the ELA is shown in the figure. The upper panels show the modeled firn process, estimated from a linear fit for the period 2003 to 2008. **(a)** The modeled change in the thickness of the top 15 annual firn layers. **(b)** The change of ice equivalent thickness of the top 15 annual firn layers. **(c)** The change in air volume in the top firn, which is equivalent to the firn compaction velocity defined in Eq. (11). The work flow of the computations is (c) = ($a - b$). **(d)**, **(e)** and **(f)** show the 2σ standard deviation of the linear trend in (a), (b) and (c), respectively.

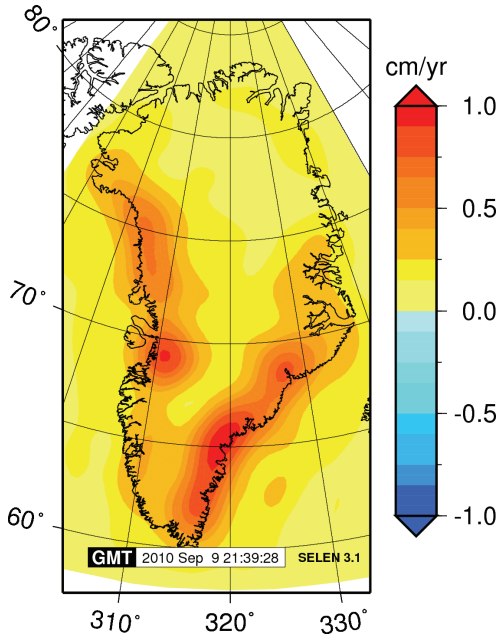

Fig. 5. Elastic vertical displacement caused by present-day mass changes in Greenland, referred to the period of one year, computed according to mass changes obtained by M3.

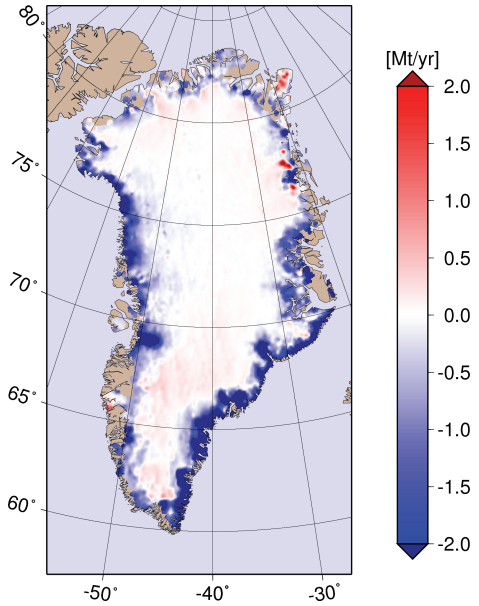

Fig. 6. The yearly spatial distribution of the mass change of the GrIS, derived for each of the grid cells. The result is based on the estimate derived by M3. The pattern of coastal thinning seen in Fig. 1 is also found in the mass change of the GrIS.

Appendix C

Paper 3

Hvidegaard, Sine Munk, Sørensen, L. S. and Forsberg, R. (2010), *ASTER GDEM validation using LiDAR data over coastal regions of Greenland*, In press, Remote Sensing Letters. Hvidegaard et al. (2010)

TRSL_A_527389
C/e: AA C/e QA: SD
Remote Sensing Letters
Vol. 00, No. 00, Xxxx 2010, 1–7

Taylor & Francis
Taylor & Francis Group

ASTER GDEM validation using LiDAR data over coastal regions of Greenland

SINE MUNK HVIDEGAARD*, LOUISE SANDBERG SØRENSEN and RENÉ FORSBERG

National Space Institute, Technical University of Denmark, DK-2100 Copenhagen, Denmark

(*Received 12 February 2010; in final form 15 September 2010*)

Elevation data from airborne Light Detection and Ranging (LiDAR) campaigns are used in an attempt to evaluate the accuracy of the ASTER global digital elevation model (GDEM) in Greenland.

The LiDAR elevation data set is characterized by a high spatial resolution of about 1 m and elevation accuracy of 20–30 cm root mean square error. The LiDAR data sets used were acquired during ice-monitoring campaigns carried out from 2003 to 2008. The study areas include ice-free regions, local ice caps and the ice sheet margin. A linear error of 15–65 m was derived, which is far greater than the 20-m product specification. This estimation is biased by both the seasonal and the climatic changes in local ice caps because the ASTER GDEM was computed from imagery acquired in the period 2000–2009. High sloping areas along the coastal regions of Greenland and the effect of the number of scenes used to generate the ASTER GDEM as well as relief are associated to the GDEM accuracy.

1. Introduction

The ASTER global digital elevation model (GDEM) provides an almost total coverage of Greenland at 1 arc-second grid spacing, and the global average accuracy is estimated to be 20 m in vertical (linear) error and 30 m in horizontal (positioning accuracy) error (ASTER GDEM Validation Team 2009). With this resolution and accuracy, the ASTER GDEM will improve the current digital elevation models (DEMs) significantly over vast areas of Greenland.

The GDEM is created by stacking of individual scene-based DEMs that have been generated using an automated processing including stereo-correlation. These DEMs are masked for clouds and corrected for residual anomalies. There is no orthorectification included in the pre-processing of the ASTER imagery.

Light Detection and Ranging (LiDAR) elevation data from several airborne campaigns over Greenland are used to quantify the ASTER GDEM accuracy. The study areas include ice-free land areas and regions of the ice sheet and glaciers close to land. The aim of this letter is to evaluate the vertical accuracy of the ASTER GDEM for the study areas and identify some of the various sources of error that are associated.

*Corresponding author. Email: smh@space.dtu.dk

Remote Sensing Letters
ISSN 2150-704X print/ISSN 2150-7058 online © 2010 Taylor & Francis
http://www.tandf.co.uk/journals
DOI: 10.1080/01431161.2010.527389

2. Data

2.1. *ASTER GDEM*

The ASTER Global DEM, released in June 2009, is a product made available by The Ministry of Economy, Trade and Industry of Japan (METI) and National Aeronautics and Space Administration (NASA). It is created by stereo-correlation of 1.5 million ASTER visible and near-infrared (VNIR) images. The stereo-correlation is performed on images from the nadir and backward-looking detector in band 3 (VNIR) and provides a GDEM with horizontal resolution of 1 arc-second available in tiles of 1 by 1 degree. The time span of the images used to generate the model is 2000–2009. A quality assessment (QA) file specifying the number of images used to generate each ASTER elevation value is supplied with each ASTER GDEM file (http://asterweb.jpl.nasa.gov/gdem.asp).

The study areas are presented in figure 1. The study areas 1, 2 and 4 include partially ice-covered regions (figure 1) whereas the study area 3 is ice free. In figure 2(*a*), elevation data from the eastern part of Disko Island are visualized.

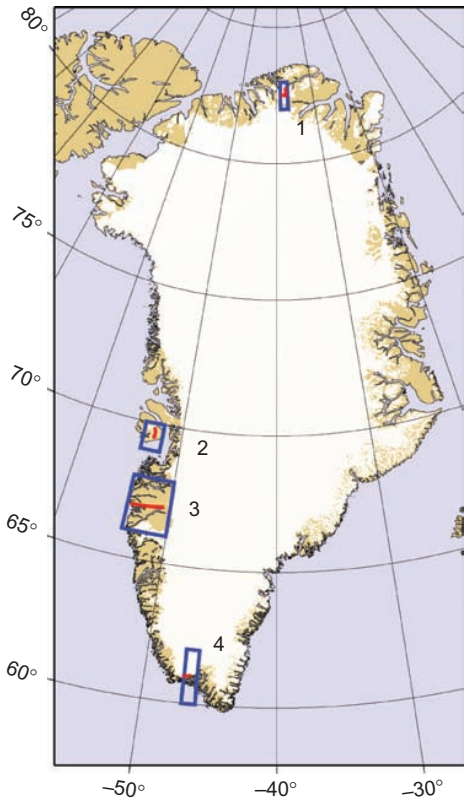

COLOUR FIGURE

Figure 1. The areal extent (outlined in blue) of the study areas 1, 2, 3 and 4 and the airborne LiDAR tracks (red lines) superimposed on a Greenland map with the ice extent visualized in white.

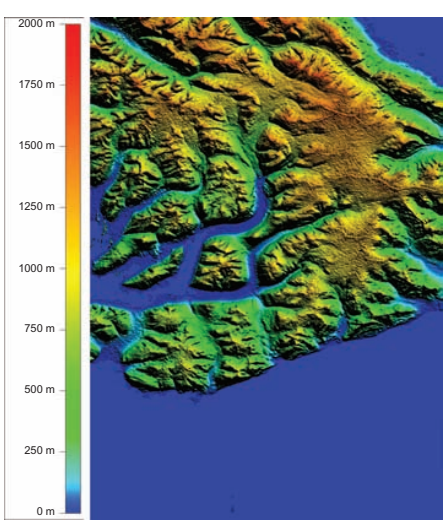

(*a*)

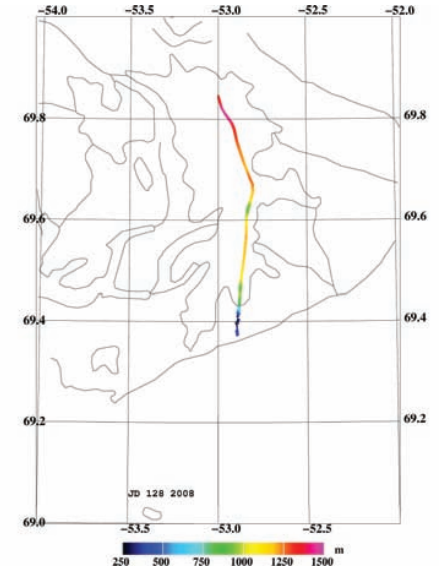

(*b*)

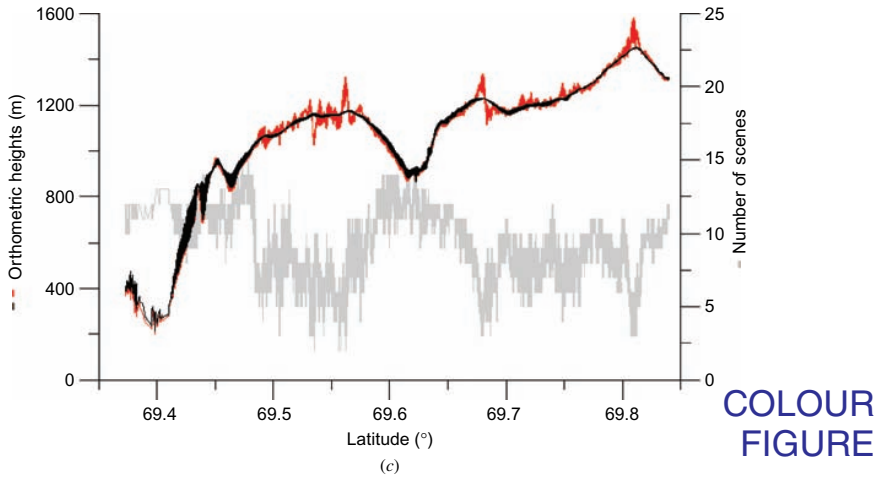

(*c*)

COLOUR FIGURE

Figure 2. (*a*) ASTER GDEM tiles covering the geographic region 69°N–70°N and 54°W–52°W, (*b*) the elevation data acquired during the LiDAR campaign of May 2008, (*c*)LiDAR elevations are shown in black while GDEM elevations along the LiDAR campaign are shown in red. Number of images, QA, is shown in grey.

2.2. *LiDAR data*

A detailed description of the airborne system used to acquire the LiDAR data is given in Lintz *et al.* (2000), Forsberg *et al.* (2001) and Hvidegaard *et al.* (2009). The system is based on a near-infrared laser scanner, with positioning by geodetic long-baseline kinematic GPS, and attitude information from a medium-grade inertial navigation system. The combined systems yield an absolute vertical accuracy of 20–30 cm root mean square error (RMSE) (Hvidegaard *et al.* 2009), in swaths of width roughly equal

Table 1. Validation of ASTER GDEM – statistics on the difference between GDEM and ground truth (LiDAR) elevations per study area. Q7

Area	ASTER GDEM tile area	LiDAR data	Difference range (m)	Mean difference (m)	Standard deviation (m)	RMSE (m)	95% Confidence level (m)
1	82°N–83°N and 39°W–37°W	2004, DOY 135	[–319; 484]	11	38	43.5	~70
2	69°N–70°N and 54°W–52°W	2004, DOY 147	[–86; 59.8]	11.9	11.5	17.4	~30
		2006, DOY 114	[–149; 591]	11.1	61	66.6	~58
		2008, DOY 128	[–152; 135.4]	0.6	25.1	25.6	~51
3	66°N–67°N and 54°W–53°W	2004, DOY 155	[–21.9; 445.8]	12.9	7.9	20.8	~26
	66°N–68°N and 54°W–50°W	2003, DOY 223	[–112.9; 289.7]	13.9	12.5	19.4	~34
	66°N–68°N and 51°W–50°W	2008, DOY 108	[–98; 64.7]	4.4	17.4	19.6	~37
4	60°N–62°N and 47°W–46°W	2007, DOY 216	[–95.7; 37.6]	–19.5	18	27.8	~52

Note: More information about the LiDAR data sets can be found in Hvidegaard *et al.* (2009).

to the flight altitude, typically 200–300 m above ground level. The horizontal resolution of the LiDAR points is approximately 1 m and the internal relative accuracy between 1-m points is better than that between 5-cm points. Q3

A DEM with 5 m spacing is interpolated from the LiDAR point cloud data and used for comparisons with accuracy specifications as described above. Both the ASTER GDEM and the LiDAR DEM are digital surface models representing maximum elevation figures. There is no significant vegetation in any of the land areas scanned.

LiDAR data from a number of different ice-monitoring campaigns carried out in the period 2004–2008 are used (see table 1 for dates of the individual LiDAR campaigns). Eight LiDAR tracks were used as reference: Three from ice-free areas and five from partially covered areas (see table 1). The ice-covered areas include small local ice caps and marginal zones of the ice sheet. Area 3 in figure 1 includes three different LiDAR surveys over two villages, Kangerlussuaq and Sisimiut, and a profile track between the two villages. This LiDAR track is shown in figure 3. The 8 LiDAR surveys are included in 12 ASTER tiles.

3. Method and results

The LiDAR elevations referenced to the WGS84 vertical datum were transformed to the EGM96 geoid. A vertical datum transformation error of 0.5 m was induced in the elevation values. A bilinear interpolation method was used to predict the ASTER GDEM elevation at the sampling interval of the LiDAR data, and differences subsequently produced. The statistics of these differences, in terms of minimum, maximum, mean, standard deviation, RMSE and the 95% confidence level accuracy of the elevation differences in the LiDAR data points have been calculated (according to Maune 2001, chap. 3) for each study area (table 1). The ASTER GDEM tiles show elevation accuracy expressed as RMSE in the range of both 15–65 m and 25–70 m at the 95% confidence interval.

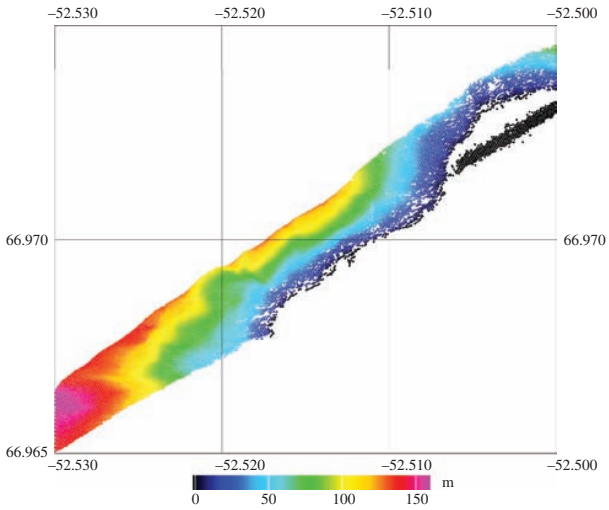

COLOUR FIGURE

Figure 3. The swath of the LiDAR data set recorded between Kangerlussuaq and Sisimiut.

For most areas, we observe a mean difference between the two data sets of 10–20 m. This indicates a potential offset of the GDEM with respect to the LiDAR tracks. The largest mean and RMSE are found in areas 1, 2 and 4, which are ice-covered areas with seasonal variations in elevations.

Examples of comparison of the LiDAR track data and interpolated ASTER grid data are shown in figure 2(*a*)–(*c*). The ASTER GDEM tiles in figure 2(*a*) show part of the Disko Island (area 2, cf. figure 1). One of the LiDAR data sets, from 2008, used to evaluate these tiles is shown in figure 2(*b*). The LiDAR elevation profile is depicted in black while the ASTER GDEM elevation profile is depicted in red (figure 2(*c*)). The corresponding QA values are shown in grey.

Figure 4 shows the correlation between the RMSE as a function of the QA-quality factor as well as the correlation of the RMSE as a function of height variability in the area. Figure 4(*a*) illustrates the expected increase of RMSE height error as the number of stereo scenes (the QA factor) is decreased, with the error apparently being invariant for QA factor above 7–8. Figure 4(*b*) shows a clear non-linear correlation of the height errors as a function of height variation in the blocks. Figure 4 is based on data from all areas, except for area 2 where only one LiDAR swath profile (from 2008) is used to avoid over-weighting of results from that particular area. It is seen that the RMSE increase dramatically for elevations larger than 1000 m, likely associated to the snow cover at high altitudes and the lack of orthorectification during the pre-processing of ASTER imagery.

4. Conclusions

We find that the ASTER GDEM tiles, in Greenland, investigated here show an accuracy of 15–65 m RMSE vertically when compared with LiDAR data, which is significantly above the quoted 20 m average accuracy.

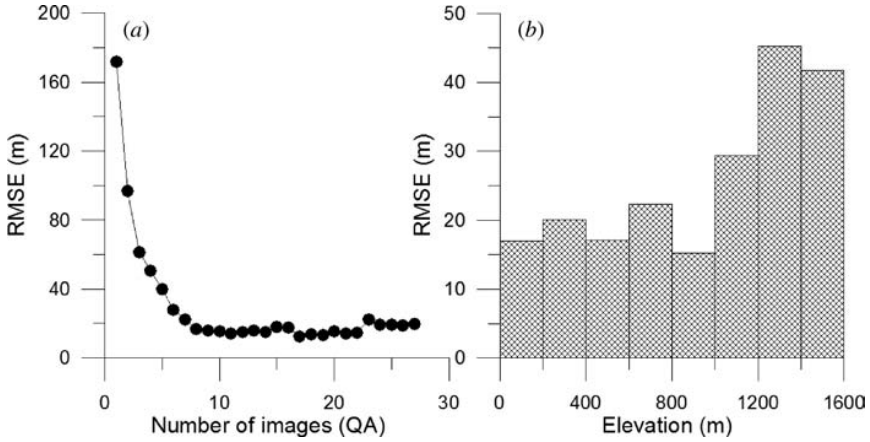

Figure 4. Error statistics for elevation differences. (*a*) RMSE for elevation differences versus number of images (QA). (*b*) RMSE of elevation differences versus elevation (LiDAR data).

The reduced ASTER GDEM accuracy is a result of different factors. The GDEM generation process is affected by clouds, shadows, scene averaging, steep slopes and seasonal variations that decrease the QA values per DEM grid cell.

The ASTER scenes were not orthorectified and thus the error increases in high relief regions. Even though the scenes averaging that is performed is expected to decrease the linear error in high relief areas, ASTER is a passive sensor, and hence clouds and illumination conditions decrease the exposure of Greenland, resulting in a decrease of QA numbers and thus increasing the overall error of the GDEM product. In addition, the steep slopes in the coastal regions emphasize the effect of mis-registration and positional accuracy (among the ASTER GDEM and LiDAR elevation data sets) to linear error.

Furthermore, the ASTER GDEM was produced from imagery acquired from almost a decade (2000–2009). Thus seasonal and climatic changes of the ice sheet are incorporated in the elevation values derived from ASTER GDEM. Inherent in this type of comparison is thus the natural variability of the ice elevations due to yearly accumulation and melt and possible long-term trends, especially along the ice sheet margin. For area 2 (Disko Island), the annual accumulation is approximately 0.5 m (Burgess *et al.* 2010) and the change between the different LiDAR data sets (from the spring period) is below 1 m/year, which is significantly lower than the GDEM accuracy. Only in the margin of the main Greenland ice sheet are changes in the ice height of several meters per year documented due to large ablation, but none of the ice-covered areas studied here are known to be affected by significant ice loss.

We have demonstrated a correlation between large RMSE and low QA values (figure 4(a)). Furthermore, the snow cover and wet surfaces reduce the correlation between the individual images and hence also reduce the accuracy in the stereo-correlation process underlining the GDEM processing. The coastal areas in Greenland are characterized by high terrain relief; thus elevation differences are emphasized in high sloping areas because mis-registration among the two data sets will increase the elevation differences as observed in this study. The differences among the two data sets are also increased in ice-covered

regions due to the seasonal changes in the ice sheet. The elevation differences across the ice sheet margin (study areas 1, 2 and 4) do present the highest standard deviation.

In summary, the statistics (table 1) indicate that the expected overall accuracy specifications are not fulfilled (ASTER GDEM Validation Team, 2009). The ASTER GDEM elevations in the studied areas have an RMSE elevation difference of 15–65 m and a mean difference, a bias, in the order of 10–20 m. On the contrary, these findings are in accordance with the accuracy standards observed from the Alaskan and Canadian regions (seasonal ice and snow covered) by the ASTER GDEM Validation Team (2009).

Despite the possible reduction in accuracy over Greenland as shown by this study, the ASTER GDEM is the most accurate DEM available at the very high (1 arc-second) spatial resolution. The ASTER GDEM might be improved with the use of data from other types of satellite missions such as SAR interferometry and ICESat laser altimetry together with data from available digital photogrammetry DEMs, geodetic point elevations as well as data from airborne laser-scanning campaigns. Current flight campaigns, such as the ongoing NASA IceBridge project, would provide significant new data that are useful for correction of GDEM errors in the land/ice transition zones.

Acknowledgement

The ASTER GDEM is a product of The Ministry of Economy, Trade and Industry of Japan (METI) and the National Aeronautics and Space Administration (NASA), http://www.ersdas.or.jpl/GDEM/E/4.html.

Several colleagues from DTU Space participated in field campaigns and data processing over the years. We especially thank Lars Stenseng, Henriette Skourup, Nynne S. Dalå and Kristian Keller.

References

ASTER GDEM Validation Team. METI/ERSDAC, NASA/LPDAAC, USGS/EROS, 2009. In cooperation with NGA and Other Collaborators, ASTER GDEM Validation Summary Report. Available online at: https://lpdaac.usgs.gov/lpdaac/media/files/ASTER_GDEM_Validation_Summary_Report (accessed January 2010). **Q4**

Burgess, E.W., Forster, R.R., Box, J.E., Moseley-Thompson, E., Bromwich, D.H., Bales, R.C. and Smith, L.C., 2010, A spatially calibrated model of annual accumulation rate on the Greenland ice sheet (1958–2007). *Journal of Geophysical Research*, in press. **Q5**

Forsberg, R., Keller, K. and Jacobsen, S.M., 2001, Laser monitoring of ice elevations and sea-ice thickness in Greenland. *International Archives of Photogrammetry, Remote Sensing and Spatial Information Systems*, **XXXIV**, pp. 163–169.

Hvidegaard, S.M., Forsberg, R., Helm, V., Hendricks, S., Skourup, H., Stenseng, L., Hanson, S. and Haas, C., 2009, CRYOVEX 2008 Final Report. *Technical Report* No. 2, DTU Space.

Hvidegaard, S.M., Forsberg, R. and Skourup, H., 2006, Sea ice thickness estimates from airborne laser scanning. In *Arctic Sea Ice Thickness: Past, Present and Future*, P. Wadhams and G. Amanatidis (Eds.), pp. 193–206 (Brussels, Belgium: Climate Change and Natural Hazards Series). **Q6**

Lintz Christensen, E., Reeh, N., Forsberg, R., Jørgensen, J.H., Skou, N. and Woelders, K., 2000, A low cost glacier mapping system. *Journal of Glaciology*, **46**, pp. 531–537.

Maune, D.F. (Ed.), 2001, *DEM Quality Assessment, Digital Elevation Model Technologies and Applications: The DEM Users Manual* (Bethesda, MD: American Society for Photogrammetry and Remote Sensing).

Appendix D

Paper 4

Sørensen, Louise Sandberg, Stenseng, L., Simonsen, S. B., Forsberg, R., Poulsen, S. K. and Helm, V. (2010), *Greenland Ice Sheet changes from space using laser, radar and gravity*, ESA Living Planet Conference, ESA Special Publication SP-686. Sørensen et al. (2010b)

GREENLAND ICE SHEET CHANGES FROM SPACE USING LASER, RADAR AND GRAVITY

Louise Sandberg Sørensen[1], L. Stenseng[2], S. B. Simonsen[3], R. Forsberg[1], S. K. Poulsen[1], and V. Helm[4]

[1]*Geodynamics Dept., DTU-Space, National Space Institute, Juliane Maries Vej 30, DK-2100 Copenhagen, Denmark*
[2]*Geodesy Dept., DTU-Space, National Space Institute, Juliane Maries Vej 30, DK-2100 Copenhagen, Denmark*
[3]*Centre for Ice and Climate, NBI, Uni. of Copenhagen, Juliane Maries Vej 30, DK-2100 Copenhagen, Denmark*
[4]*Geosciences Division, Alfred Wegener Institute, Columbusstrasse, D-27568 Bremerhaven, Germany*

ABSTRACT

The Greenland cryosphere is undergoing rapid changes, and these are documented by remote sensing from space. In this paper, an inversion scheme is used to derive mass changes from gravity changes observed by GRACE, and to derive the mean annual mass loss for the Greenland Ice Sheet, which is estimated to be 204 Gt/yr for the period 2002-2010.
NASA's laser altimetry satellite ICESat has provided elevation estimates of the ice sheet since January 2003. In order to be able to compare GRACE and ICESat derived results, the ICESat volume change must be converted into a mass change estimate. Therefore, it is necessary to model the densities and compaction of the firn. We find that data from ASIRAS show great potential for validating the glaciological models used to determine the densities and firn compaction.

Key words: Greenland Ice Sheet; GRACE; ICESat; ASIRAS.

1. INTRODUCTION

The space-based techniques for measuring cryospheric changes are very different in nature, and have different advantages and disadvantages. The large present-day changes of the Greenland Ice Sheet are quantified by the different satellite data sets. Gravity changes observed by the GRACE satellites since 2002 can be used to estimate the total mass loss of the ice sheet [1, 2, 3]. The GRACE observations are sensitive to other mass redistribution signals such as post glacial rebound (PGR), which is still poorly constrained in Greenland. In this paper, we use an inversion scheme to estimate the mean annual mass loss of the Greenland Ice Sheet from GRACE data (2002-2009).
NASA's laser altimetry satellite ICESat has, since the launch in January 2003, provided time tagged and geolocated elevation estimates of the ice sheet. The ICESat laser signal is reflected by the snow surface and thus allowing the estimation of the change in volume of the entire ice sheet. Modeling of the snow/ice densities, and processes such as firn compaction, is a necessity in order to convert the volume change of snow and ice observed by ICESat into a mass change estimate, which can be compared with the GRACE results.
We show that the use of high resolution SAR altimeter data from ASIRAS along the EGIG line (see Figure 1) has great potential for validating and constraining the glaciological models, used to convert volume to mass changes.

2. MASS LOSS OF THE GREENLAND ICE SHEET FROM GRACE

We use a Tychonov generalized inversion method with regularization described in [4], to derive monthly mass variations of the Greenland Ice Sheet from changes in gravity, observed by the GRACE satellites.
The GRACE Level-2 data used, consist of monthly spherical harmonic expansions of the Earth's gravity potential. The monthly solutions are represented by a set of Stokes harmonic coefficients up to degree and order 60 [5], provided by the CSR processing center (Center for Space Research, University of Texas, USA) [6]. The C_{20} coefficients in the monthly GRACE solutions are replaced by coefficients derived from 5 satellite laser ranging (SLR) campaigns [7].
The gravity signal caused by PGR is determined from the ice history ICE-5G(VM2) [8], and is subtracted from the gravity trend derived from the GRACE data.
The time series of mass change is shown in Figure 2. By fitting a linear trend through the entire period (2002-2009) gives a mean annual mass loss of 204 Gt/year.

3. ICESAT DERIVED ELEVATION CHANGES ALONG THE EGIG LINE

The elevation changes of the ice sheet near the EGIG line are derived from the ICESat data. The area is outlined

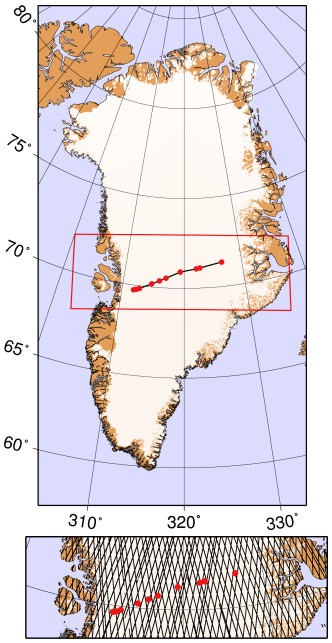

Figure 1. The upper figure shows the EGIG line crossing the Greenland Ice sheet. The lower figure shows the ICESat ground track coverage in the area.

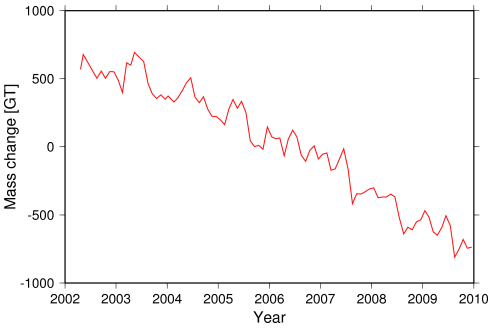

Figure 2. Mass change time series of the Greenland Ice Sheet from the monthly GRACE CSR models.

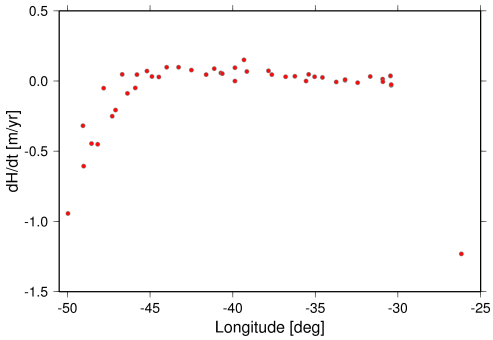

Figure 3. Elevation changes [m/yr] along the EGIG line derived from ICESat data.

in Figure 1. The data used is the GLA12 'Antarctic and Greenland Ice Sheet Altimetry Data' product [9], which was downloaded from National Snow and Ice Data Center. This study is based on the available release 31, 91-day repeat cycle data, spanning the period from October 2003 to March 2008.

Filtering of the data and application of corrections is necessary in order to remove problematic data [10, 11]. The saturation correction is added to the relevant measurements, which are flagged in the data files. We reject problematic data, based on the shape of the return signal, and the number of peaks. Besides these criteria, we have used the data quality flags and warnings given with the data to reject less accurate measurements [12].

Due to problems with the GLAS instrument, ICEsat has measured only 2-3 months (campaigns) every year. The ICESat ground tracks are not exactly repeated, and this makes deriving elevation changes problematic. An observed elevation difference between two (repeat) tracks is a sum of the surface slope, seasonal variations, and a secular trend.

Several method for deriving elevation changes from ICESat data have been published [13, 14, 15]. The elevation changes (dH/dt) presented here, are derived by a method similar to [16, 17] in which the elevation (H) is assumed to be a linear function of time and the surface slope (along-track and cross-track), and a cosine and sine function, describing the seasonal variability. Using this assumption, we estimate dH/dt in 500 m segments along track. The individual ICEsat measurements in each 500 m segment are assigned a weight which ensures that each available ICESat campaign will have equal weight in the dH/dt solution.

Figure 1 shows the ICESat data coverage in the area, and Figure 3 shows the derived elevation changes in a profile crossing the ice sheet, following along the EGIG line. It is seen, that there is a clear thinning of the ice sheet near the ice margins, and that the elevation changes are close to zero in the central parts.

4. DENSITY AND FIRN COMPACTION MODELLING

In order to tie the different observations of the Greenland Ice Sheet together, modelling of snow and firn processes have to be conducted. An observed elevation change of the ice sheet can be related to mass changes by modelling the firn response to climate changes, and the surface density of the ice sheet.
The firn compaction is a function of climate variables such as temperature and accumulation. It is important to determine the elevation changes caused by firn compaction, since it should not contribute to the total mass balance of the ice sheet determined from ICESat data.
Following [18, 19, 20, 21, 22], the annual firn layer thickness (λ) at time after deposition $t = t_0 + t_i$, can be modeled by Eq. 1

$$\lambda(t_0, t) = \begin{cases} \left(\frac{(b(t_0) - r(t_0))\rho_i}{\rho_f(t_0, t)} + r(t_0) \right) \tau & ,b(t_0) \geq r(t_0) \\ b(t_0)\delta(t - t_0)\tau & ,b(t_0) < 0 \end{cases} \quad (1)$$

where b is the surface mass balance, $r(t_0)$ is the amount of refrozen melt water inside the firn layer, ρ_i is the density of ice, ρ_f is the surface firn density, τ is a time constant and δ is the Kronecker delta. The layer thickness is estimated from year to year, to determine the elevation changes of the Greenland Ice Sheet, caused by changes in the surface temperature and precipitation.
Firn compaction modelling is associated with a number of unknowns, and the error analysis is not tangible from the model input. However, an important part of the modelling is to validate the models with airborne measurements such as the ASIRAS flight campaign and connected firn density studies from in-situ measurements.

5. ASIRAS DATA

The ASIRAS instrument [23] is developed as an airborne interferometric SAR altimeter with properties similar to the SIRAL instrument on CryoSat-2. ASIRAS radar data and lidar data was collected in spring 2006 along the EGIG line and snow densities were measured with N-probe [24] at selected sites. A combination of the delay compensated SAR processing and the low flight altitude (approximate 300 m above terrain), allows the radar signal to penetrate up to 15 m into the snow pack. From the radar return signal it is possible to detect layering in the snow pack [25], caused by the seasonal variations in the snow properties.
A local maximum algorithm is used to detect peaks in the ASIRAS echoes, which is related to the annual variation in the snow density. These annual layers can be detected and followed along the EGIG line in the entire dry snow zone, and in some parts of the percolations zone.
Assuming that the snow can be described as a mixture of air and small ice particles, it is possible to calculate

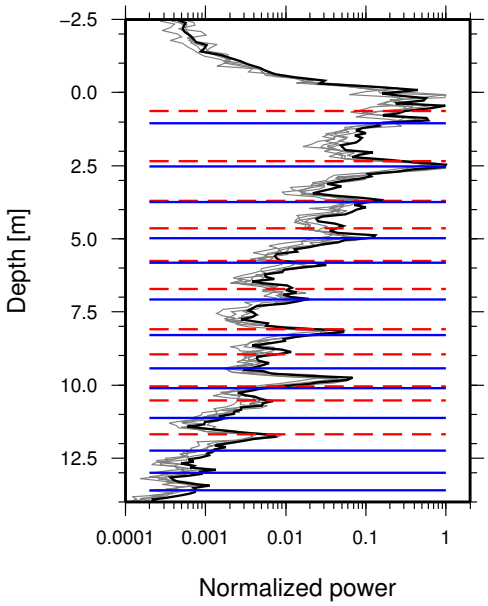

Figure 4. Comparison of different data types at T19. ASIRAS echos (in black and grey), modelled layers (in blue), and high density layers measured by N-Probe (in red).

the permittivity of the snow volume [26], as a function of the density, and hence the refractive index. The apparent depth of a layer can now be converted to true depth using a simple density model for the snow pack. It is now possible to compare the layers derived from the model with the layers detected in ASIRAS data.
An example of typical ASIRAS echoes is shown in Figure 4. The black line shows the echo obtained closest to the T19 site and the grey lines show echoes immediately before and after the closest approach.

6. CONCLUSION AND OUTLOOK

We find a mass loss estimate of the Greenland Ice Sheet of -204 Gt/yr based on GRACE data (2002–2009). In order to compare changes derived from ICESat data with the GRACE results, it is necessary to model firn compaction. Preliminary studies show that the firn compaction is a significant contribution to the total volume change, and therefore it is important to validate the models used.
In order to do so, we use ASIRAS and N-probe data along the EGIG line. We show that in general there are good agreement between ASIRAS data, N-probe data and the snow model west of the Ice Divide, see Figure 4. However, east of the Ice Divide the modelled layers and ASIRAS derived layers deviates, and unfortunately there

is no N-probe data in this area to confirm either.

ACKNOWLEDGMENTS

GRACE data was available via the PO.DAAC system
ASIRAS data has been collected during the CryoVEx (CryoSat Validation Experiment) campaigns by members of CVRT (CryoSat calibration and validation team). We would like to thank all members of the CVRT, especially Elizabeth Morris who collected and processed the N-probe data.
ECMWF ERA-interim data used in this study have been provided by ECMWF and been obtained from the ECMWF Data Server.
ICESat data was downloaded from the NSIDC web site.
We would like to thank S. J. Johnsen for useful discussions of the firn compaction process.

REFERENCES

[1] S. B. Luthcke, H. J. Zwally, W. Abdalati, D. D. Rowlands, R. D. Ray, R. S. Nerem, F. G. Lemoine, J. J. McCarthy, and D. S. Chinn. Recent greenland ice mass loss by drainage system from satellite gravity observations. *Science*, 314(5803):1286–1289, 2006.

[2] B. Wouters, D. Chambers, and E. J. O. Schrama. Grace observes small-scale mass loss in greenland. *Geophys. Res. Lett.*, 35(20):L20501–, October 2008.

[3] I. Velicogna. Increasing rates of ice mass loss from the greenland and antarctic ice sheets revealed by grace. *Geophys. Res. Lett.*, 36(19):L19503–, October 2009.

[4] L. Sandberg Sørensen and R. Forsberg. Greenland ice sheet mass loss from grace data. In *International Symposium on Gravity, Geoid and Earth Observation (GGEO), 2008, Crete, Greece*, 2008.

[5] B. D. Tapley, S. Bettadpur, M. Watkins, and C. Reigber. The gravity recovery and climate experiment: Mission overview and early results. *Geophys. Res. Lett.*, 31, 2004.

[6] S. Bettadpur. *Level-2 Gravity Field Product User Handbook, Rev. 2.3*. Center for Space Research, University of Texas, Austin, 2.3, 2007.

[7] M Cheng and B. D. Tapley. Variations in the earth's oblateness during the past 28 years. *J. Geophys. Res.*, 109:B9, 2004.

[8] W.R. Peltier. Global glacial isostasy and the surface of the ice-age earth: The ice-5g (vm2) model and grace. *Annual Review of Earth and Planetary Sciences*, 32(1):111–149, May 2004.

[9] HJ Zwally, R. Schutz, C. Bentley, J. Bufton, T. Herring, J. Minster, J. Spinhirne, and R. Thomas. GLAS/ICESat L2 Antarctic and Greenland Ice Sheet Altimetry Data V031. *Boulder, CO: National Snow and Ice Data Center left fence http://nsidc. org/data/gla12. html right fence*, 2010.

[10] Benjamin E. Smith, Charles R. Bentley, and Charles F. Raymond. Recent elevation changes on the ice streams and ridges of the ross embayment from icesat crossovers. *Geophys. Res. Lett.*, 32(21):L21S09–, October 2005.

[11] H. A. Fricker, A. Borsa, B. Minster, C. Carabajal, K. Quinn, and B. Bills. Assessment of icesat performance at the salar de uyuni, bolivia. *Geophys. Res. Lett.*, 32(21):L21S06–, September 2005.

[12] NSIDC. Glas altimetry product usage guidance. 2010.

[13] Helen Amanda Fricker and Laurie Padman. Ice shelf grounding zone structure from icesat laser altimetry. *Geophys. Res. Lett.*, 33(15):L15502–, August 2006.

[14] D.C. Slobbe, R.C. Lindenbergh, and P. Ditmar. Estimation of volume change rates of greenland's ice sheet from icesat data using overlapping footprints. *Remote Sensing of Environment*, 112(12):4204–4213, December 2008.

[15] Hamish D. Pritchard, Robert J. Arthern, David G. Vaughan, and Laura A. Edwards. Extensive dynamic thinning on the margins of the greenland and antarctic ice sheets. *Nature*, 461(7266):971–975, October 2009.

[16] Ian M. Howat, Ian Joughin, Mark Fahnestock, Benjamin E. Smith, and Ted A. Scambos. Synchronous retreat and acceleration of southeast greenland outlet glaciers 200006: ice dynamics and coupling to climate. *Journal of Glaciology*, 54:646–660, 2008.

[17] B. E. Smith, H. A. Fricker, I. R. Joughin, and S. Tulaczyk. An inventory of active subglacial lakes in antarctica detected by icesat (20032008). *J. Glaciol.*, 55(192):L21S09–, 2009.

[18] Michael M. Herron and Chester C. Langway. Firn densification: An empirical model. *Journal of Glaciology*, 25(93):373–385, 1980.

[19] H. Jay Zwally and Li Jun. Seasonal and interannual variations of firn densification and ice-sheetsurface elevation at the greenland summit. *Journal of Glaciology*, 48:199–207(9), March 2002.

[20] Jun Li, H. Jay Zwally, Helen Cornejo, and Donghui Yi. Seasonal variation of snow-surface elevation in north greenland as modeled and detected by satellite radar altimetry. *Annals of Glaciology*, 37:233–238, 2003.

[21] Niels Reeh, David A. Fisher, Roy M. Koerner, and Henrik B. Clausen. An empirical firn-densification model comprising ice lenses. *Annals of Glaciology*, 42:101–106, 2005.

[22] Niels Reeh. A nonsteady-state firn-densification model for the percolation zone of a glacier. *J. Geophys. Res.*, 113:–, September 2008.

[23] C. Mavrocordatos, E. Attema, M. Davidson, H. Lentz, and U. Nixdorf. Development of ASIRAS (airborne SAR/Interferometric altimeter system). *IEEE International Geoscience and Remote Sensing Symposium*, 4:2465–2467, 2004.

[24] Elizabeth M. Morris and J. David Cooper. Instruments and methods. density measurements in ice boreholes using neutron scattering. *Journal of Glaciology*, 49(167):599–604, 2003.

[25] R. L. Hawley, E. M. Morris, R. Cullen, U. Nixdorf, A. P. Shepherd, and D. J. Wingham. Asiras airborne radar resolves internal annual layers in the dry-snow zone of greenland. *Geophysical Research Letters*, 33, 2006.

[26] H. Looyenga. Dielectric constants of heterogeneous mixtures. *Physica*, 31:401–406, 1965.

Appendix E

Comparison of rate of elevation change from ICESat and airborne LiDAR measurements.

L. S. Sørensen, S. Bircher, L. Stenseng, H. Skourup, S. Hanson, S. Hvideaard and R. Forsberg, (2009), *Changes of the Greenland Ice Sheet from ICESat and airborne LiDAR measurements*, Part of presentation given at the 'Changes of the Greenland Cryosphere' workshop, Nuuk, 25-27 August 2009.

The airborne LiDAR measurement used in this comparison, were collected during DTU field campaigns in 2003, 2004, 2005, and 2006. The figures to the right show the ICESat results, and the figures to the left show the LiDAR results.

dh/dt derived from Airborne Lidar data

Based on 2003, 2005 and 2006 campaigns

ICESat for comparison

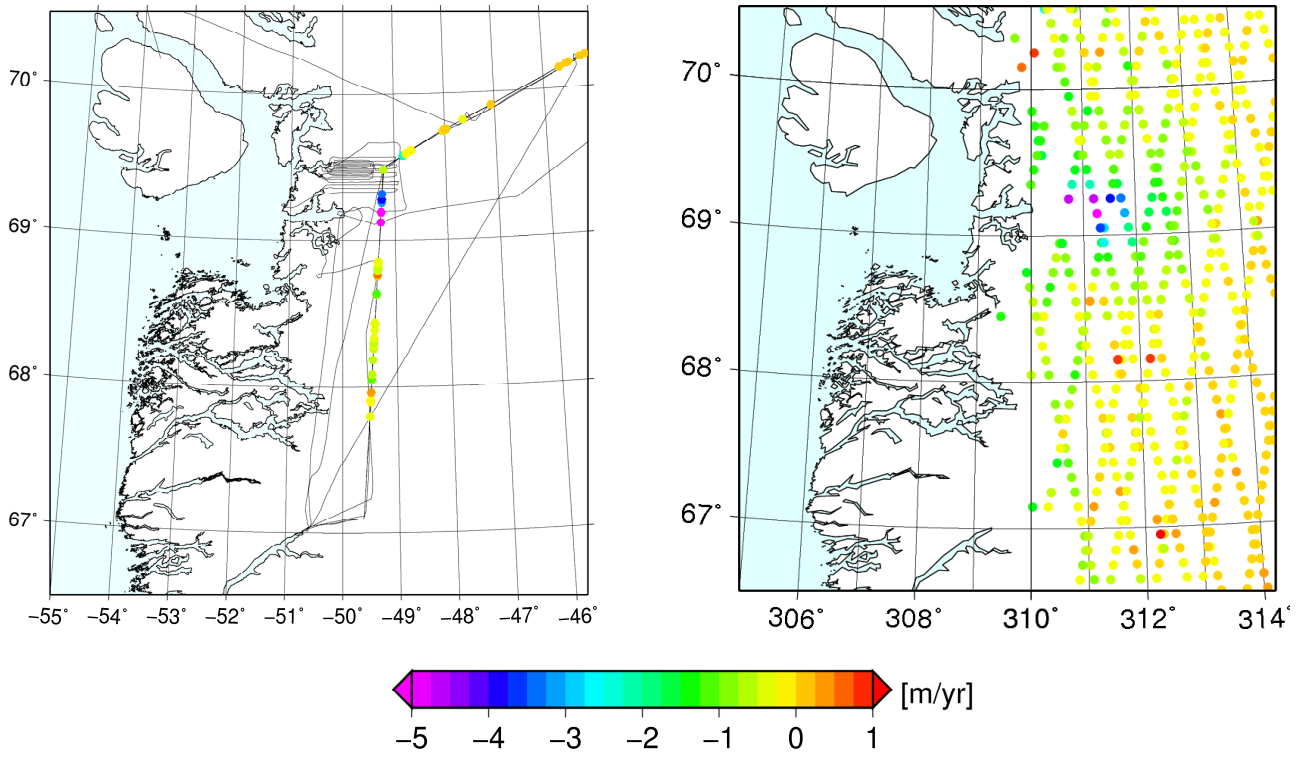

XLVI

dh/dt derived from Airborne Lidar data

Based on 2004 and 2006 campaigns

ICESat for comparison